THE ROLE OF DIELECTRIC SCREENING IN $SrTiO_3$-BASED INTERFACES

A Thesis Submitted to the Committee on Graduate Studies in Partial Fulfillment

of the Requirements for the Degree of Doctor of Philosophy

in the Faculty of Arts and Science

Trent University

Peterborough, Ontario, Canada

Materials Science Ph.D. Graduate Program

January 2019

Abstract

THE ROLE OF DIELECTRIC SCREENING IN $SrTiO_3$-BASED INTERFACES

Amany Raslan

We build a theoretical model for exploring the electronic properties of the two-dimensional (2D) electron gas that forms at the interface between insulating $SrTiO_3$ (STO) and a number of perovskite materials including $LaTiO_3$, $LaAlO_3$, and $GdTiO_3$. The model treats conduction electrons within a tight-binding approximation, and the dielectric polarization via a Landau-Devonshire free energy that incorporates STO's strongly nonlinear, nonlocal, field- , and temperature-dependent dielectric response. We consider three models for the dielectric polarization at the interface: an ideal-interface model in which the interface has the same permittivity as the bulk, a dielectric dead-layer model in which the interface has permittivity lower that the bulk, and an interfacial-strain model in which the strain effects are included.

The ideal-interface model band structure comprises a mix of quantum 2D states that are tightly bound to the interface, and quasi-three-dimensional (3D) states that extend hundreds of unit cells into the STO substrate. We find that there is a substantial shift of electrons away from the interface into the 3D tails as temperature is lowered from 300 K to 10 K. We speculate that the quasi-3D tails form the low-density high-mobility component of the interfacial electron gas that is widely inferred

from magnetoresistance measurements.

Multiple experiments have observed a sharp Lifshitz transition in the band structure of STO interfaces as a function of applied gate voltage. To understand this transition, we first propose a dielectric dead-layer model. It successfully predicts the Lifshitz transition at a critical charge density close to the measured one, but does not give a complete description for the transition. Second, we use an interfacial-strain model in which we consider the electrostrictive and flexoelectric coupling between the strain and polarization. This coupling generates a thin polarized layer whose direction reverses at a critical density. The transition occurs concomitantly with the polarization reversal. In addition, we find that the model captures the two main features of the transition: the transition from one occupied band to multiple occupied bands, and the abrupt change in the slope of lowest energy band with doping.

Keywords: Two-dimensional electron gas, permittivity, dead layer, strain, flexoelectric, Lifshitz transition.

Acknowledgments

"And say, "My Lord, increase me in knowledge." Quran 20:114. " I kneel humbly to ALLAH thanking HIM for showing me the right path, without HIS help my efforts would have gone astray.

I would like to express gratitude to Prof. Bill Atkinson, whose patience and support has been unwavering. His constant encouragement and enjoyment for learning has greatly contributed to complete this work.

I would like to express the deepest appreciation to my committee members, Prof. Rachel Wortis, and Prof. Franco Gaspari for their insightful perspective and for many interesting discussions we had in committee meetings.

I would like to extend my gratitude to the Physics and Astronomy Department staff, Trent University, for their kind support and help, especially Mr. Patrick Lafleur.

Finally, I would like to thank my family for their encouragement and prayer, especially my mother, Fatma. A very special thanks goes out to my sons, Ahmed and Ali, and my husband, Dr. Maher Selim, for their constant love and support.

Contents

List of Tables

List of Figures

Chapter 1

Introduction

Much of modern technology is enabled by the discovery and development of advanced materials that make these technologies work. These include nanodevices, such as quantum dotes, whose properties are different from in the bulk. Here in this thesis, we are interested in a new application of an old material, strontium titanate ($SrTiO_3$). The focus of this thesis is the quantitative modeling of the electronic structure of $SrTiO_3$ (STO)-based interfaces taking into account the role of the STO dielectric properties.

STO interfaces have received extensive attention since Ohtomo and Hwang [1] discovered the existence of a highly conductive layer at the interface between two insulating oxides, STO and lanthanum aluminate ($LaAlO_3$). This conductive layer is a two-dimensional electron gas (2DEG) with a high electron density, $10^{13} - 10^{14}$ cm^{-2} [1, 2], and that is confined to within $\sim 4 - 7$ nm of the interface [3]. By comparison, the 2DEG in silicon devices typically has a density around $10^{10} - 10^{12}$ cm^{-2} and is confined to within $\sim$ 10 nm of the interface [4]. The 2DEG mobility at STO interfaces is found to be nearly 10^4 cm^2/Vs, which is somewhat less than the value of $\sim 10^7$ cm^2/Vs [4] at semiconductor interfaces. In many ways STO-based interfaces are

comparable to semiconductor interfaces; interest in STO interfaces is mainly driven by the possibility of new functionality [5, 6, 4, 7, 8].

Interfaces have been made between STO and a number of perovskite materials, (see Fig. 1.1), such as $LaTiO_3$ [9], $GdTiO_3$ [10], $LaVO_3$[11], $LaGaO_3$[12], and $KTaO_3$ [13]. However, the most celebrated and studied interface is between STO and $LaAlO_3$ (LAO). In addition to being conducting, this interface has a superconducting state below 200mK [14] and ferromagnetism that can be controlled at room temperature[15, 16, 17]. The ability to tune LAO/STO interfaces through metal-insulator [2] and superconductor-insulator transitions by application of a gate voltage makes LAO/STO interfaces promising for potential electronic devices such as tunnel junctions and field-effect transistors [5].

1.1 Mechanisms of 2DEG Formation at STO Interfaces

To date, the origin of the 2DEG at STO interfaces remains unclear. Depending on the growth conditions, there are three main mechanisms that have been proposed as the source of the 2DEG: the polar nature of the cap material, oxygen vacancies, and cation intermixing. We review each scenario, and the experiments that support it.

1.1.1 Electronic Reconstruction

The most popular scenario is an electronic reconstruction that comes from a "polar catastrophe". A polar catastrophe happens when a polar material is attached to a non-polar material. This results in an electric field inside the polar material that creates a large potential difference across it. As the thickness of the polar material increases, this large potential difference leads to electronic and structural instabilities.

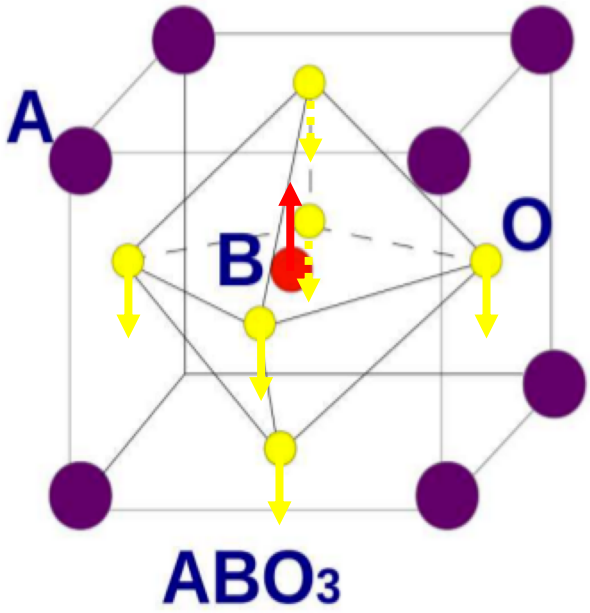

Figure 1.1: Unit cell of ABO_3 perovskite crystals. The A atom here represents strontium (Sr), B is for titanium (Ti), and O for oxygen (O). Arrows show the motion of the Ti and O atoms in the optical soft mode. Figure taken from [18].

For example, at semiconductor GaAs/Ge interfaces, Ge is non-polar, while GaAs is polar. To compensate for the buildup of the electric field, a surface roughening and intermixing of the Ge and Ga at the interface takes place. This is called an atomic reconstruction [4].

In LAO/STO, the electronic instabilty involves a charge transfer between the LAO surface and the interface. This happens due to the perovskite structure of the STO: a perovskite has chemical formula ABO_3, where A and B are cations and the oxygen is the anion. In the case of STO, A = Sr and B = Ti (see Fig. 1.1). In the (001) direction the ABO_3 lattice consists of layers of AO and BO_2 planes. To keep ABO_3 neutral,

the cations A and B may have formal valence $A^{+2}B^{+4}$, $A^{+4}B^{+2}$ or $A^{+3}B^{+3}$, because oxygen has a formal valence of O^{-2}. In LAO/STO interfaces, the cation valences are $Sr^{+2}Ti^{+4}$, and $La^{+3}Al^{+3}$. Accordingly, STO ($Sr^{+2}Ti^{+4}O_3^{-6}$) is stacked in alternating layers of $Sr^{+2}O^{-2}$(AO) and $Ti^{+4}O_2^{-4}$ (BO_2), which are neutral planes, having no net charges. On the other hand, LAO ($A^{+2}B^{+4}O_3^{-6}$) has planes of $La^{+3}O^{-2}$(AO) and $Al^{+3}O_2^{-4}$ (BO_2), with net charge +1 and -1, respectively. Thus, the interface of LAO and STO is between polar LAO and non-polar STO, leading to a polar discontinuity at the interface. If we imagine LAO as a chain of capacitors in series, then a potential will grow through each capacitor leading to a voltage difference between the LAO surface and interface, as illustrated in Fig. 1.2.(a). The growth of this voltage with LAO thickness is known as a "polar catastrophe".

The existence of Ti at the interface gives the possibility for an electronic reconstruction because Ti has a multivalent nature, Ti^{+3} or Ti^{+4}. Thus, if a half-electron per unit cell is transferred from the top layer of the LAO, it will find accommodation in a Ti atom at the interface, which will become $Ti^{+3.5}$, as shown in Fig. 1.2.(b). This electronic reconstruction compensates the electric field in the LAO layers [Fig. 1.2.(b)], and solves the polar catastrophe problem. This scenario is valid for n-type STO interfaces in which the STO surface has to be TiO_2-terminated in the (001) direction. However, for the p-type interface, for which the STO surface has to be SrO-terminated in the (001) direction, the electronic reconstruction occurs by transferring a half-hole from the surface of LAO layers. Since there is no possibility to form $Ti^{+4.5}$, the holes are trapped by oxygen vacancies at the interface, which leads the p-interface to be insulating [19, 1].

The polar catastrophe scenario was proposed first by Ohtomo and Hwang in their

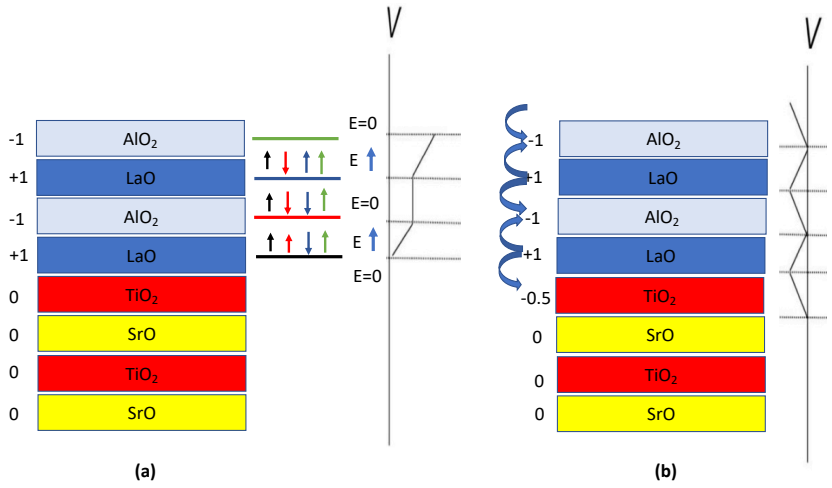

Figure 1.2: Polar catastrophe scenario.(a) shows the origin of the polar catastrophe. 0's, +1's, and -1's represent the net charge per layer which generates a corresponding electric field E, and potential V along the z-direction. The potential difference between the surface and interface grows with LAO thickness. (b) shows that a transfer of 0.5 electron per unit cell to the interface eliminates the diverging potential. Figure taken from [18].

seminal paper [1]. Later, it was supported experimentally by Thiel et al.[2]. They found that there is a critical LAO thickness, after which the LAO/STO interface is conducting. This means that, when the thickness of the LAO layer is small, the potential difference between LAO surface and the interface is small. Once the LAO thickness exceeds a critical value, ~ 4 unit cells [2], the potential becomes larger than the LAO band gap. As a result, charges are transferred to the interface.

On the other hand, the polar catastrophe scenario is not able to explain multiple observations of conductive interfaces for which there is no polar discontinuity, such as amorphous LAO on STO [20], and interfaces in the (110) direction [21]. In addition, according to this scenario the electron density has to be in order of 3×10^{14} cm^{-2}, but

the experimentally measured density (from the Hall effect) is an order of magnitude lower ($\sim 2-6\times10^{13}$ cm^{-2}). All of this raises doubts that the polar discontinuity is the only scenario for the 2DEG at STO-based interfaces.

1.1.2 Oxygen Vacancies

A second possible scenario for the 2DEG formation is oxygen vacancies. These are a common type of defect in oxide materials, and they are created during sample growth, especially at low oxygen pressure, and act as electron donors. In bulk STO, oxygen vacancies can create electron concentrations exceeding $\sim 10^{17}$ cm^{-3} [22, 7]. In the case of LAO/STO interfaces, the vacancy concentration depends on the oxygen partial pressure and the temperature during growth [23, 24]. Oxygen vacancies can form both on the STO side of the interface and at the LAO surface [25]. Experiments reported that oxygen vacancies in the STO substrate can give electron densities that are up to 1000 times larger than predicted by the polar catastrophe model [1, 7]. However, while it seems likely that oxygen vacancies contribute to the 2DEG, they can not by themselves explain why the conducting interface is formed only after a critical LAO thickness [2].

1.1.3 Cation Intermixing

Cation intermixing is considered as another scenario for the 2DEG formation [26]. It takes place when the STO substrate is doped with La: Zaid el al. [27] reported that the exchange between Sr^{+2} and La^{+3} results in the formation of a conducting $La_xSr_{1-x}TiO_3$ layer at the interface. Despite the experimental evidence of cation intermixing, it can not for example explain the critical thickness for a metal-insulation

transition, or why LAO/STO alloys are found to be insulating [7].

In summary, there is no consensus on the origin of the 2DEG at STO interfaces. It is possible, in fact, that a combination of these scenarios controls the 2DEG formation, and that this combination depends on the interface geometry and growth conditions. For the (001) LAO/STO interface, the existence of a metal-insulator transition at 4 unit cells of LAO suggests that the polar catastrophe mechanism is dominant in this case.

1.2 STO Interface Band Structure

Bulk STO is a band insulator with 3.25 eV band gap, and it can be electron-doped with Nb, La, or oxygen vacancies [7]. Its valence band is composed of $2p$ oxygen orbitals, while the conduction band is composed of Ti $3d$ orbitals. Due to crystal fields, the $3d$ orbitals split into t_{2g} and e_g symmetries. In bulk STO, the t_{2g} orbitals (d_{xy}, d_{xz} and d_{yz}) are degenerate at the Brillouin-zone center Γ-point [28], as shown in Fig. 1.3.

Although the band structure in bulk STO is well known, the interface adds complications that lead to uncertainty in the detailed band structure of the 2DEG. Notably, the electric fields that confine the 2DEG to the interface are shaped by STO's dielectric permittivity. In the next section, we review what is known about the permittivity.

Many theoretical methods have been used to study the interface band structure, including density functional theory (DFT)[29, 30], tight-binding models [31, 32, 33], and Poisson-Schrodinger models [3, 34]. Early DFT calculations were done to explain the origin of the 2DEG [29]. Popovic et al. [29] reported that the occupied conduction bands are derived from Ti t_{2g} orbitals, with the band minimum at the Γ point. Figure

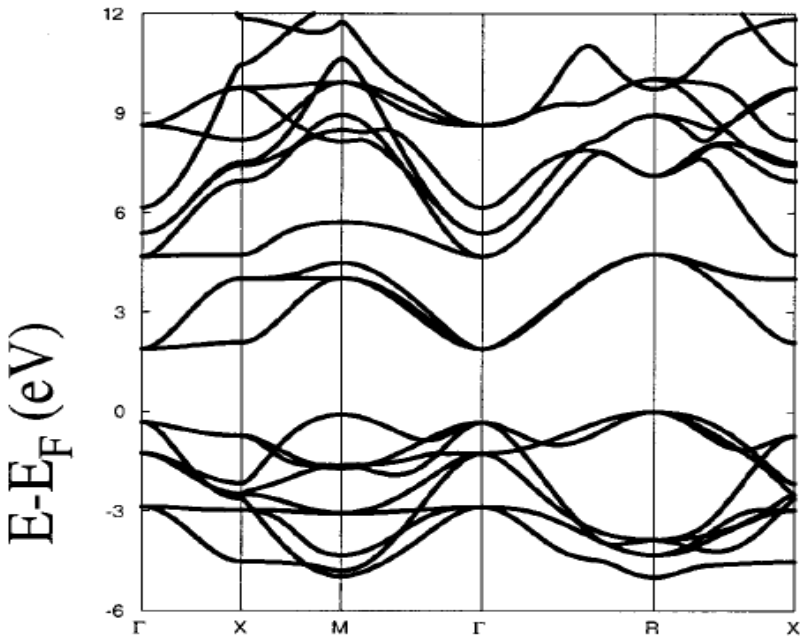

Figure 1.3: The band structure of bulk STO. At the Γ point, the lowest three conduction bands have Ti t_{2g} character, while the top three valence bands have O $2p$ character. Reprinted from [28], with the permission of AIP Publishing.

1.4 shows the resulting subband structure that forms at the interface. The lowest energy band has xy character with the wave function localized in the first Ti layer at the interface [Ti1(xy) in Fig. 1.4]. Above the first band at the Γ point, there are bands with xz and yz character [Ti1, Ti2, Ti3 (xz)], and high-energy xy bands whose wavefunctions spread over several layers. Popovic et al. suggested that the first xy band is sensitive to interface disorder, and that its charges are localized and do not contribute to transport. They proposed that this can explain why the measured Hall charge density ($\sim 2-6.\times 10^{13}$ cm^{-2}) is much smaller than the theoretically proposed one ($\sim 3.\times 10^{14}$ cm^{-2}) obtained from the polar catastrophe scenario. This proposal

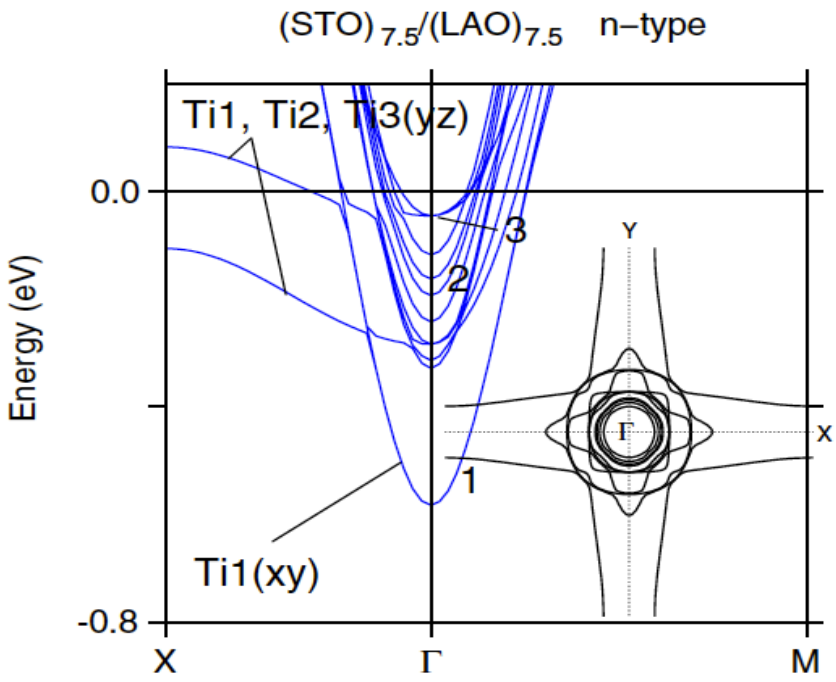

Figure 1.4: The calculated subband structure for LAO/STO interface and their predominant orbital characters. Band dispersions are shown along the interface (xy plane) with X $= \pi/a(1,0,0)$ and M $= \pi/a(1,1,0)$, where a is the in-plane lattice constant. The inset shows the resulting Fermi surface in the xy-plane. Figure taken from [29][https://link.aps.org/doi/10.1103/PhysRevLett.101.256801].

has not, however, been verified experimentally.

Popovic's calculations, as well as other DFT calculations, suffer from the limited thickness of the STO layer used in simulations. The DFT computational cost increases with system size, which leads to finite-size effects in the DFT results. Son et al.[30] studied the effect of STO thickness on the charge distribution using thicknesses up to 30 unit cells. They reported that as the STO thickness increases, the charges move from the interface region to inside the STO. This demonstrates that finite size effects can be an important factor in simulations. Stengel [35] has compared first-principles

methods with a model Hamiltonian, and found that both give similar band structures [36]. This opens the door for the use of tight-binding and Poisson-Schrodinger models: these simplified models can be used to study large systems extending hundreds of nm away from the interface.

Tight-binding and Poisson-Schrodinger models are mostly used to study the doping-dependent band structure. References [32] and [31] found that the charge density has a big effect on the shape of the quantum well, and consequently on the band structure. Reference [31]'s results are discussed in detail in the next section.

Experimentally, angle resolved photo-emission spectroscopy (ARPES) is the most-used technique to directly measure the band structure. ARPES is a surface-sensitive probe, and its measurements can give information about band masses and signatures of spin-orbital coupling. Although ARPES seems not to be convenient for studying STO-based interfaces, where the interesting part is buried under the surface, Santander-Syro1 and co-workers successfully applied ARPES to investigate the surface states of vacuum-cleaved STO [37]. They made the surface of STO metallic by oxygen vacancy doping, and found that there is a 2DEG confined within a few unit cells of the surface. Their results showed that t_{2g} bands split into multiple subbands at the surface, similar to what is shown in Fig. 1.4. The authors argued that the 2DEGs at STO surfaces and STO-based interfaces are not very different [28].

In summary, both calculations and experiments suggest that the 2DEGs occupy the Ti t_{2g} orbitals. The band structure consists of subbands with different orbital symmetries. The lowest energy band has xy character and is confined to the interface. The higher energy bands have xy, xz and yz character and spread across many Ti layers. This picture applies at high density. The question of why the measured charge

density is so much lower than predicted by DFT has not been answered, and it is not clear whether this picture applies at all dopings.

1.3 Dielectric Properties of STO

STO is well known for its high dielectric permittivity [38, 39], which is a strong function of both the temperature and electric field. Figure 1.5 shows measurements of the temperature dependence of the dielectric constant (ϵ) at different bias fields ranging from $0 - 500$ V/mm. At high T and zero field, ϵ(T)$\sim$(T-T_c)$^{-1}$, where $T_c \sim 30$ K [40]. This equation implies that there is a ferroelectric transition at T_c; however, the dielectric constant saturates before it diverges because quantum fluctuations suppresses the ferrolectric transition [41]. For this reason STO is known as a quantum paraelectric.

The strong increase of dielectric permittivity at low temperatures was demonstrated to be associated with the softening of a transverse optical phonon mode [42]. The optical mode involves the titanium and oxygen atoms moving in opposite directions (see Fig. 1.1). The frequency of this optical mode is found to be temperature-dependent [42], and as the temperature decreases, the mode frequency decreases. This is known as mode softening. The optical mode is also sensitive to the electric field.

There are two important points about Fig. 1.5: first, the dielectric constant increases non-linearly when both temperature and electric field are lowered; second, the electric field-dependence of the permittivity disappears for temperatures greater than 50 K. Any dielectric model must be consistent with these two observations.

Several calculations have been made based on tight-binding or continuum models

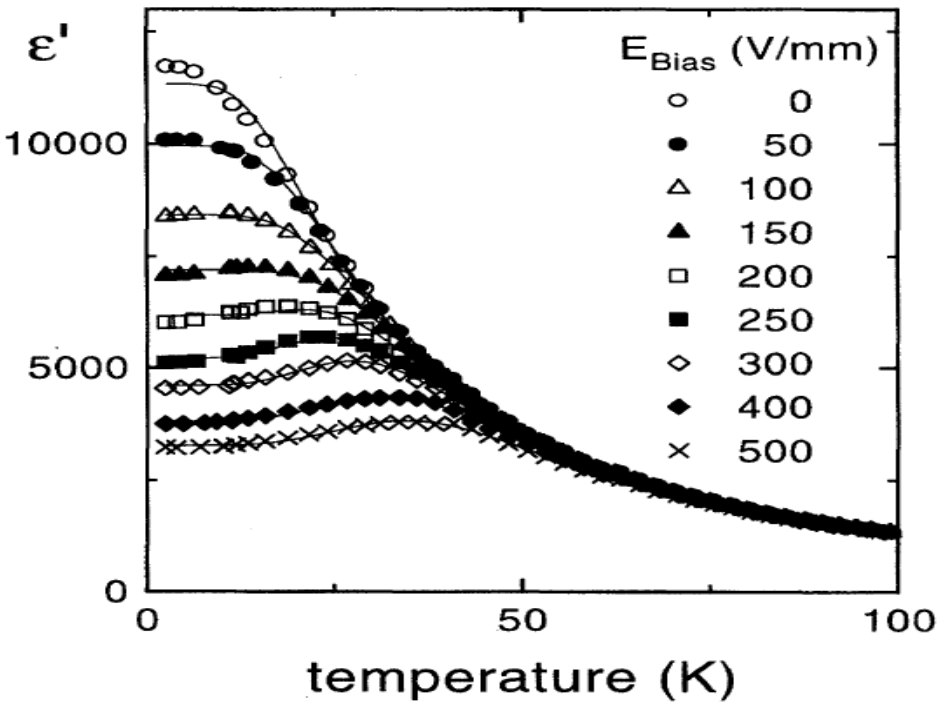

Figure 1.5: Temperature dependence of the real part of dielectric constant in ϵ' STO for various fields between 0 V/mm and 500 V/mm. ϵ' is the real part of the component ϵ_{zz} of the permittivity tensor. The solid lines represent the fitting of experimental data to mean field equations. Figure taken from [39][https://link.aps.org/doi/10.1103/PhysRevB.52.13159].

that build in relevant properties of the dielectric function [3, 31, 32, 34, 43]. These phenomenological approaches have tended to focus on the nonlinear response of ϵ to the electric field as a way to understand the doping-dependence of the charge profile near the interface.

For example, Copie et al.[3] performed conductive-tip atomic force microscopy experiments to study the charge density profile in cross-section LAO/STO samples at high (300 K) and low (10 K) temperatures. They modeled their results by solving the Poisson-Schrodinger equation for the interfacial charge distribution. They found that a correct description of the charge profile depends on including the nonlinear

field response in their model.

A more realistic treatment of the dielectric properties has been made by Khalsa and MacDonald [31]. They used a tight-binding approach to study the effect of the charge density on the electronic structure and charge confinement. They treated the lattice polarization within a Landau-Devonshire approximation that inherently includes nonlocal effects. In addition, they included a quartic term in the lattice energy that represents the nonlinear response of the lattice to strong electric fields. The charge profile and band structure were obtained by solving the tight-binding Hamiltonian and the Poisson equation self-consistently. Their calculations have been performed with 60 layers of STO, at fixed temperature (90K), and for different dopings.

For low carrier densities (doping $\leq 10^{14}$ cm^{-2}), they found that the charges spread deeply into the STO (up to ~ 50 layers). As the doping increases, the spread of the charges decreases, and at very high doing ($> 5 \times 10^{14}$cm^{-2}) half of the total charge is confined in the first layer of STO. The behaviour of the charge confinement can be understood from the relation between the electric field and dielectric permittivity. At low doping, the electric field is too weak to confine the electrons. At high doping, the electric field is strong enough that the nonlinear term is important and confines strongly the 2DEG to the interface. These calculations demonstrate the interplay between the dielectric permittivity and the band structure.

1.4 Outlook

In this thesis, we study the effect of dielectric screening on the electronic structure of STO interfaces. Previous treatments of the STO dielectric function have ignored

its temperature dependence, and have assumed that the response at the interface is the same as in the bulk. In Chapter 2, we present our model for the interface. We start with Khalsa and MacDonald's model, and expand it to include temperature-dependence. This model is for "ideal interfaces", since we assume that the dielectric permittivity is the same as in the bulk. Results for this model are presented in Chapter 3. These results were published in Ref. [33].

Chapter 4 is motivated by an observed Lifshitz transition at low doping in the STO-based interfaces. To explain the transition, we modify our polarization model to accommodate a dead layer at the interface. The results for the doping-dependent band structure are presented and are compared with experiments. Discrepancies between these calculations and experiments motivate us to study the effect of interfacial strain on the dielectric function. In Chapter 5, we explore strain effects on the band structure, and show that this may be the origin of the observed Lifshitz transition. These results were published in Ref. [44]. Finally, a conclusion is presented in Chapter 6.

Chapter 2

The Ideal Interface Model

This chapter gives a comprehensive description of our ideal-interface model for STO-based interfaces. The word ideal here means that the interface has the same dielectric properties as bulk STO. The interface model has two distinct pieces: a self-consistent tight-binding description of the electronic bands and a Landau-Devonshire description of the polarization. The electronic Hamiltonian is used throughout this thesis, while the polarization model is updated from chapter to chapter to accommodate certain interface features. We begin with an overview of the model's structure and boundary conditions. Then, we discuss the model's two pieces in more detail. Next, we discuss both nonlocal and nonlinear contributions to the polarization in our ideal dielectric model. At the end, we review our calculation methodology, and discuss code convergence and acceleration.

2.1 Model Sketch and Boundary Conditions

Figure 2.1 shows the model's structure. We consider a thick film of N STO layers stacked in the [001] direction beneath an insulating cap layer. LAO is a typical cap layer, (see Fig. 2.1), because it has a wider band gap than STO, 5.6 eV and 3.3 eV

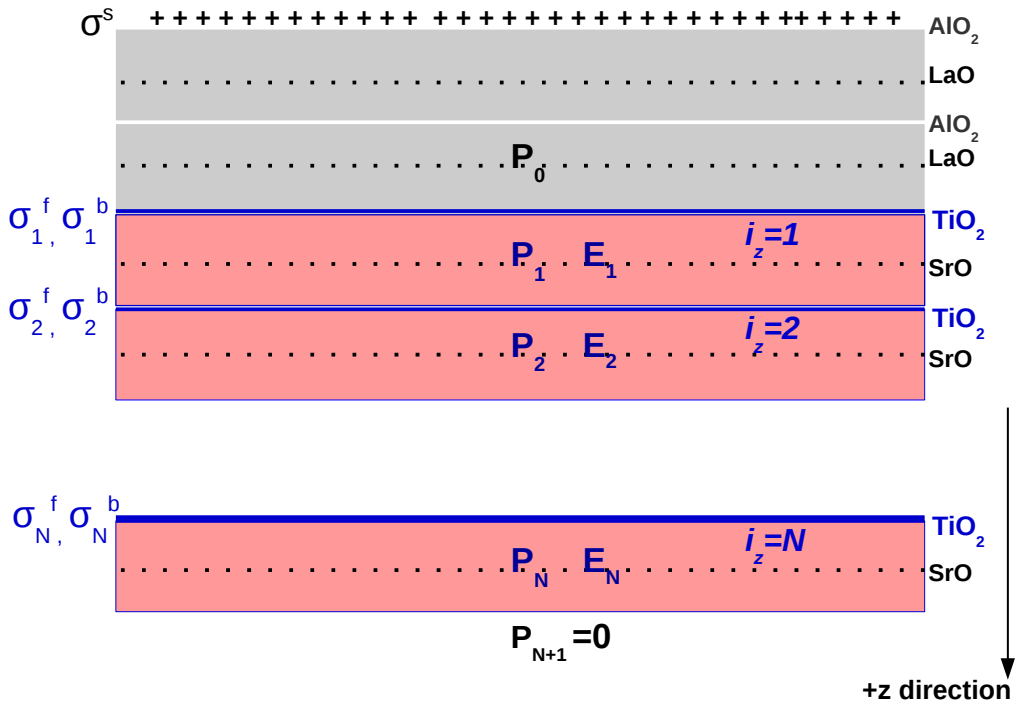

Figure 2.1: Sketch of a model STO/LAO interface. N unit cells of STO are stacked below an insulating LAO film in alternating TiO_2 and SrO layers in the [001] direction. Electronic reconstruction, gating, and surface O vacancies transfer charge from the top AlO_2 layer to the interface, leaving a residual 2D charge density σ^s on the AlO_2 surface that attracts STO conduction electrons to the interface. The model is discretized along the z direction, and assumes that the conducting TiO_2 layers are separated by blocks of dielectric; the polarization P_{i_z} and electric field E_{i_z} are therefore defined in the regions between the TiO_2 layers. The conduction electrons in layer i_z have 2D charge density $\sigma^f_{i_z}$, while the bound charge density due to the polarization is $\sigma^b_{i_z} = P_{i_z} - P_{i_z+1}$. We assume translational invariance in the planes, so the polarization, field, and electron density depend only on the layer index i_z. An extra fictitious dielectric layer ($i_z = N + 1$) is added to facilitate handling the boundary condition $P_{N+1} = 0$ at the bottom of the STO substrate.

respectively. We assume that there is a residual positive charge σ^s (indicated by "+" signs) on the AlO_2 surface originating from any of the possible doping scenarios that are discussed in the previous chapter, such as electronic reconstruction. This residual charge creates an electric field that confines the STO conduction electrons to the interface.

In order to properly define the electric field and polarization inside the STO, the model is discretized along the z direction (perpendicular to the interface). We treat the STO as a set of conducting TiO_2 planes separated by layers of dielectric. As shown in Fig. 2.1, the polarization and electric field are defined in the dielectric layers, while the charge density is confined to the 2D TiO_2 planes.

We assume that we have translational invariance in the planar directions, so that the polarization, electric field, and charge density depend only on the layer index i_z. Then, by symmetry, the polarization and electric field vectors $\mathbf{P}$ and $\mathbf{E}$ must point in the z direction. The surface bound charge is defined as $\sigma^b = \mathbf{P} \cdot \mathbf{n}$. Thus, the 2D charge density in the i_zth TiO_2 plane has two contributions: a free charge density $\sigma^f_{i_z}$ due to the conduction electrons and a bound charge density $\sigma^b_{i_z} = P_{i_z} - P_{i_z-1}$ due to the polarization gradients.

We require boundary conditions for both the electric field and the polarization. In the layered geometry, and for a fixed σ^s, the electric field in the STO is independent of the dielectric permittivity of the cap layer. For simplicity, then, we take the polarization to be zero above the interface (ie. $P_0 = 0$) and the electric field above the first STO layer is therefore (by Gauss' law) $E_0 = \sigma^s/\epsilon_0$. At large z, we expect the electric field and the polarization to be screened by the free charge density: to handle this, the electric field in the Nth STO layer is zero (ie. $E_N = 0$), and we add

a fictitious $(N+1)$th layer in which $\sigma^f_{N+1} = P_{N+1} = 0$.

2.2 Electronic Hamiltonian

The model assumes that there are three types of charge density: the positive surface charge density σ^s at the LAO surface, the free electron charge density $\sigma^f_{i_z}$ and 2D bound charge density $\sigma^b_{i_z}$. Thus we can write the effective Hamiltonian for the STO conduction electrons

$$\hat{H}^{\text{eff}} = \hat{H}_0 + \hat{V}^{\text{ext}} + \hat{V}^{\text{SC}}[\sigma^f, \sigma^b], \tag{2.1}$$

where $\hat{H}_0$ is the tight-binding Hamiltonian for the inter-orbital hopping, $\hat{V}^{\text{ext}}$ is the external potential energy due to the charge at the LAO surface, and $\hat{V}^{\text{SC}}[\sigma^f, \sigma^b]$ represents the self-consistent electrostatic potential energy due to both the free charge density $\sigma^f_{i_z}$ and the bound charge density $\sigma^b_{i_z}$ at the TiO_2 planes, respectively.

2.2.1 The Tight-binding term

STO has a 3.3 eV band gap between filled O $2p$ orbitals and empty Ti t_{2g} orbitals. For an electron-doped interface we therefore include only the t_{2g} orbitals in our model. We adopt a tight-binding Hamiltonian with three orbitals per unit cell, having d_{xy}, d_{xz}, and d_{yz} symmetry. We emphasize here that although the t_{2g} orbitals appear explicitly in our Hamiltonian, the $p-d$ oxygen bonding orbitals appear implicitly, as all the hopping between neighboring t_{2g} orbitals occurs through the O $2p$ orbitals.

We start here with a noninteracting Hamiltonian for the STO

$$\hat{H}_0 = \sum_{i,j} \sum_{\alpha\beta\sigma} c^\dagger_{i\alpha\sigma} t_{i\alpha,j\beta} c_{j\beta\sigma}, \tag{2.2}$$

where i, j labels unit cells, and α, β are for orbital type (d_{xy},d_{xz},d_{yz}). $c_{i\beta\sigma}$ is the annihilation operator for an electron with spin σ in unit cell i and orbital type β, and $c^{\dagger}_{i\alpha\sigma}$ is the corresponding creation operator. $t_{i\alpha,j\beta} = \langle i\alpha|H_0|j\beta\rangle$ is the hopping matrix element of the periodic crystal Hamiltonian $H_0 = \frac{-\hbar^2}{2m}\nabla^2 + V(r)$ between orbital α in unit cell i and orbital β in unit cell j, where $V(r)$ is the lattice potential.

We assume we have translational invariance with periodic boundary conditions in the x and y directions, and apply open (hard-wall) boundary conditions in the z direction. This means there is no hopping through the interface. To diagonalize the Hamiltonian, by Fourier transforming in two dimensions (x and y) to go to k-space, we define

$$\begin{aligned} c_{j\beta\sigma} &= \frac{1}{\sqrt{N_{\mathbf{k}}}} \sum_{\mathbf{k}} e^{i\mathbf{k}\cdot\mathbf{r}_\beta} c_{j_z\mathbf{k}\beta\sigma} \\ c^{\dagger}_{i\alpha\sigma} &= \frac{1}{\sqrt{N_{\mathbf{k}}}} \sum_{\mathbf{k}'} e^{i\mathbf{k}'\cdot\mathbf{r}_\alpha} c_{i_z\mathbf{k}'\alpha\sigma}, \end{aligned} \tag{2.3}$$

with $N_{\mathbf{k}}$ is the number of k-points in the x- and y-direction, $\mathbf{k} = (k_x, k_y)$ is a 2D wavevector, and $\mathbf{r}_\beta$ is a 2D vector in real-space such that $\mathbf{r}_\beta = a(x_{j\beta}, y_{j\beta})$.

Since $i = (i_x, i_x, i_z)$, we replace $\sum_i$ with $\sum_{i_x i_y i_z}$. Substituting Eq. (2.3) in Eq. (2.2), and considering nearest neighbors, the tight-binding term is

$$\hat{H}_0 = \sum_{i_z, j_z} \sum_{\mathbf{k}} \sum_{\alpha\beta\sigma} c^{\dagger}_{i_z\mathbf{k}\alpha\sigma} t_{i_z\alpha,j_z\beta}(\mathbf{k}) c_{j_z\mathbf{k}\beta\sigma}, \tag{2.4}$$

where i_z is layer index, and $t_{i_z\alpha,j_z\beta}(\mathbf{k})$ is now an element of the the tight-binding

matrix,

$$\mathbf{t}(\mathbf{k}) = \begin{bmatrix} \mathbf{E}(\mathbf{k}) & \mathbf{T} & \dots & & \\ \mathbf{T} & \mathbf{E}(\mathbf{k}) & & & \\ & & \ddots & & \\ & & & \mathbf{E}(\mathbf{k}) & \mathbf{T} \\ & & & \mathbf{T} & \mathbf{E}(\mathbf{k}) \end{bmatrix}, \tag{2.5}$$

where $\mathbf{E}(\mathbf{k})$ and $\mathbf{T}(\mathbf{k})$ are matrices in the orbital basis. Considering only hopping between the same orbital types, we obtain

$$\mathbf{E}(\mathbf{k}) = \begin{bmatrix} \epsilon'_{xy}(\mathbf{k}) & 0 & 0 \\ 0 & \epsilon'_{xz}(\mathbf{k}) & 0 \\ 0 & 0 & \epsilon'_{yz}(\mathbf{k}) \end{bmatrix} \tag{2.6}$$

$$\mathbf{T} = \begin{bmatrix} -t^{\perp} & 0 & 0 \\ 0 & -t^{\parallel} & 0 \\ 0 & 0 & -t^{\parallel} \end{bmatrix}, \tag{2.7}$$

and

$$\begin{aligned} \epsilon'_{xy}(\mathbf{k}) &= \epsilon_{t_{2g}} - 2t^{\parallel}(\cos k_x a + \cos k_y a), \\ \epsilon'_{xz}(\mathbf{k}) &= \epsilon_{t_{2g}} - 2t^{\parallel}\cos k_x a - 2t^{\perp}\cos k_y a, \\ \epsilon'_{yz}(\mathbf{k}) &= \epsilon_{t_{2g}} - 2t^{\perp}\cos k_x a - 2t^{\parallel}\cos k_y a, \end{aligned} \tag{2.8}$$

are planar dispersions. Here, $\epsilon_{t_{2g}}$ is the on-site orbital energy (which can be set to 0), and a is the STO lattice constant. For a given symmetry of t_{2g} orbital there are two distinct hopping processes between nearest-neighbour Ti atoms: the hopping

Model parameters	
$t^{\parallel}$	0.236 eV
$t^{\perp}$	0.035 eV
a	3.9 Å
M	24 amu
Q	$8.33e$
ω_0	2.5×10^{13} s^{-1}
ω_1	1.7×10^{13} s^{-1}
α_1	$1.15a$
α_2	$5a$
ϵ_∞	$5.5\epsilon_0$
T_0	1.46×10^4 K
T_s	15 K
λ	1.45
γ	63 eV·Å^{-4}

Table 2.1: Model parameters used in our calculations. Values are taken from Ref. [31] except for T_0, ξ, T_s, and γ, which are obtained by fitting to the temperature- and field-dependence of the experimental dielectric susceptibility (Appendix B).

amplitude is $t^{\parallel}$ between Ti atoms in the same plane as the orbital (eg. the x-y plane for d_{xy} orbitals), while it is $t^{\perp}$ perpendicular to the plane of the orbitals (eg. along the z direction for d_{xy} orbitals). Since nearest-neighbor d_{xy} orbital wavefunctions overlap more in the x-y plane than along the z-axis, $t^{\parallel} \gg t^{\perp}$. Values for $t^{\parallel}$, $t^{\perp}$, and other model parameters are given in Table 2.1.

2.2.2 The Potential Energy term

The charges at the LAO surface (σ^s) create an electrostatic potential inside the STO, which is called in our model the external potential energy V^{ext}. Assuming that this surface charge is uniformly distributed, we obtain a simple description for the

potential energy of an electron in the confining field,

$$\hat{V}^{\text{ext}} = \frac{\sigma^s e}{2\epsilon_\infty} \sum_{\mathbf{k}} \sum_{i_z \alpha\sigma} (z + d_{LAO}) c^\dagger_{i_z \mathbf{k}\alpha\sigma} c_{i_z \mathbf{k}\alpha\sigma}, \tag{2.9}$$

where ϵ_∞ is the high frequency dielectric constant due to electronic screening (discussed in the next section), $z = i_z a$ is the distance from layer i_z to the interface, and d_{LAO} is the thickness of the LAO film.

The self-consistent Hartree potential energy $\hat{V}[\sigma^f, \sigma^b]$ due to $\sigma^f_{i_z}$ and $\sigma^b_{i_z}$ can be represented as

$$\hat{V}^{\text{SC}}[\sigma^f, \sigma^b] = e \sum_{i\alpha\sigma} \phi_{i\alpha\sigma} \hat{n}_{i\alpha\sigma}, \tag{2.10}$$

where $\phi_{i\alpha\sigma} = \frac{1}{4\pi\epsilon_\infty} \sum_j \frac{a^2}{|\mathbf{r}_i - \mathbf{r}_j|} \sigma_j$ is the electron-electron potential with $\sigma_j = \sigma^f_j + \sigma^b_j$ is the total 2D charge density, and $\hat{n}_{i\alpha\sigma} = c^\dagger_{i\alpha\sigma} c_{i\alpha\sigma}$ is the charge density operator for unit cell index i, orbital type α and electron spin σ.

We simplify $\phi_{i\alpha\sigma}$ by assuming that each layer has a homogeneous charge distribution. This means that the potential in each plane is constant and depends only on the layer index. This leads us to write the potential as

$$\phi_{i_z \alpha\sigma} = \sum_{j_z} \sum_{\rho} \frac{1}{4\pi\epsilon_\infty} \frac{a^2}{\sqrt{\rho^2 + (i_z - j_z)^2 a^2}} \sigma_{j_z}, \tag{2.11}$$

where $\vec{\rho}$ is a 2D vector in the x and y-direction. Then,

$$\phi_{i_z \alpha\sigma} = \frac{1}{4\pi\epsilon_\infty} \sum_{j_z} \Big[\int_0^{2\pi} d\theta \int_0^R \frac{1}{\sqrt{\rho^2 + (i_z - j_z)^2 a^2}} \rho d\rho \Big] \sigma_{j_z}. \tag{2.12}$$

where R is a cutoff. We add a constant to Eq. (2.12) to make the interface the zero

of potential. Then, we integrate Eq. (2.12), and take $R \to \infty$, giving

$$\phi_{i_z\alpha\sigma} = \frac{a}{2\epsilon_\infty} \sum_{j_z} (|i_z - j_z| - j_z)\sigma_{j_z}, \tag{2.13}$$

and the potential energy due to free charges in k-space is

$$\hat{V}^{\mathrm{SC}}[\sigma^f, \sigma^b] = \frac{ea}{2\epsilon_\infty} \sum_{\mathbf{k}} \sum_{i_z\alpha\sigma} \sum_{j_z} (|i_z - j_z| - j_z)\sigma_{j_z} \hat{n}_{\mathbf{k}i_z\alpha\sigma},$$

The total 2D charge density σ_{j_z} is obtained by calculating both the bound and free charge densities. The 2D bound charge in layer j_z is

$$\sigma^b_{j_z} = P_{j_z} - P_{j_z+1} \tag{2.14}$$

where the polarization P_{j_z} is obtained from the Landau-Devonshire model discussed in the next section.

The 2D free charge density in layer j_z is $\sigma^f_{j_z} = -e \sum_\beta n_{j_z\beta}/a^2$, where $n_{j_z\beta}$ is the electron occupation number for orbitals of type β in layer j_z. The charge density (Appendix A) is calculated self-consistently from

$$n_{j_z\beta} = \frac{2}{N_{\mathbf{k}}} \sum_{\mathbf{k}} \sum_{n} |\psi_{j_z\beta,n}(\mathbf{k})|^2 f(\epsilon_{n\mathbf{k}}), \tag{2.15}$$

where the factor of 2 is for spin, $\epsilon_{n\mathbf{k}}$ and $\psi_{j_z\beta,n}(\mathbf{k})$ are the energy eigenvalues and eigenstates of $\hat{H}^{\mathrm{eff}}$ (Eq. (2.1)) respectively, and $f(\epsilon_{n\mathbf{k}})$ is the Fermi-Dirac distribution function

$$f(\epsilon_{n\mathbf{k}}) = \frac{1}{1 + \exp\left[(\epsilon_{n\mathbf{k}} - \mu)/k_B T\right]} \tag{2.16}$$

with k_B the Boltzmann constant, T the temperature of the STO in Kelvin and μ the chemical potential.

2.3 Polarization Model

The high polarizability of STO is due to the presence of a soft transverse optical phonon mode that is associated with an incipient ferroelectric transition. The transition is suppressed by quantum fluctuations, so that the dielectric susceptibility saturates at a characteristic temperature $T_s \sim 15$ K (see Fig. 1.5). Here, the induced polarization P_i is defined for unit cell $i = (i_x, i_y, i_z)$ as

$$P_i = \frac{Qu_i}{a^3}, \tag{2.17}$$

where Q is the effective charge associated with the soft mode, and u_i is the normal-mode coordinate representing the amplitude of the lattice distortion, projected onto the soft optical phonon eigenvector [45]. We assume that this polarization is uniform within each atomic layer, and depends only on i_z.

To obtain the polarization, we use a simple quartic free energy, which has the form[31]

$$U = \frac{1}{2}\sum_{i,j} \mathbf{u}_i \cdot \mathbf{D}_{ij} \cdot \mathbf{u}_j - Q\sum_i \mathbf{E}_i \cdot \mathbf{u}_i + \frac{\gamma}{4}\sum_i |\mathbf{u}_i|^4 \tag{2.18}$$

where $\mathbf{D}_{ij}$ is a matrix that contains the force constants between the unit cells located at $i = (i_x, i_y, i_z)$ and $j = (j_x, j_y, j_z)$, and γ is constant of proportionality for the non-linear response. This latter term is important only at high electron densities where the electric field is very strong. In Eq. (2.18), the first term represents the linear response of the lattice to an external electric field, the second term represents the

interaction between polarization and the electric field, and the third term represents the non-linear response to the electric field. The term $\mathbf{D}_{ij}$ includes the nonlocal response of the polarization, which means that the dielectric function is nonlocal (the local case is discussed in the next section).

The electric field $\mathbf{E}_i$ is the total electric field inside the STO. To obtain it, we start from Poisson's equation

$$\epsilon_0 \nabla \cdot \mathbf{E}(z) = \rho(z) - \nabla \cdot \mathbf{P}(z), \tag{2.19}$$

where ϵ_0 is the permittivity of free space, and $\rho(z)$ is the charge density. The polarization here has two contributions: the lattice polarization $\mathbf{P}^{lat}$, and the atomic polarization $\mathbf{P}^{at}$ [46]. Assuming that the atomic polarization is frequency independent, i.e.

$$\mathbf{P}^{at} = \epsilon_0 \chi^{at} \mathbf{E}, \tag{2.20}$$

where χ^{at} is a frequency-independent susceptibility, we obtain

$$\epsilon_0 (1 + \chi^{at}) \nabla \cdot \mathbf{E}(z) = \rho(z) - \nabla \cdot \mathbf{P}^{lat}(z). \tag{2.21}$$

We identify $\epsilon_0(1 + \chi^{at}) = \epsilon_\infty$ as the optical dielectric constant and write

$$\epsilon_\infty \nabla \cdot \mathbf{E}(z) = \sigma^s \delta(z - z^s) + \sum_{j_z} \sigma^f_{j_z} (z - z_{j_z}) - \nabla \cdot \mathbf{P}^{lat}(z). \tag{2.22}$$

where $z^s = d_{LAO}$ is the location of the LAO surface, $z = i_z a$, and $z_{j_z} = j_z a$. Equation (2.22) tells us that the total electric field in the STO has three sources: the surface charge density (σ^s), the free charge density (σ^f), and the bound charge density,

$-\nabla \cdot \mathbf{P}^{lat}(z)$. Because the field $-\mathbf{P}^{lat}(z)/\epsilon_\infty$ is opposite to $\mathbf{P}^{lat}$, it is often referred to as the depolarizing field.

Assuming translational invariance, we can write

$$U = \frac{N_x N_y}{2} \sum_{i_z j_z} u_{i_z} D_{i_z j_z} u_{j_z} - N_x N_y Q \sum_{i_z} u_{i_z} E_{i_z} + \frac{\gamma N_x N_y}{4} \sum_{i_z} u_{i_z}^4 \tag{2.23}$$

where N_x is the number of unit cells in the x-direction, N_y is the number of unit cells in the y-direction, and $D_{i_z j_z} = D_{\mathbf{k}=0, i_z j_z}$. The free energy equation can be written as

$$\frac{U}{N_{2D}} = \frac{1}{2} \sum_{i_z j_z} u_{i_z} D_{i_z j_z} u_{j_z} - Q \sum_{i_z} u_{i_z} E_{i_z} + \frac{\gamma}{4} \sum_{i_z} u_{i_z}^4, \tag{2.24}$$

where $N_{2D} = N_x N_y$.

The potential energy can be then minimized by taking the derivative with respect to u_{l_z} and setting it equal to zero, from which we obtain the constituent equation

$$Q E_{l_z} = \sum_{j_z} D_{l_z j_z} u_{j_z} + \gamma u_{l_z}^3. \tag{2.25}$$

for u_{l_z}. We then use Eq. (2.17) to calculate the polarization.

$D_{i_z j_z}$ can be determined by performing the inverse Fourier transform as

$$D_{i_z j_z} = \frac{1}{N} \sum_{k_z} e^{i k_z (z_i - z_j)} D(\mathbf{k} = 0, k_z), \tag{2.26}$$

where $\mathrm{D}(\mathbf{k} = 0, \mathrm{k_z})$ is defined by fitting the measured soft-mode phonon dispersion to the empirical formula

$$D(\mathbf{k} = 0, k_z) = M \left[\omega_0^2 - \omega_1^2 e^{-\frac{\alpha_1^2 k_z^2}{2}} - \omega_2^2 e^{-\frac{\alpha_2^2 k_z^2}{2}} \right], \tag{2.27}$$

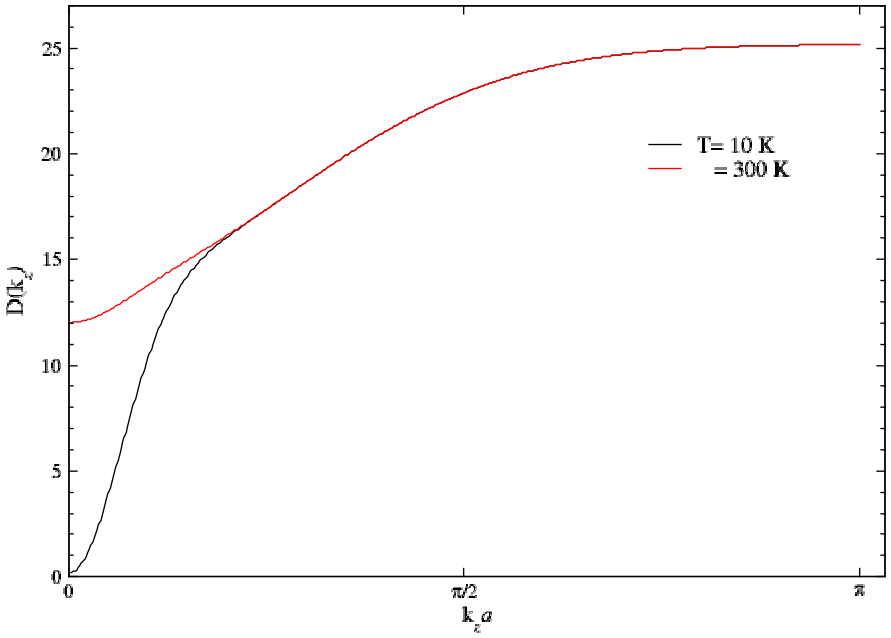

Figure 2.2: Equation (2.27) as function of k_z at low (10 K), and high (300 K) temperatures.

where M is the reduced mass for the mode [31], the constants ω_0, ω_1, and α_1 are fitting parameters used to reproduce the measured phonon dispersion, and ω_2 and α_2 are used to fit the low temperature phonon dispersion, shown in Table 2.1 . This formula was originally proposed by Khalsa and MacDonald [31].

In our model, we propose that ω_2 is responsible for the temperature dependence of $D(\mathbf{k})$ at $\mathbf{k} = 0$, and accordingly, we obtain a formula (Appendix B) for ω_2 as a function of temperature

$$\omega_2^2 = \omega_0^2 - \omega_1^2 - \frac{Q^2 (T^Q)^\lambda}{M \epsilon_0 a^3 C}, \tag{2.28}$$

where T^Q is an effective temperature, C is a constant, and the power $\lambda = 1.45$ is

chosen to improve the quantitative fit to experiments. Table 2.1 shows the fitting parameters [31]. Figure 2.2 shows Eq. (2.27) at low and high temperatures.

2.4 Local and Nonlocal Dielectric Functions

In the previous section, we introduced the interface model. In the remainder of this chapter, we discuss some of the assumptions behind the model. The dielectric response, Eq. (2.25), contains both nonlocal and nonlinear contributions to the polarization. The nonlinearity has been discussed previously [31, 47, 43] and was generally found to be important only near the interface for $\sigma^s \geq 10^{14}\ e/\mathrm{cm}^2$, consistent with our findings in Chapter 3. The nonlocal contribution to the polarization has been included previously only by Khalsa and MacDonald [31]. Other studies such as [43] included only the local dielectric response, due to its simplicity in calculations. Here, we illustrate the importance of the nonlocal response by comparing to a local dielectric model.

We compare the charge density profile obtained from the nonlocal matrix of force constants $D_{i_z j_z}$, defined previously, with the one obtained from a local matrix $\tilde{D}_{i_z j_z} = \tilde{D}_{i_z}\delta_{i_z,j_z}$. For purposes of comparison, we choose $\tilde{D}_{i_z}$ such that it gives the same linear response for a uniform electric field as $D_{i_z j_z}$. If the electric field E_{l_z} and normal coordinate u_{j_z} are independent of position in Eq. (2.25), we obtain in the weak-field limit

$$\begin{aligned} QE &= \sum_{j_z} D_{i_z j_z} u \\ &= D_{k_z=0} u, \end{aligned} \tag{2.29}$$

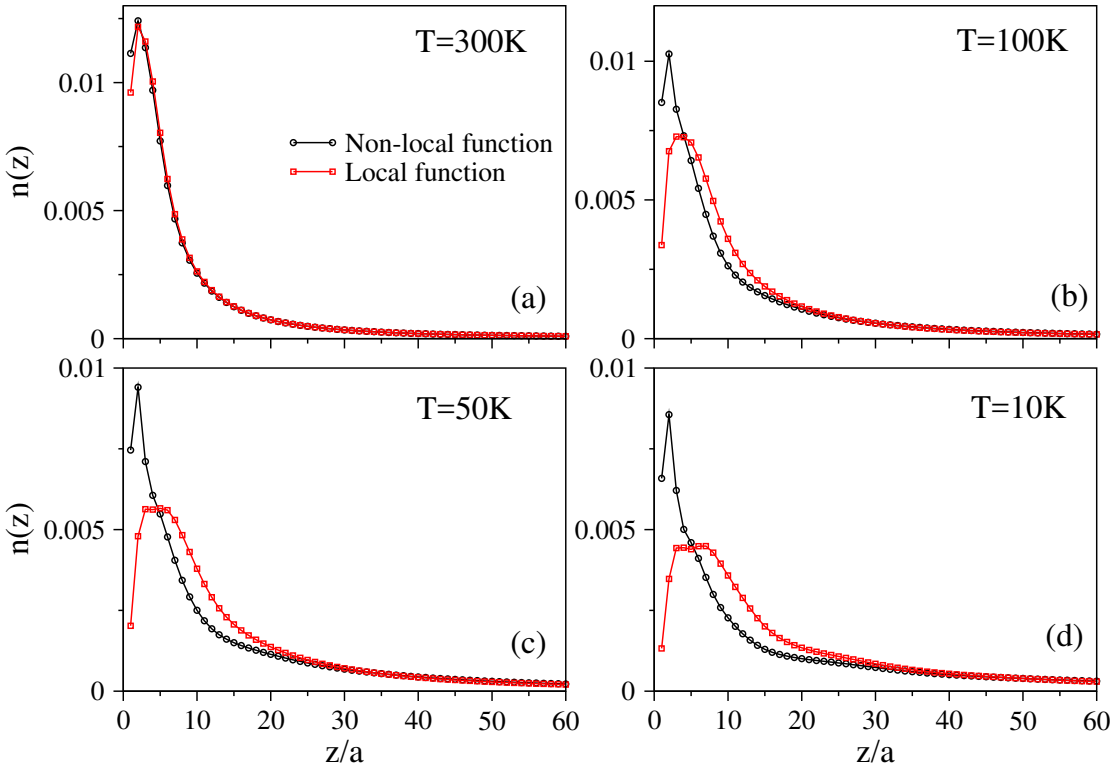

Figure 2.3: Comparison of local and nonlocal models for the dielectric response. The charge density (n(z) per unit cell with $z = i_z a$) profile for the two models is shown at temperatures (a) $T = 300$ K, (b) 100 K, (c) 50 K, and (d) 10 K with $\sigma^s = 0.1e/a^2$. The first 60 layers of an $L = 200$ layer thick STO slab are shown.

and we therefore define $\tilde{D}_{i_z} = D_{k_z=0}$.

Figure 2.3 shows the charge density profile (calculated as described in sec. 2.5) at different temperatures for local and nonlocal force constants. At 300 K, the two give nearly the same charge density profile [Fig. 2.3(a)]. However, as the temperature is lowered, charge moves away from the interface more rapidly for the local case than for the nonlocal case [Fig. 2.3(b)-(d)]. Far from the interface, both cases yield nearly identical results as found in Ref. [43]; this is because we defined $\tilde{D}_{i_z}$ such that it gives same homogeneous response as $D_{i_z j_z}$.

The behavior shown in Fig. 2.3 can be understood simply. The dielectric response is connected to a soft optical phonon mode with dispersion $\omega_{\mathbf{k}}$ satisfying $D_{\mathbf{k}} = M\omega_{\mathbf{k}}^2$ where M is the effective mass of the mode. At high temperatures, $\omega_{\mathbf{k}}$ has a relatively smooth dispersion as shown in Fig. 2.2; however the dispersion, and consequently $D_{\mathbf{k}}$, develops a sharp feature at low T as the mode softens near $\mathbf{k} = 0$ [42] [see Fig. 2.2]. From the properties of Fourier transforms, it follows that the range of $D_{i_z j_z}$ is therefore greater at low T than at high T, or equivalently that the response is more local at high T. This accounts for the similarity between the two models at 300 K. The different charge profiles that emerge at low T indicate that the local dielectric function is more effective at screening the electric field in regions where there are strong field gradients.

In summary, Fig. 2.3 shows that the local approximation for $D_{i_z j_z}$ is not suitable at low temperature. Therefore, nonlocal corrections can not be ignored.

2.5 Numerical Calculations

In our calculations, we perform a self-consistency cycle for $\sigma_{i_z}^f$ and $\sigma_{i_z}^b$, which involves solving Eqs. (2.15) and (2.25) for a given electric field to obtain the electron density and lattice polarization, and then updating the electric field from the resulting potential [see Fig. 2.4]. Here, our calculation methodology aims to minimize the computational time and accelerate the self-consistency cycle. There are many factors that influence the calculations such as the number of **k**-points, the thickness of the STO, and the structure of the self-consistency calculations.

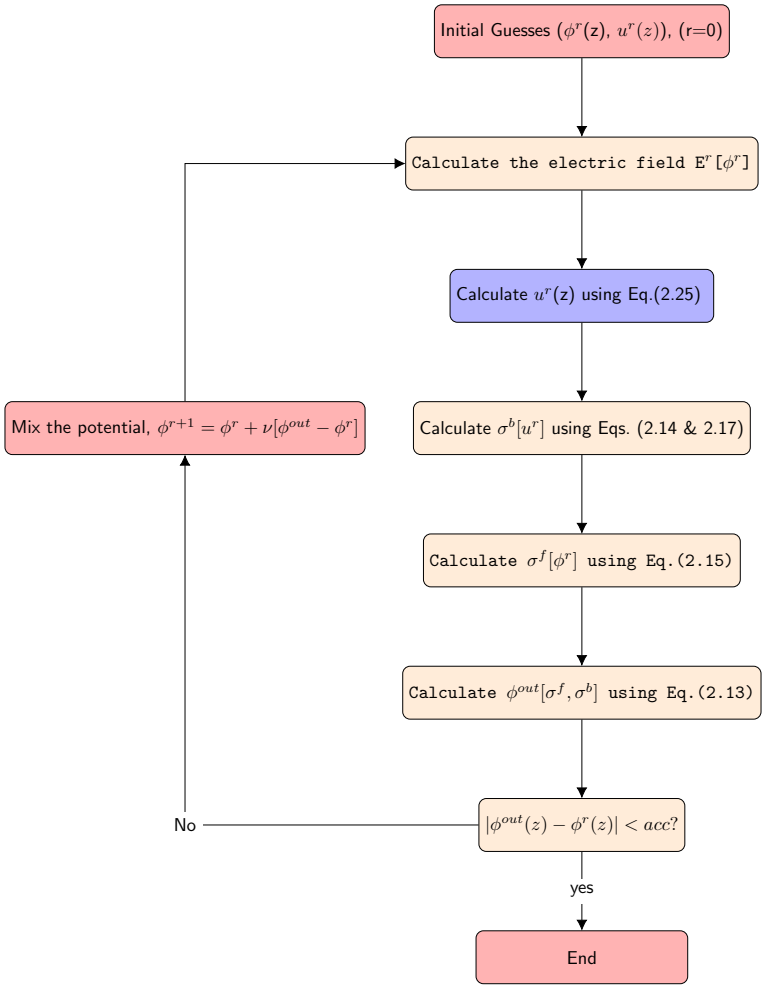

Figure 2.4: Flow chart for self-consistent calculations. Chart shows simple mixing.

2.5.1 Number of k-points and Atomic Spin-Orbit Coupling

To solve Eq. (2.15), we use a LAPACK subroutine (DSYEV) [48] to get the Hamiltonian eigenvalues and eigenvectors. Calling this subroutine for each **k**-point consumes a lot of time, and the number of **k**-points becomes a major factor. However, the k-dependence becomes trivial if we ignore atomic spin-orbit coupling (ASOC). This eliminates mixing of the t_{2g} orbitals and makes the eigenvectors independent of **k**

[49, 50, 31, 36]. (The derivation of the ASOC term is shown in Appendix C.) Ignoring the contributions to the Hamiltonian that mix different orbital symmetries means that each band has a well-defined orbital character. As a consequence, the band index n can be written in the form $\tilde{n}\alpha$ where α is one of xy, xz, or yz and $\tilde{n}$ is an integer labeling bands of type α (the $1xy$ band is the lowest-energy xy orbital character band, etc.) [see Fig. 2.5.(a) and (c)].

Figure 2.5 compares the band structure for the STO thin film with and without ASOC at low doping ($\sigma^s = 0.03$ e/a^2) and intermediate doping ($\sigma^s = 0.1$ e/a^2). We performed theses calculations at low temperature (T=10 K) and with the strength of the ASOC set to ξ_{SOC}= 19.3 meV [36].

Figure 2.5.(a) and (c) show the band structure without ASOC. The key features of these figures are (i) the lowest-energy band has xy character, (ii) as the doping increases, the $1xy$ band splits from the other bands, which form a quasi-continuum. These features will be discussed at length in Chapter 3.

Figure 2.5.(b) and (d) show that, while the details of the band structure are modified by ASOC, the two key features listed above are not. For this reason, ignoring ASOC in our calculations does not affect our conclusions in Chapter 3.

We ignore also Rashba spin-orbit coupling in our calculations. Caviglia et. al [50] found that there is Rashba SOC. Its strength depends on gate voltage, and is maximum near the Lifshitz transition. Zhong et. al [36] showed that the Rashba SOC comes from a combination of ASOC and lattice deformations at the interface. The calculated spin splitting is only a few meV, but becomes important for transport when the Fermi level lies near the bottom of a sub-band with low weight at the interface. Again, the neglect of Rashba SOC will not affect on conclusions in Chapter 3.

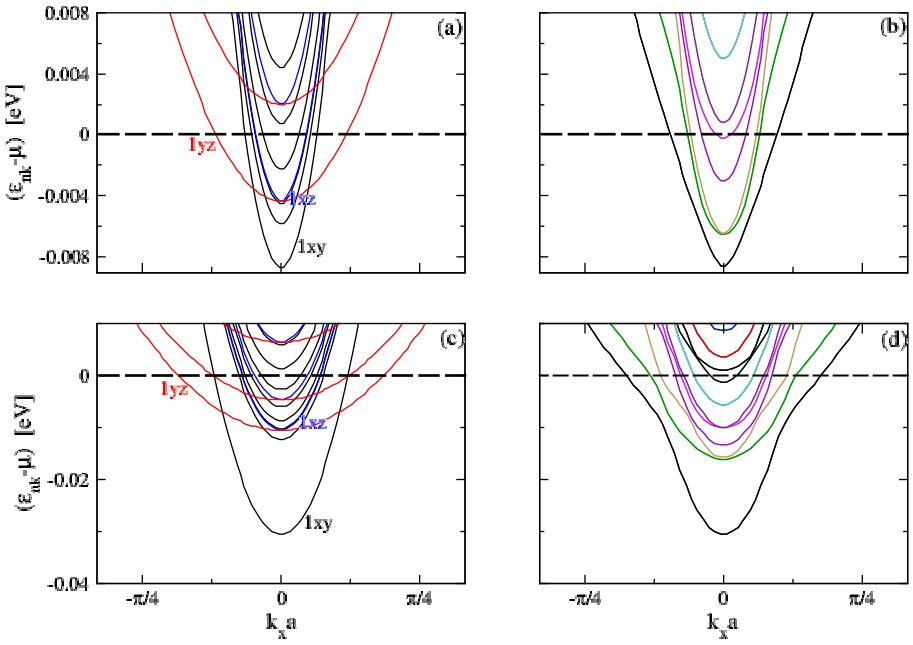

Figure 2.5: (a) and (c) show the band structure for STO thin film without ASOC for doping $\sigma^s = 0.03$ e/a^2 and $\sigma^s = 0.1$ e/a^2, respectively. (b) and (d) show the corresponding band structure with ASOC. The results are for a 30-layer STO thin film, with 36 k-points, and at T=10 K.

By ignoring ASOC, we gain a large computational advantage. The lack of orbital mixing leads to a particularly simple form of the Hamiltonian such that the eigenvectors $\psi_{j_z\beta,n}(\mathbf{k})$ are independent of $\mathbf{k}$. In this form, we break the Hamiltonian [Eq. (2.1)] into three terms that are block diagonal in the orbital type α,

$$\hat{H}^{\text{eff}} = \sum_{i_z,j_z} \sum_{\mathbf{k}} \sum_{\alpha\sigma} c^{\dagger}_{i_z\mathbf{k}\alpha\sigma} [H^{\text{eff}}_{\alpha}] c_{j_z\mathbf{k}\alpha\sigma}, \tag{2.30}$$

with

$$H_\alpha^{\text{eff}} = H_{1\alpha} + H_{2\alpha}(\mathbf{k}), \tag{2.31}$$

where $H_{1\alpha}$ is k-independent, but depends on the layer potentials

$$H_{1\alpha} = \begin{bmatrix} \phi_1 & -t & 0 & \dots & \\ t & \phi_2 & 0\dots & & \\ & & \ddots & & \\ & & & -t & \phi_n \end{bmatrix}, \tag{2.32}$$

with ϕ_i the potential in layer i, and t either $t^{\parallel}$ or $t^{\perp}$ depending on orbital type.

$H_{2\alpha}$ is k-dependent, but doesn't depend on the potential

$$H_{2\alpha}(\mathbf{k}) = \epsilon'_\alpha(\mathbf{k}) \begin{bmatrix} 1 & 0 & 0 & \dots & \\ 0 & 1 & 0\dots & & \\ & & \ddots & & \\ & & & 0 & 1 \end{bmatrix}, \tag{2.33}$$

with $\epsilon'_\alpha(\mathbf{k})$ given by Eq. (2.8), and depends on orbital α.

Let $\mathbf{S}$ be the matrix that diagonalizes the Hamiltonian $H_{1\alpha}$, then

$$\mathbf{S}^\dagger[H_{1\alpha} + H_{2\alpha}(\mathbf{k})]\mathbf{S} = \mathbf{S}^\dagger H_{1\alpha}\mathbf{S} + \epsilon'_\alpha(\mathbf{k})\mathbf{S}^\dagger\mathbf{I}\mathbf{S} = \epsilon_{\tilde{n}\alpha} + \epsilon'_\alpha(\mathbf{k})\mathbf{I}, \tag{2.34}$$

where $\mathbf{I}$ is the identity matrix. Thus, once $\mathbf{S}$ and $\epsilon_{\tilde{n}\alpha}$ are obtained from $H_{1\alpha}$, we can obtain eigenvalues for any $\mathbf{k}$ from

$$\epsilon_{\tilde{n}\alpha\mathbf{k}} = \epsilon_{\tilde{n}\alpha} + \epsilon'_\alpha(\mathbf{k}). \tag{2.35}$$

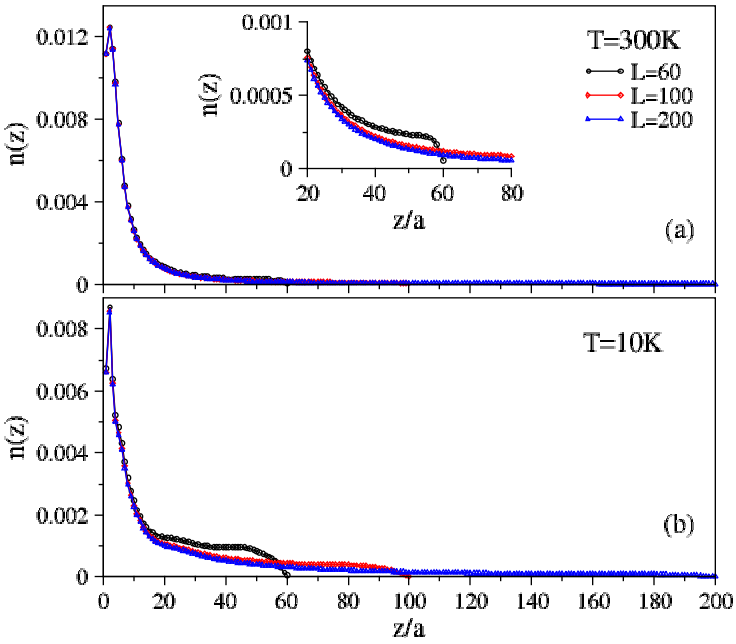

Figure 2.6: Finite-size effects on the electron density $n(z)$, $z = i_z a$. Results are shown for (a) 300 K and (b) 10 K. The electron density is given in units of electrons per unit cell. Results are shown for STO thicknesses of $N = 60$, 100, and 200 layers. The 2D charge density is $\sigma^s = 6.5 \times 10^{13}$ e/cm^2 (corresponding to 0.1 e/a^2). *Inset.* A zoom-in of the charge profile at 300K is shown.

We therefore only need to diagonalize the Hamiltonian once per **k**-sum. The resulting speed-up allows us to study large system sizes of up to 200 layers with 200×200 k-points. By comparison, DFT calculations are typically restricted to small system sizes, in the range of 5 to 30 unit cells, and 8×8 k-points.

2.5.2 Finite-Size Effects: STO Film Thickness

Most previous numerical simulations (including DFT and tight-binding models) have been restricted to a few tens of STO layers, and it is unclear to what extent they are affected by the thickness of the STO slab[29]. Figure 2.6 compares the electron density $n(z)$ inside the STO slab for different slab thicknesses ($L = 60$, 100, and 200 layers) at high and low temperatures. For qualitative purposes, we can divide the charge profile to two regions: one is close to the interface ($z < 10a$) and has most of the total charge, and the other ($z > 10a$) contains a long tail that extends deeply into the STO slab. Near to the interface, the distribution of charges is nearly identical for all thicknesses at 300 K [Fig. 2.6(a)], and depends only weakly on thickness at 10 K [Fig. 2.6(b)]. In contrast, the shape of the long tail changes with the system size, particularly at low T. We note, however, that the total amount of charge in the tail region is roughly independent of slab thickness. Finite-size effects are therefore important when the detailed structure of the tails is of interest.

2.5.3 Anderson Mixing

As mentioned before, the charge density and the normal mode displacement are obtained self-consistently, and both of them depend on each other. This complicates the calculations and makes them numerically unstable [31]. To overcome this problem, mixing methods are often used. Mixing processes, which are known also as acceleration methods, are applied to iterative calculations to improve the rate of convergence. This is especially important given that the convergence of many iterative problems is slow [51]. In our case, we simply do not obtain convergence at all without mixing. We discuss here two methods: simple and Anderson mixing.

In our calculations, simple mixing is applied to the potential energy. In the simple mixing method, the input energy for the forthcoming iteration $(r+1)$ is calculated by linearly mixing the input from the current iteration, ϕ^r, with the output from Eq. (2.13), ϕ^{out}, [see Fig. 2.4]

$$\phi^{r+1} = \phi^r + \nu[\phi^{out} - \phi^r]. \tag{2.36}$$

where ν is the mixing parameter. In Eq. (2.36), $\nu = 0$ means that ϕ^{r+1} is not updated, and $\nu = 1$ means that ϕ^{r+1} is given by Eq. (2.13). Thus, the value of ν in our calculation is between 0 and 1.

We find that simple mixing is useful for small numbers of STO layers and low doping. However, once we increase N or σ^s, the code becomes unstable and does not converge. This leads us to try Anderson mixing. Anderson mixing is a well known method in self-consistent calculations. It obtains ϕ^{r+1} by mixing ϕ^{out} with a small number of previous iterations. This decreases the code instability.

In this method, we construct two $m \times N$ arrays, where N is the number of layers, and m is the number of recent values of ϕ^r and ϕ^{out} to keep (Typically we take $m = 4$). From these, we calculate a so-called optimal input value

$$\bar{\phi^r} = \phi^r + \sum_{i=1}^{m} \theta_i^r (\phi^{r-i} - \phi^r), \tag{2.37}$$

and the associated difference

$$\bar{F^r} = F^r + \sum_{i=1}^{m} \theta_i^r (F^{r-i} - F^r). \tag{2.38}$$

where $F^r = \phi^{out} - \phi^r$ is a measure of how close one is to convergence. The coefficients

θ_i^r are obtained by minimizing the norm $\langle \bar{F}^r | \bar{F}^r \rangle$. Minimizing with respect to θ_i^r leads to the linear equation [52]

$$\sum_{i=1}^{m} \langle F^r - F^{r-j} | F^r - F^{r-i} \rangle \theta_i^r = \langle F^r - F^{r-j} | F^r \rangle \quad \forall_{j=1,\ldots,m}. \tag{2.39}$$

Equation (2.39) is then solved for θ_i^r by using a LAPACK subroutine (dgesv). We linearly combine these two optimal input and difference values to calculate the new input for the subsequent iteration as

$$\phi^{r+1} = \bar{\phi}^r + \nu \bar{F}^r. \tag{2.40}$$

By using this method, we find that our code becomes stable and converges quickly.

2.6 Summary

This chapter discussed the ideal interface model. The model employs a tight-binding approximation for the electrons, in which interactions are treated within a self-consistent field approximation. The electrons couple to the polarization charge density $-\nabla \cdot \mathbf{P}$ where the polarization $\mathbf{P}$ is calculated from a Landau-Devonshire energy that depends explicitly on temperature and electric field. We included both the nonlocal and nonlinear contributions to the polarization. The nonlocal contribution was shown to be important for describing the charge density accurately near the interface.

The main approximation in our model is the neglect of atomic spin-orbit coupling. While details of the band structure are affected by this approximation, the broad trends are not.

Our model ignores also the renormalization of the band masses by electron-phonon

[53] and electron-electron interactions [54], and the effects of antiferrodistortive rotations of the unit cell below temperatures of 105 K [55, 56]. While these will affect our results quantitatively, the qualitative aspects of the results should be robust.

The next chapter, Chapter 3 discusses results for the ideal interface model at different temperatures and doping. In Chapters 4 and 5, the polarization model will be modified to include the effects of structural distortions at the interface.

Chapter 3

Temperature-Dependent Band Structure of Ideal STO Interfaces

This chapter shows and discusses results of the ideal interface model that is given in Chapter 2. First, the temperature-dependence of the charge distribution is described in Sec. 3.1 for low, intermediate, and high electron densities (relative to typical experimental densities). These results are then discussed in the context of the temperature- and doping-dependent band structure in Sec. 3.2. One direct experimental measure of the band structure is angle-resolved photoemission (ARPES), and in Sec. 3.3 we focus on the implications of our calculations for ARPES. Finally, in Sec. 3.4 we propose that 3D tail states, which are ubiquitous in our calculations, form the high-mobility component of the electron gas that is widely observed in magnetotransport experiments.

Early DFT calculations established [34] that the interface breaks the cubic symmetry of the ideal STO lattice, so that a qualitative difference emerges between d_{xy} orbitals (which are oriented parallel to the interface) and $d_{xz/yz}$ orbitals. The hopping amplitude along the z axis is $t^{\perp}$ for d_{xy} orbitals and $t^{\parallel}$ for d_{xz} and d_{yz} orbitals.

Since $t^{\parallel} \sim 10t^{\perp}$, this corresponds to an effective mass along the z direction that is 10 times larger for xy bands (so they are called heavy bands in the z-direction) than for xz or yz bands (so-called light bands in the z-direction). This difference sets the energy ordering of the bands, such that the lowest-energy band has xy symmetry and is tightly confined to within a few unit cells of the interface; the lowest $d_{xz/yz}$ bands are higher in energy and extend farther from the interface.

In an ideal polar catastrophe model, a charge transfer of 0.5 electrons per unit cell is needed to suppress the potential divergence in the polar cap material. The ideal value of 0.5 e/a^2 has been measured for $GdTiO_3$/STO interfaces [57], and only sporadically in LAO/STO interfaces [58, 59]; in most conducting interfaces typical experimental values of the electron density measured by the Hall effect [60, 61] range from 10^{13} to 10^{14} e/cm^2. The charge density can be further modulated by a gate voltage, and we therefore perform calculations for three different doping levels that cover common experimental and theoretical values of the 2D charge density: $\sigma^s = 0.5\ e/a^2$ ($3.3\times10^{14}\ e/\text{cm}^2$), as predicted by the polar catastrophe model; $\sigma^s = 0.1\ e/a^2$ ($6.5 \times 10^{13}\ e/\text{cm}^2$), which is a typical doping found in LAO/STO interfaces; and $\sigma^s = 0.05\ e/a^2$ ($3.3\times10^{13}\ e/\text{cm}^2$), which is approaching the metal insulator transition that is observed at $\sim 10^{13}\ e/\text{cm}^2$. Several calculations have explored the doping dependence of the electronic structure at low T [3, 35, 31, 32, 34], and we observe similar trends with doping in our low-T calculations. The main new results in this chapter refer to how the T-dependence of the electronic structure evolves with doping.

3.1 Effect of Temperature on the Charge Distribution

In this section, we examine the temperature-dependence of the charge distribution for the three representative cases listed above. To minimize finite-size effects, all calculations are for an STO slab of thickness $N = 200$ layers (see Section 2.5.2). We show that there is a pronounced shift of charge density from 2D quantum states that are confined to within ~ 4 nm of the interface into 3D tail states that extend hundreds of unit cells into the STO; the degree of this shift depends strongly on doping.

Figure 3.1(a)-(c) shows the electron density, $n(z) = \sum_\beta n_{i_z\beta}$ (where $z = i_z a$), for 10 K and 300 K and for low (0.05 e/a^2), intermediate (0.1 e/a^2), and high (0.5 e/a^2) electron densities. As we discuss below, the charge distribution is a mix of surface states with strongly 2D character and tails with 3D character. This is particularly evident in the low-T results in Fig. 3.1, which show a clear distinction between surface and tail regions. At high T, the distinction blurs, and $n(z)$ drops off rapidly in the tail region. The crossover between surface and tail occurs at $z \approx 10a$ ($z \approx 4$ nm), and for discussion purposes we divide the profile into region A ($z \leq 10a$) and region B ($z > 10a$). The charge densities n_A and n_B for each region are plotted as a function of T in Fig. 3.1(d)-(f).

There are two key points made by Fig. 3.1. The first is that the fraction of the total electron density in region A depends on σ^s. At 300 K, about 90% of the charge lies in region A for high σ^s, whereas only about half of the total charge lies in region A at low σ^s.

The second point is that, except at the highest doping levels, $n(z)$ depends strongly on T: the charge density near the interface decreases as the temperature is lowered while it increases in the tails. The contrast between low and high charge densities is

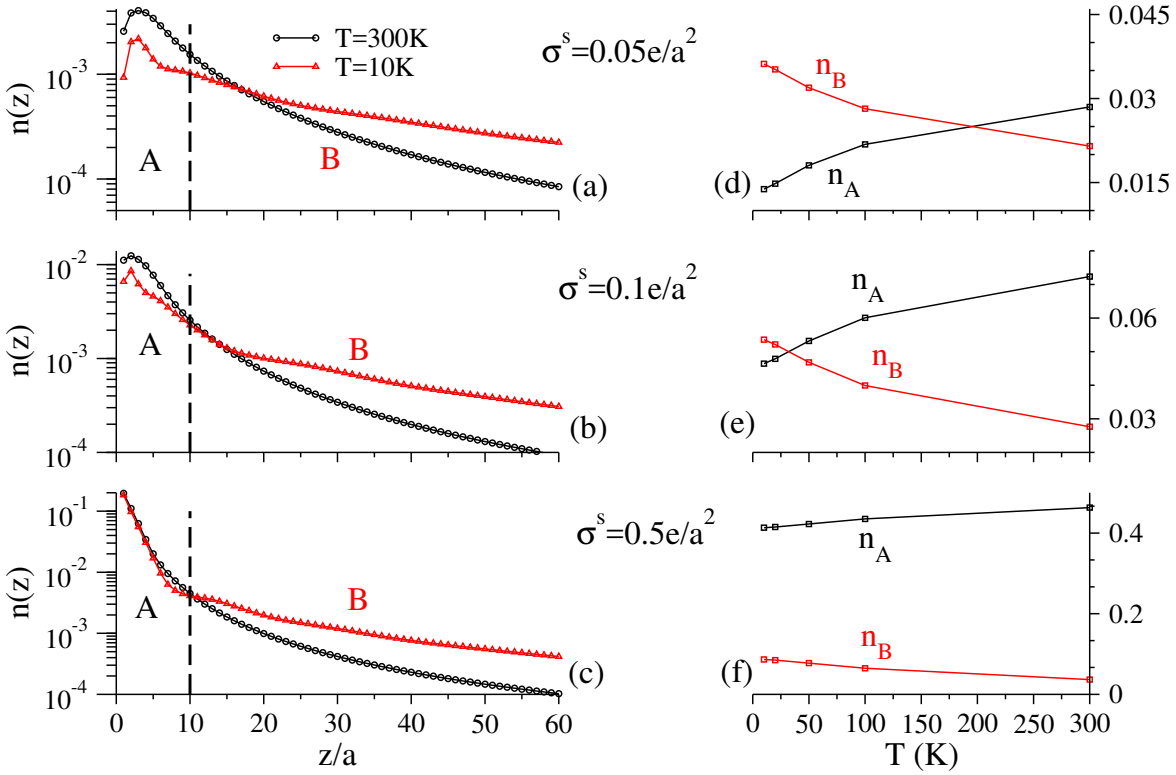

Figure 3.1: Electron density $n(z)$ per unit cell inside an STO slab at different temperatures and dopings. Results are for (a) $\sigma^s = 0.05\ e/a^2$, (b) $0.1\ e/a^2$, and (c) $0.5e/a^2$ at $T = 10$ K and $T = 300$ K. The vertical dashed lines define regions A ($z \leq 10a$) and B ($z > 10a$), which roughly correspond to the interface and tail regions. (d)-(f) The total 2D electron density in regions A and B as a function of temperature. The figure shows the first 60 layers of an $L = 200$ layer STO slab. Figure from [33].

striking: n_A doubles between 300 K and 10 K for low charge density ($\sigma^s = 0.05e/a^2$), but changes by only 10% for high charge density ($\sigma^s = 0.5e/a^2$). Focusing on the middle "typical" value of $\sigma^s = 0.1e/a^2$, we note that about 70% of the total electron density lies in region A at 300 K, in agreement with Ref. [3], and slightly under half remains at 10 K.

One of the most striking features of Fig. 3.1 is that the profile of $n(z)$ near the interface is almost independent of T at the highest charge density, but is strongly

T-dependent at the lowest charge density. This trend is connected to the nonlinearity of the dielectric response in strong electric fields. When σ^s is large, the electric fields near the interface are large, and the nonlinear term ($\gamma u_{l_z}^3$) in Eq. (2.25) dominates the linear term ($\sum_{j_z} D_{l_z j_z} u_{j_z}$). Because we have taken γ to be T-independent, $n(z)$ is also T-independent in this region. The electric field decreases both as one moves away from the interface, and as one decreases σ^s; in both regimes, $n(z)$ becomes temperature-dependent because the nonlinear contribution to the dielectric response is small.

It should be noted that in the nonlinear regime, the lattice polarization due to an electric field is proportional to $\gamma^{-1/3}$ [from Eq. (2.25)], so that γ must change by a relatively large amount to have a significant effect on the charge distribution. Indeed, γ has been measured experimentally[38] below 60 K and was found to be roughly constant down to 30 K, and then to increase by about 50% as the system was further cooled. This corresponds to a change of only 15% in the nonlinear dielectric screening. Unless γ changes significantly at higher T, the assumption of constant γ is reasonable.

To understand better the charge deconfinement that occurs at low temperatures, we plot the electronic potential energy, the electric field, and the polarization at high and low temperatures in Fig. 3.2 for the intermediate value of σ^s. Figure 3.2(a) shows that, in region A, there is a triangular quantum well that confines electrons in 2D quantum states near the interface at all temperatures. In contrast, the potential in region B is strongly temperature dependent, with a crossover from a deep well at high temperature to a nearly flat potential at 10K. This strong T-dependence is connected to the linear dielectric function, which changes by two orders of magnitude between

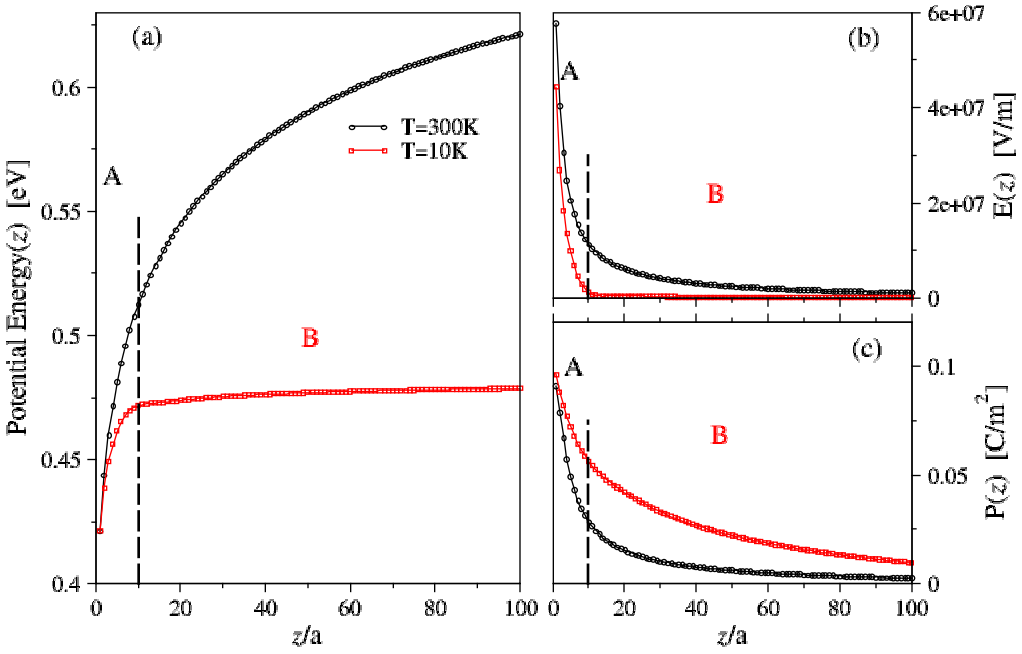

Figure 3.2: Details of the self-consistent solution at low and high temperature for $\sigma^s = 0.1e/a^2$. (a) The self-consistent potential energy, (b) the electric field, and (c) the polarization are shown at 300 K and 10 K. Figure from [33].

300 K ($\epsilon \approx 300\epsilon_0$) and 10 K ($\epsilon \sim 10^4\epsilon_0$).

For comparison, we have performed calculations with a constant permittivity $\epsilon = 300\epsilon_0$ (Fig. 3.3). This is obtained by replacing $\mathbf{P}^{lat}(z)$ by $\epsilon\mathbf{E}(z)$ in Eq. (2.22). As shown in Fig. 3.3, the temperature has no effect at high doping, but it matters at low doping. However, the charge density in Fig. 3.3.(a) is more confined at low temperature, which is opposite to what is shown in Fig. 3.1.(a). This shows that the temperature-dependence in Fig. 3.1.(a) comes mainly from the dielectric function

Because of the large value of ϵ, the electric field is strongly screened in region B

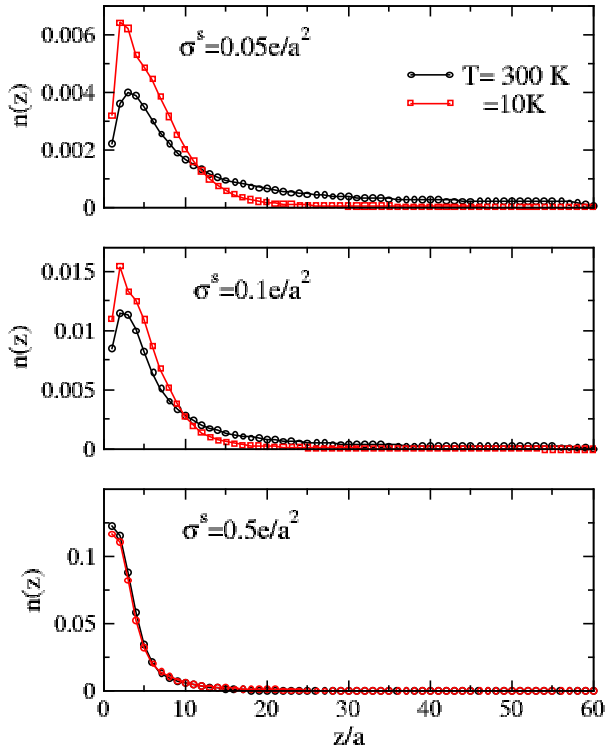

Figure 3.3: Electron density $n(z)$ per unit cell inside an STO slab at different temperatures and dopings with constant $\epsilon = 300\epsilon_0$. Results are for (a) $\sigma^s = 0.05e/a^2$, (b) $0.1e/a^2$, and (c) $0.5e/a^2$ at $T = 10$ K and $T = 300$ K.

at low temperature [Fig. 3.2(b)]. According to Gauss' law,

$$\epsilon_\infty \frac{\partial E(z)}{\partial z} = -en(z) - \frac{\partial P(z)}{\partial z} \tag{3.1}$$

where $P(z)$ is the lattice polarization, $E(z)$ is the electric field, and $\epsilon_\infty = 5.5\epsilon_0$ the

optical dielectric constant. Because the electric field is small in region B, we have

$$en(z) \approx -\frac{\partial P}{\partial z}, \tag{3.2}$$

at $T = 10$ K.

This means that the electric field generated by the conduction electrons in region B is nearly compensated by the lattice polarization. The polarization $P(z)$, which is related to the normal coordinate $u(z)$ for the soft phonon mode by Eq. (2.17), is shown in Fig. 3.2(c). Here, we see that $P(z)$ decays with z more slowly at low T than it does at high T, consistent with enhanced dielectric screening at low T.

For completeness, we plot the charge density for intermediate doping as a function of orbital type in Fig. 3.4. This figure shows that, while the interfacial d_{xy} electron density $n_{xy}(z)$ is weakly temperature dependent, $n_{xz}(z)$ and $n_{yz}(z)$ evolve strongly with T near the interface. In particular, the d_{xz} and d_{yz} bands combined account for 80% of the charge transfer out of the first 10 layers as the temperature decreases. The different sensitivities of $n_{xy}(z)$ and $n_{xz/yz}(z)$ to temperature follow from the different mass anisotropies of the three bands: both the xz and yz bands are light along the z direction while the xy bands are heavy; the xz and yz wavefunctions are therefore more extended along z than the xy wavefunctions. It is unsurprising that the xz and yz bands are most affected as the confining potential weakens when T is reduced.

In summary, we arrive at the following scenario: at room temperature, a majority of electrons is confined to quantum states within ~ 4 nm of the interface by strong electric fields associated with the surface charge σ^s; however, as T is reduced, this electric field is increasingly screened by the dielectric response of the STO, causing a partial deconfinement of the electron gas. This deconfinement is most pronounced

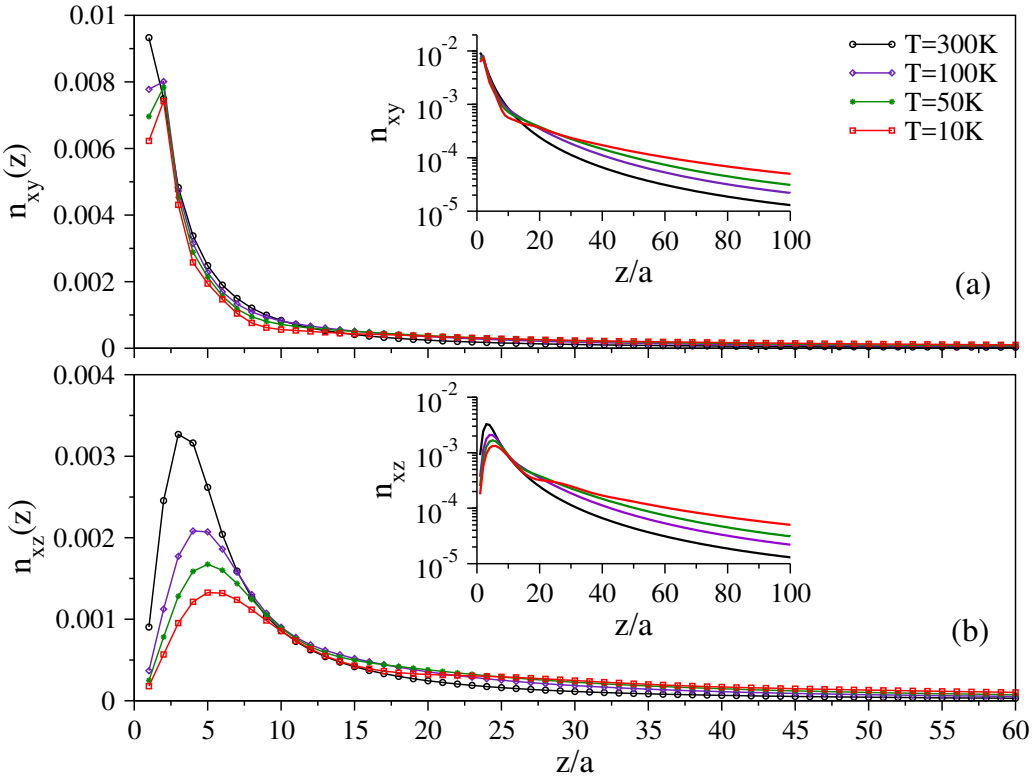

Figure 3.4: Electron density per unit cell $n_\alpha(z)$ for orbital types (a) $\alpha = xy$, and (b) $\alpha = xz$. Results are at temperatures range from 300 K to 10 K. Note that $n_{yz}(z) = n_{xz}(z)$. Insets show the electron density on logarithmic scale. Results are for $\sigma^s = 0.1e/a^2$. Figure from [33].

at the lowest σ^s, where approximately half of the interfacial electron density moves into the tail region. Despite the large fraction of electrons in the tails, the associated electric fields are vanishingly small because of the strong dielectric screening.

3.2 Effect of Temperature on the Band Structure

The temperature-dependent band dispersions $\epsilon_{n\mathbf{k}}$ are shown in Fig. 3.5 for intermediate charge density. The t_{2g} orbital degeneracy is broken by the interface, resulting in multiple orbitally polarized sub-bands.[29] The sub-bands consist of light bands

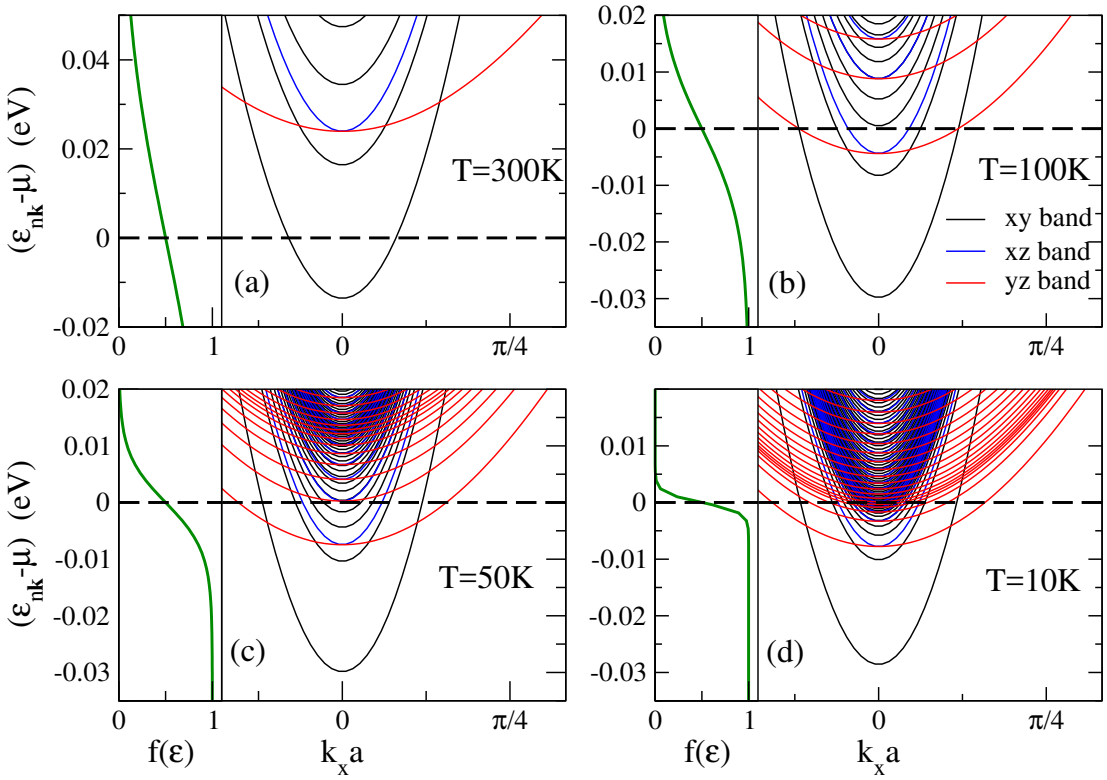

Figure 3.5: Self-consistent band structure along $\mathbf{k} = (k_x, 0)$. Results are for (a) 300 K, (b) 100 K, (c) 50 K, and (d) 10 K, and $\sigma^s = 0.1e/a^2$. The Fermi-Dirac distribution function, $f(\epsilon)$, is shown in each panel (green line). Figure from [33].

(black lines) with d_{xy} orbital character, and two anisotropic bands (blue and red lines) with d_{xz} and d_{yz} orbital character. At all temperatures, the two lowest-energy sub-bands at $\mathbf{k} = 0$ have d_{xy} orbital character, while d_{xz} and d_{yz} sub-bands appear at higher energies. This structure is consistent with previous DFT calculations [35, 36] and with photoemission experiments[62].

Figure 3.5(a) shows the $1xy$, $2xy$, $1xz$, and $1yz$ sub-bands at 300 K. We note that while the chemical potential μ lies below all but the $1xy$ band at 300 K, the thermal energy is sufficient that all bands shown in Fig. 3.5(a) have significant electron occupation. The $1xy$ band has the highest occupancy, containing about 20% of the

total electron density, while the first four bands combined contain approximately half of the total charge.

Two significant changes occur as the temperature is lowered: first, there is a significant shift of μ between 300 K and 100 K; second, while the gap between the $1xy$ and $2xy$ bands evolves very little with T, the spacing between the remaining bands shrinks significantly.

Coincident with this change in the spectrum, there is a shift of the occupied eigenstates towards three-dimensionality. At 300 K, the bands shown in Fig. 3.5(a) have strong 2D character, and the eigenstates are localized within the first 10 STO layers. This is illustrated in Fig. 3.6, which shows the projected weight $|\psi_{j_z\alpha,n}|^2$ of the first few sub-bands. Figure 3.6 shows that the $1xy$ band is localized within 5 layers of the interface at all temperatures, but that the $2xy$ and $1xz/yz$ bands extend twice as far into the STO at 10 K as at 300 K. Higher bands are affected even more by temperature, and the $10xy$ band extends four times as far into the STO at 10 K as it does at 300 K.

The distribution of charge amongst the bands is also T-dependent. At 300 K, 57% of the charge is contained in the first 4 bands ($1xy$, $2xy$, $1xz/yz$); at 10 K, this charge is shared amongst the lowest 5 bands (including $3xy$). Thus, charge spreads away from the interface as T is lowered for two reasons: first, occupied bands become less confined; and second, the density of bands increases, such that higher bands with larger spatial extent become occupied.

In particular, the band structure in Fig. 3.5(d) shows evidence for coexisting 2D and 3D components to the electron gas: states that are confined to the interface region are characterized by bands that are clearly separated from each other at $\mathbf{k} = \mathbf{0}$, while

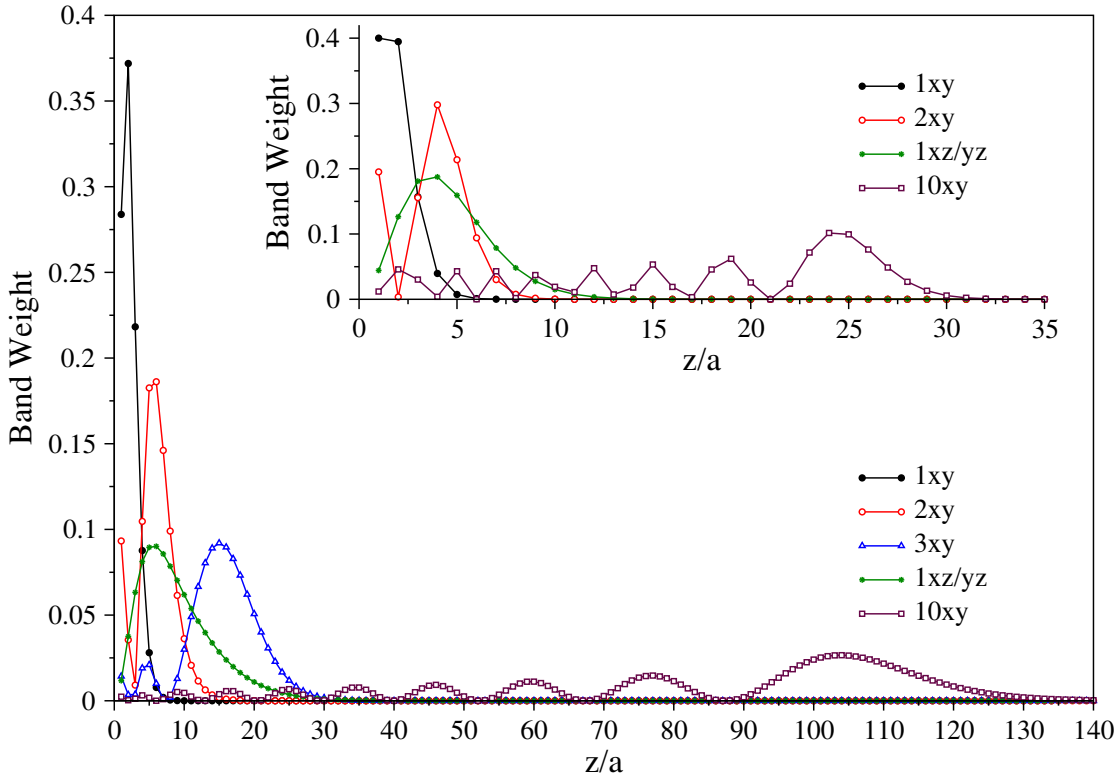

Figure 3.6: Projected band weights at 10 K (main panel) and 300 K (inset). The figure shows the band weights of the lowest five bands at 10 K and the lowest four bands at 300 K; these bands contain slightly more than half of the total charge. For illustration, the band weight of a high-energy $10xy$ band is also shown at each temperature. The projected weight of band n in layer $j_z = z/a$ for orbital type α is $|\psi_{j_z\alpha,n}|^2$, where the $\psi_{j_z\alpha,n}$ is the electronic wavefunction. Note that the xz and yz band weights are the same. Results are for $\sigma^s = 0.1e/a^2$. Figure from [33].

3D states are characterized by a dense continuum of bands. Indeed, we have found that the first half-dozen bands do not change much with the STO slab thickness L, indicative of quantum interface states; however, the sub-band structure at energies $\geq \mu$ becomes denser as N increases, indicating that these states extend to the back wall of the STO slab, even for $N = 200$. Figure 3.5 thus reinforces the narrative that there is a transfer of electrons from 2D quantum states localized within $\sim$ 10 unit

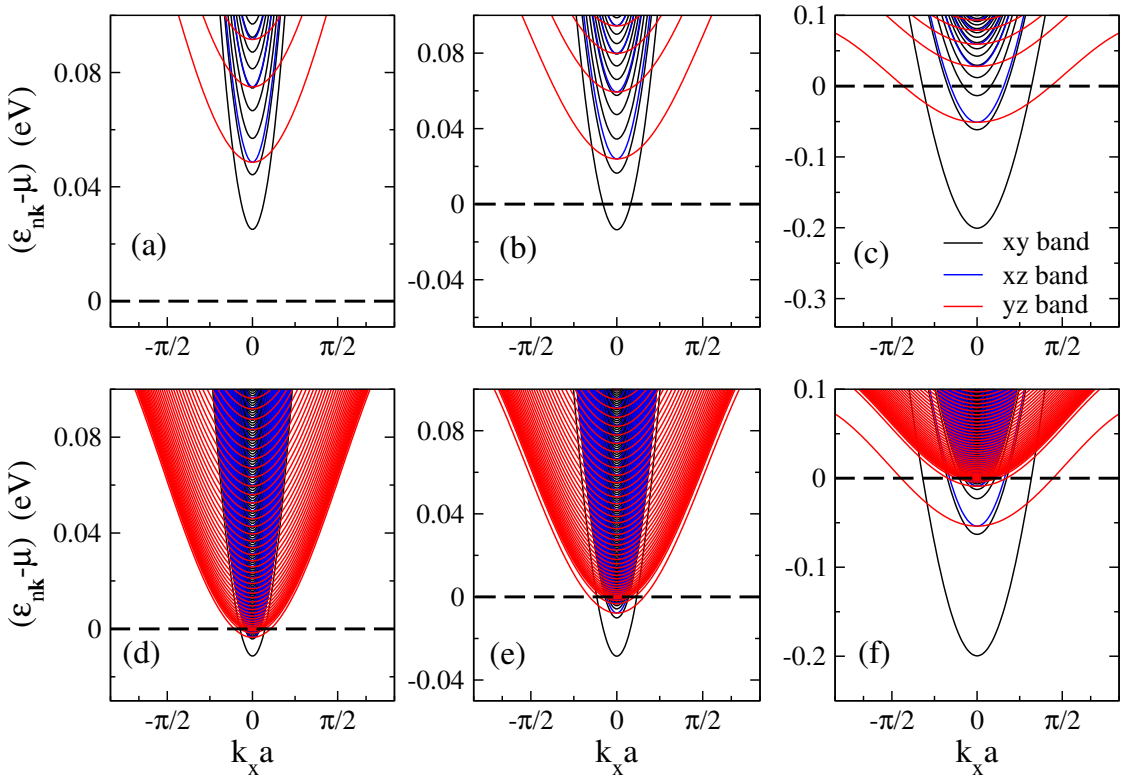

Figure 3.7: Doping- and temperature-dependent band structure of a STO interface. Results are for (a)-(c) 300 K, and (d)-(f) 10 K. Doping levels are (a), (d) $\sigma^s = 0.05e/a^2$; (b), (e) $\sigma^s = 0.1e/a^2$; (c), (f) $\sigma^s = 0.5e/a^2$. Figure from [33].

cells of the interface to extended 3D tails as T is lowered.

Figure 3.7 compares the calculated band structures at low and high temperature for low, intermediate, and high doping. At all electron densities, the visible portions of the spectra comprise a set of distinct bands with 2D character at 300 K. At 10 K, the spectra consist of a small number of low-energy 2D bands that are clearly separated from a 3D continuum with $\epsilon_{n\mathbf{k}} \geq \mu$. The low-energy bands are the source of the interfacial component of the charge density in Fig. 3.1. Consistent with Fig. 3.1, the 2D bands at high doping [Fig. 3.7(c) and (f)] are nearly independent of T.

In summary, we find that there is a discrete spectrum of quantum 2D states that

are confined to within 10 unit cells of the interface, and a higher energy continuum of 3D states that extend hundreds of unit cells into the STO. The principal result of this section is that the 3D states lead to a partial deconfinement of the electrons from the interface at low T, and that this deconfinement becomes more pronounced as the total 2D electron density is reduced.

3.3 Spectral Function

The temperature-dependent band structure can be observed by ARPES, and indeed recent ARPES experiments at low temperature have found features consistent with the predicted band structure.[53, 61] ARPES is a surface-sensitive technique that measures the projection of the spectral function onto the top STO layer; furthermore, photon polarization can be used to selectively probe different orbital symmetries. For direct comparison we therefore calculate $A_{i_z,\alpha}(\omega, \mathbf{k})$, the projected spectral function in layer i_z for orbital type α. This is given by

$$A_{i_z,\alpha}(\omega, \mathbf{k}) = \sum_n |\psi_{i_z\alpha,n}(\mathbf{k})|^2 \delta(\omega - \epsilon_{n\mathbf{k}}), \tag{3.3}$$

where $|\psi_{i_z\alpha,n}(\mathbf{k})|^2$ is the weight of the nth band in layer i_z for orbital type α, and $\epsilon_{n\mathbf{k}}$ is the dispersion of the nth band. The delta-function has a Lorentzian broadening of 0.01 eV, which is comparable to the energy resolution of high-resolution ARPES experiments.

We are principally concerned with two main points about the spectral function: the intensity of the various features of the band structure, which is nominally related to the weight of the different bands at the surface; and the size of the apparent Fermi

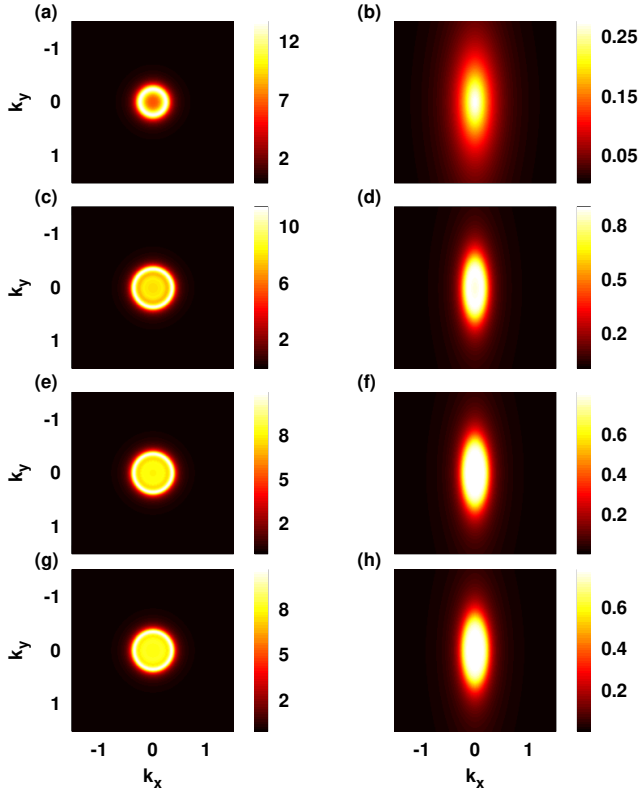

Figure 3.8: Projected spectral function at the interface for quasiparticle energy μ. The left panels show $A_{1,xy}(\mu, \mathbf{k})$ for xy bands at (a) 300 K, (c) 100 K, (e) 50 K, and (g) 10 K. The right panels present the corresponding spectral function $A_{1,xz}(\mu, \mathbf{k})$. Results are for $\sigma^s = 0.1e/a^2$. Figure from [33].

surfaces, which is nominally related to the filling of each band. Because both the band weight and band dispersion change with temperature, as shown in Figs. 3.5 and 3.6, we expect that the projected spectral function must also change with temperature.

We begin with the case of intermediate electron density. Figure 3.8 shows the temperature-dependent spectral function $A_{1,\alpha}(\mu, \mathbf{k})$ at the interface ($i_z = 1$) for quasiparticles at the electrochemical potential μ. The left panels present the evolution of the projected spectral function for the xy bands; the right panels show the corresponding spectral function for the xz bands. (The spectral functions for the yz bands

can be obtained by rotating the xz image by $\pi/2$.)

At 300 K, we observe an intense ring with xy symmetry, corresponding to the $1xy$ band [Fig. 3.8(a)], and a very weak cigar-shaped feature associated with the $1xz$ band [Fig. 3.8(b)]. The disparity between the xy and xz/yz intensities is consistent with the fact that only the $1xy$ band crosses μ at this high temperature. Indeed, the bottom of the $1xz$ band is ~ 0.035 eV above μ, and is only observable in Fig. 3.8(b) because of the finite energy resolution in Eq. (3.3).

At 100 K, the intensity of the $1xy$ band decreases slightly, and an intense disk centered at $\mathbf{k} = \mathbf{0}$ appears [Fig. 3.8(c)]. This change in the spectral function reflects both changes in the band structure and a shift of the chemical potential to higher energies [c.f. Fig. 3.5(b) and (c)]. At this temperature, multiple xy bands pass within 0.01 eV of the chemical potential; while the $1xy$ band appears as a distinct ring, these remaining xy bands blur together to form a disk. The $1xz$ band [Fig. 3.8(d)] continues to be an order of magnitude less intense than the xy bands, despite the fact that the $1xz$ band dispersion crosses μ at 100 K. This is because of the small weight of the $1xz$ band at the interface [Fig. 3.6].

Below 50 K, the intensity of the $1xy$ ring does not change [Fig. 3.8(e) and (g)], but the disk intensity increases slightly because higher energy xy bands shift downwards as T decreases, as shown in Figs. 3.5(c) and (d). At the lowest temperatures, this disk represents the projection of the 3D tail states onto the surface. The intensity of the xz bands remains an order of magnitude smaller than that of the xy bands [Fig. 3.8(f)]. There is very little change to the apparent spectrum below 50 K.

Focusing on bands of xy symmetry, we note that the apparent filling as determined from the area of the $1xy$ ring is temperature-dependent, and changes by $\sim$ 20%

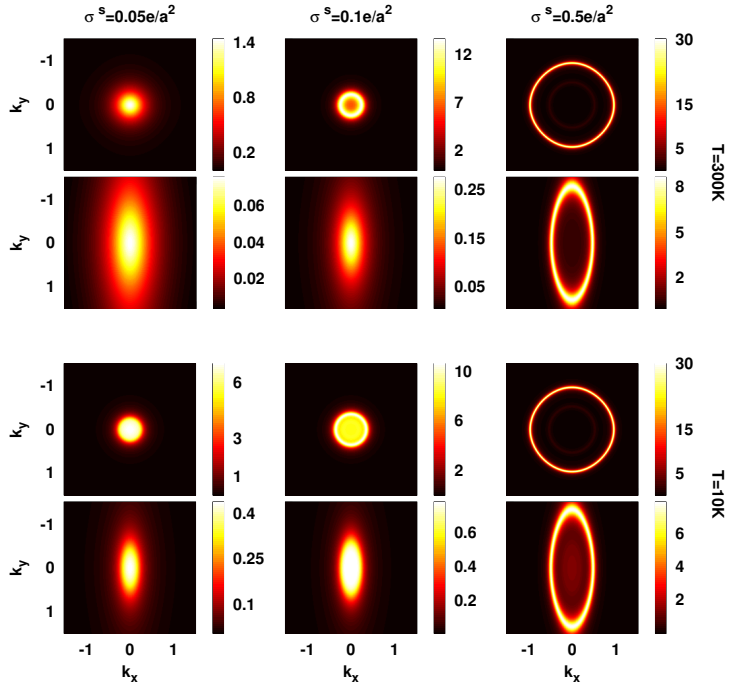

Figure 3.9: Projected spectral function at low, intermediate, and high electron densities, and at $T = 10$ K and $T = 300$ K. Results are shown for xy bands (rows 1 and 3) and xz bands (rows 2 and 4) bands. Figure from [33].

between 300 K and 100 K. This change does not reflect a 20% change in the filling of the $1xy$ band however, because of the rather large change in μ, which shifts upwards by almost 0.02 eV as T is lowered. Below 100 K, the ring's surface area does not significantly change with temperature.

Next, the doping-dependence of the spectral function is shown in Fig. 3.9. As expected, the surface area of the bands increases with σ^s, in agreement with Ref. [61]; however, it is the temperature-dependence of the intensity that is most striking. The spectral function is almost independent of T at $\sigma^s = 0.5e/a^2$, which is a direct result of the strongly nonlinear dielectric response in the interface region at high doping. In contrast, at low doping, the intensity of the spectral function at μ is strongly T-dependent, primarily because of the strong T-dependence of the chemical

potential.

Several groups have performed ARPES experiments on STO interfaces at low temperatures, and the shapes and surface areas of our calculations are in good agreement with the measured Fermi surfaces for approximately the same doping.[63, 61, 53] Notably the xz (and yz) bands are more than an order of magnitude weaker than the xy bands in our calculations; and while the relative intensities of the bands observed in ARPES depend on matrix elements, the $d_{xz/yz}$ bands are indeed considerably weaker than the d_{xy} bands.[63]

In summary, our calculations agree with ARPES experiments at low temperatures, and we make two predictions regarding spectral function $A_{1,\alpha}(\mu, \mathbf{k})$ at high temperatures: first that the area of the $1xy$ ring should shrink as T is raised above 100 K; and second that the intensity of the $d_{xz/yz}$ bands should drop dramatically above 100 K.

3.4 Discussion

Unlike conventional semiconductors, the STO dielectric function is strongly temperature- and electric field-dependent. This leads to counterintuitive behavior at STO interfaces; namely, that the electron gas is more strongly confined at high temperatures and electron densities than at low temperatures and electron densities. Consequently, our calculations make predictions that differ from commonly held views regarding the electron distribution in STO interfaces. The conventional view is that the electronic properties are dominated by quantum 2D states, and indeed experiments find that the majority of the charge is bound to within ~ 10 nm of the interface [64, 3, 65, 60]. Measurements of the nonlinear Hall coefficient have been modeled by two occupied

sub-bands: a low-mobility band containing most of the conduction electrons, and a high-mobility band containing a minority of carriers. The mobilities of the two components vary from sample to sample, and may differ by orders of magnitude [66, 67, 59, 68, 58]. While the two-band interpretation is conceptually useful, it has been noted that inconsistencies within the two-band analysis suggest a more complicated band structure [66]. At low electron densities, the picture is clearer: experiments have found a Lifshitz transition near electron densities of 1.5×10^{13} cm^{-2} [66], which is slightly above the metal-insulator transition at $\approx 10^{13}$ cm^{-2}. Below the Lifshitz transition, the magnetic field-dependence of the Hall resistivity is linear, indicating that only a single band is occupied. A full discussion of the Lifshitz transition is presented in the following chapter.

In contrast, the results reported in this chapter find a large number of occupied bands at all doping levels, similar to previous calculations [3, 35, 31, 32]. A significant fraction of the occupied bands corresponds to the quasi-3D tail states that extend hundreds of unit cells into the STO substrate. While the fraction of charge contained in the tails is small at high electron densities, it is over 50% at low electron densities (Fig. 3.1). Perhaps more interestingly, we have found a strong temperature dependence to the charge distribution at intermediate electron densities, with a pronounced shift of charge into the tails as T is lowered. The general trend that the charge spreads out as T decreases was observed experimentally [3]; however, experimental confirmation of quasi-3D tails remains lacking. Indeed, direct observation of the tails may be difficult because, except at the lowest doping levels, the electron density $n(z)$ in the tails is at least an order of magnitude smaller than in the 2D component of the electron gas (Fig. 3.1).

The tails may be most relevant to transport experiments, since interfacial disorder (eg. cation intermixing) is thought to severely reduce the mobility of 2D states near the interface. A proper comparison between theory and experiment requires a detailed disorder model, which is beyond the scope of this work. Nonetheless, we can make a few simple observations based on a crude model for the mobility μ_n of the first few bands ($n = 1xy,\ 1xz/yz,\ 2xy$). This model assumes that interfacial disorder (eg. cation intermixing) is the dominant scattering mechanism and that interband scattering can be neglected. These assumptions break down at low doping, first because the interband spacing becomes less than the scattering rate, and second because low-lying bands become part of the 3D continuum and are therefore subject to scattering by defects in the STO substrate. The model is also limited because it provides no information about the mobility of the 3D tails. For qualitative purposes, however, we can assume that the tails behave similarly to bulk STO.

The simplest ansatz is to take a quenched disorder model in which the Ti site potentials in the first Λ STO layers adjacent to the interface are chosen from a random box-distribution of width W. Experimentally, cation intermixing is found to extend over a few unit cells,[19] and for concreteness, we arbitrarily take $W = 1$ eV and $\Lambda = 2$; however, the qualitative results do not depend strongly on this choice. Within a Born approximation the electron lifetime τ_n in band n [Appendix D] is

$$\frac{\hbar}{\tau_n} = \frac{\sqrt{m_{x,n}m_{y,n}}W^2a^2}{24\hbar^2}\sum_{i_z=1}^{\Lambda}|\Psi_{i_z\alpha,n}|^2, \tag{3.4}$$

where $m_{x,n}$ and $m_{y,n}$ are effective mass components for band n. The mobility for transport in the x-direction is $\mu_n = e\tau_n/m_{x,n}$. The absolute values of the mobility, which depend on our arbitrary choice of W, are not especially meaningful; however,

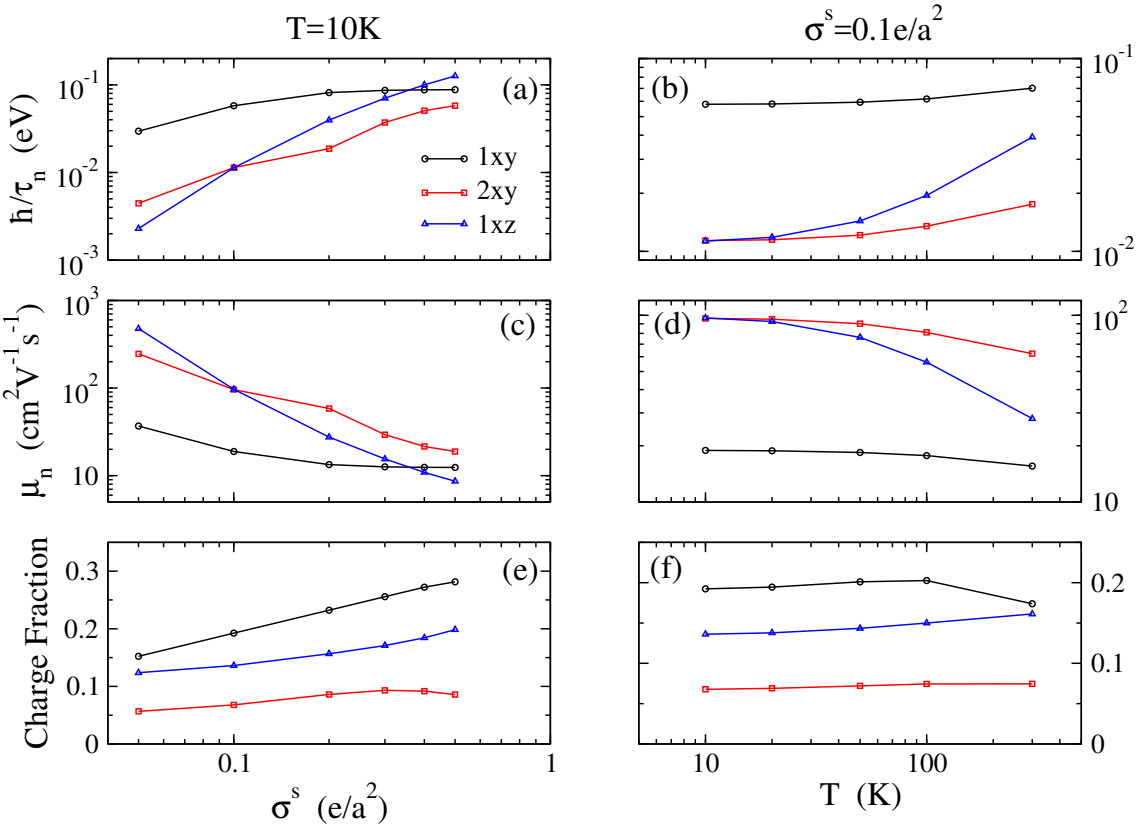

Figure 3.10: Transport properties of 2D interface states as a function of (a), (c), (e) 2D charge density at fixed temperature, and (b), (d), (f) temperature at fixed 2D charge density. (a), (b) Scattering rate $\hbar/\tau_n$; (c), (d) mobility μ_n; and (e), (f) fraction of the total charge in band n for $n = 1xy$, $2xy$, and $1xz$. The calculations assume that elastic scattering comes predominantly from interfacial disorder (eg. cation intermixing), and that interband scattering process can be neglected. Contributions from the 3D tails are not included in this figure. Figure from [33].

the trends with doping and temperature shown in Fig. 3.10 are.

Equation (D.10) shows that individual bands' scattering rates depend on the projected band weight $|\Psi_{i_z\alpha,n}|^2$ onto layers adjacent to the interface. Two clear trends in Fig. 3.10, namely that μ_n increases when either σ^s or T is reduced, can be traced back to shifts of the band weight away from the interface (recall, for example, Fig. 3.6).

Similarly, Fig. 3.10 shows that at fixed T and σ^s the mobilities of different 2D bands may differ by an order of magnitude or more because of they have different band weights at the interface.

While significant, the differences in mobilities between bands that are shown in Fig. 3.10 are much less than the three orders of magnitude difference between high- and low-mobility electrons reported in Refs. [58, 59]. Those experiments instead suggest that the two electronic components live in different environments. With this in mind, we speculate that the low-density high-mobility component of the electron gas observed over a wide range of electron dopings [66, 67, 59, 68, 58], may in fact correspond to the 3D tails in our calculations. These tails have very little overlap with the interface, and the scattering of conduction electrons will be determined by the defect density in the STO substrate. The remaining high-density low-mobility component of the electron gas then must correspond to the 2D interface states, whose mobility is limited by interfacial disorder. We point to three experimental observations that are broadly consistent with this proposed scenario:

- First, our calculated charge densities in the interface and tail regions roughly correspond to the observed fractions of low and high mobility charges. Ref. [58] reports that for high electron densities, the high-mobility component of their electron gas comprises less than 10% of the total electron density, while Ref. [67] found that at intermediate densities the high-mobility component contains a third of the total electron density. Similarly, Fig. 3.1 shows that the fraction of the total charge in the tail region at 10 K rises from less than 10% at high electron density to roughly 50% at intermediate density.

- Second, the predicted temperature dependence of the mobility is qualitatively

consistent with available experiments. At intermediate electron densities, Ref. [67] found that the conductivity of the high-density component is nearly independent of T (up to 30 K), while the conductivity of the low-density component drops by an order of magnitude. Similarly, Fig. 3.10 shows that the mobilities of the interface states are almost constant between 10 K and 30 K, owing to modest changes in the confinement of their wavefunctions to the interface. Conversely, we expect the tail states to exhibit a strong temperature-dependence, assuming that they follow the behavior of bulk STO [69, 70].

- Third, at low electron densities, Ref. [66] argued that the chemical potential is pinned to the bottom of a heavy band that acts as a charge reservoir. They speculated that this reservoir consists of interfacial $d_{xz/yz}$ bands; however, our calculations find that at 10 K the chemical potential is pinned to the bottom of the quasi-3D tail bands (Fig. 3.7). Because the density of states in the tails is extremely high compared to the 2D interface states, we argue that the tails provide a more natural explanation for the observed charge reservoir.

We note that there are open questions that are not addressed by the simple arguments presented here. Our model does not predict the Lifshitz transition observed by Ref. [66] at low electron density, for example. Instead, the $1xy$ band in our calculations continuously merges with the 3D continuum as the electron density is lowered. In the next chapter, we discuss how to modify our dielectric model to obtain the observed Lifshitz transition.

In summary, we have explored the temperature-dependent band structure of ideal interface model. The calculations presented in this chapter suggest a significant role for quasi-3D tail states, contrary to a widely held perception that the interfaces are

dominated by 2D states. These tail states extend hundreds of unit cells into the STO substrate, and are extremely sensitive to both electron doping and temperature. We have shown that photoemission experiments can be used to probe the temperature-dependent band structure; however, the tail states exist far from the interface and are therefore invisible to ARPES. We speculate, however, that the tail states are key to understanding transport experiments, and have provided some qualitative evidence to support this idea.

Chapter 4

Effect of a dead layer on the doping-dependent band structure

This chapter is motivated by recent experiments that show there is a Lifshitz transition in LAO/STO interfaces [66, 71, 72, 73]. We start the chapter by introducing the Lifshitz transition, and the experiments that observed it. Then, we explore the doping-dependent band structure in the case of an ideal-interface model and show that it does not reproduce the observed Lifshitz transition. Next, we introduce a dielectric dead layer to our model, and repeat the calculations. Finally, we compare our results with experiments.

4.1 The Lifshitz Transition

The previous chapter studied the effect of the STO dielectric function on the electronic properties of 2DEGs at STO interfaces. We found that the calculated band structure has a mix of 2D states that are tightly bound to the interface, and quasi-3D states that extend into the STO substrate. As the temperature is lowered, the charges spread out into the STO bulk into a quasi-3D tail. This spreading is less important

at high electron densities, but becomes substantial at low densities.

The low-density regime, defined here as σ^s =0.01– 0.1e/a^2, has recently attracted attention due to the existence of fascinating properties such as superconductivity [14, 74], strong spin-orbit coupling [50], and an observed Lifshitz transition [66]. In this regime in particular, near the Lifshitz transition, it was reported that the superconducting transition temperature and spin-orbit coupling strength are maximum [50, 66, 75, 73].

A Lifshitz transition is defined as an abrupt change of topology of a Fermi surface [76]. To our knowledge, the Lifshiz transition in STO-based interfaces was first mentioned in Ref. [66] by Joshua and co-workers. In their work, the response of the LAO/STO system to a magnetic field at different back-gate voltages (V_G) was measured. They showed that there is a critical gate voltage (V_C) at which the magnetotransport properties abruptly change. When $V_G < V_C$, the Hall resistivity, ρ_{xy}, changes linearly with magnetic field (B), while at $V_G \geq V_C$, ρ_{xy} changes non-linearly with the field. A nonlinear Hall effect suggests multiple types of carriers. Therefore, the experiment suggests the Lifshitz transition is a transition from a single Fermi surface to multiple Fermi surfaces.

These experiments are typically interpreted with a two-band model in which the Hall resistivity as a function of magnetic field is [46, p. 240]

$$\rho_{xy} = \frac{B}{e}\frac{(n_1\mu_1^2 + n_2\mu_2^2) + (\mu_1\mu_2 B)^2(n_1 + n_2)}{(n_1\mu_1 + n_2\mu_2)^2 + (\mu_1\mu_2 B)^2(n_1 + n_2)^2}, \tag{4.1}$$

with $n_1(n_2)$, and $\mu_1(\mu_2)$ the charge densities and mobilities of the two types of carriers respectively, and B is the magnetic field. When $n_2 = 0$, ρ_{xy} reduces to the usual Hall resistivity, $\rho_{xy} = \frac{B}{en_1}$, which is linear in B as expected.

The extracted charge density as a function of gate voltage is shown in Fig. 4.1, which is adopted from Ref. [72]. The authors applied a top-gate voltage to the LAO/STO interface. They fitted the transverse (σ_{xy}) and longitudinal (σ_{xx}) conductivity to the two-band expressions

$$\sigma_{xy} = eB\frac{(n_1\mu_1^2 + n_2\mu_2^2) + (\mu_1\mu_2 B)^2(n_1 + n_2)}{(1+\mu_1^2B^2)(1+\mu_2^2B^2)}, \tag{4.2}$$

$$\sigma_{xx} = e\frac{(n_1\mu_1 + n_2\mu_2) + (\mu_1\mu_2 B^2)(n_1\mu_2 + n_2\mu_1)}{(1+\mu_1^2B^2)(1+\mu_2^2B^2)}. \tag{4.3}$$

From this, they get the charge densities n_1 and n_2 as a function of gate voltage.

At $V_G < V_C$ the density of electrons n_1 grows with gate voltage and is equal to the total density $n_{total} = n_1 + n_2$ because n_2 here is nearly zero. At V_C, n_1 deviates from n_{total} and n_2 starts to rise. This marks the Lifshitz transition, and the corresponding charge density at V_C is the Lifshitz density $n_L \sim 2.9 \times 10^{13}$ cm^{-2}. At $V_G > V_C$, n_2 increases with gate voltage, and n_1 decreases. Indeed, there are two main features in Fig. 4.1: one is that there is a single Liftshitz transition; second is that there is an abrupt change in the slope of n_1 after the transition. The main goal of the remainder of this thesis is to explain these features.

Most of the experiments that observed the Lifshitz transition [66, 75, 71] reported nearly the same behaviour of charge density with gate voltage. The differences between these experiments are in the value of n_L, and the slope of n_1 after the transition. For example, Ref. [66] suggested that n_L is a universal value and is equal to 1.6×10^{13} cm^{-2}. However, it was found later that n_L does depend on multiple factors, such as whether the interface is back- or top-gated, the growth conditions, and the cap material[75, 71]. n_L is now found to lie in a range $1.6 - 4 \times 10^{13}$ cm^{-2}

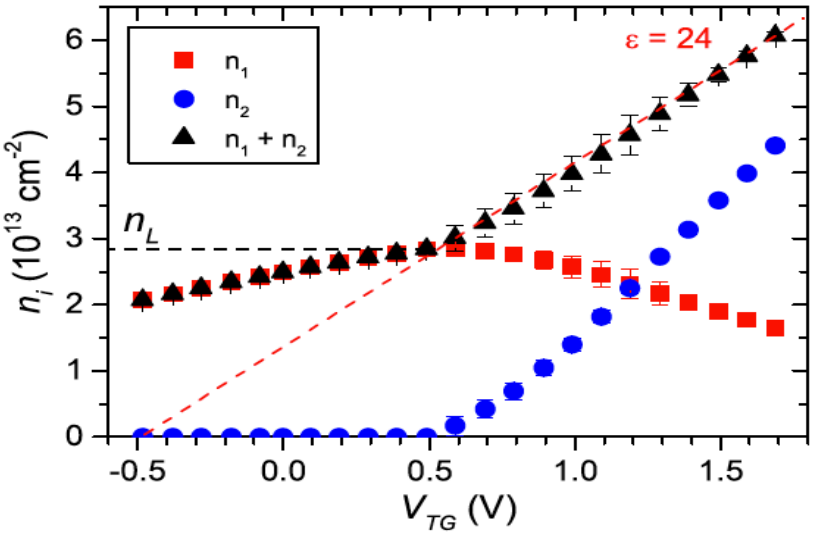

Figure 4.1: The extracted charge density versus top-gate voltage (V_{TG}) at T=2 K. The black dashed line indicates the Lifshitz charge density (n_L). The red dashed line is obtained from a paralle-plate capacitore model in which $V_{TG} = \sigma d_{LAO}/\epsilon_{LAO}$, where $\epsilon_{LAo} = 24$ and $d_{LAO} = 5$ nm. Figure taken from [72][https://link.aps.org/doi/10.1103/PhysRevLett.118.106401].

[66, 75, 71, 72]. References [66, 75] applied a back-gate voltage and reported that n_1 smoothly decreases with gate voltage after the transition. On the other hand, Smink et al. [73] found that the slope of n_1 abruptly changes as shown in Fig. 4.1. To sum up, we conclude that both n_L, and the slope of n_1 depend on the experimental conditions.

We mentioned that all the experiments which observed the Lifshitz transition at STO-based interfaces used the two-band model as a way to analyze their Hall measurements [68, 66, 75, 71, 72]. However, there are some concerns with this model. First, the non-linear response of the Hall measurement suggests multiple types of carriers. Given the fact that the charges in the STO are spread over multiple layers of Ti atoms, each layer having different disorder depending on whether it is near

or far from the interface, it is not proper to assume that there are only two distinct mobilities. Secondly, Liang et al.[75] showed that it is difficult to obtain self-consistent fits of the two-band model to transport data. In particular, they found that the two-band ρ_{xx} deviates substantially from the experimental data, especially at high fields [75]. They concluded that it is difficult to develop a model that can describe the observed Hall measurements either quantitatively or qualitatively. The two-band model should be considered just as an approximation.

Joshua et al.[66] proposed a scenario to understand the Lifshitz transition that relates to the Ti 3d band structure at the STO interfaces. Due to symmetry breaking at the interface, the lowest energy xy band splits from the d_{xz} and d_{yz} bands. Therefore, below a critical carrier density, it is suggested that all charges reside in the xy band and only one type of carrier exists. Above the critical carrier density, as the gate voltage increases, the Fermi level is lifted across the bottom of the xz and yz bands. The two newly occupied bands are suggested to take up most of the added carriers[66].

This scenario has been investigated by Maniv et al., who used a three-band tight-binding model that includes spin-orbit coupling and on-site interactions [77]. The three-band model considers just one TiO_2 layer with three orbital types (d_{xy}, d_{xz}, and d_{yz}). Maniv et al.[77] used this model to explain the nonmontonic behaviour of the Hall coefficient in their experiments. They emphasized the role of the Hubbard-type interactions in redistributing the charges between bands as the gate voltage increases. Nandy et al. [78] used the same model to study how the strength of the electron-electron interaction (U) affects the Lifshitz transition. At $U = 0$, they reported a Lifshitz transition at $n_L = 0.18\mathrm{e}/\mathrm{a}^2 (1.2 \times 10^{14}\ \mathrm{cm}^2)$, and as U increases, they found

that n_L decreases. It should be emphasized, however, that the main features of the Lifshitz transition, especially the abrupt reduction of n_1 after the transition, are not reproduced by the model.

An important limitation of the three-band model is that it has only one layer. This means that the charge density per unit cell is an order of magnitude larger than the measured one for a given 2D charge density. As we show this makes the Hubbard-type interactions more important than they should be. Also, the model ignores the dielectric screening that has a significant effect on the STO band structure, as shown in Chapter 3.

In fact, it is not even clear that the three-band model scenario is supported by more realistic models [79, 31, 32, 33]. The goal of the reminder of this thesis is to develop a realistic model that explains the transition. In the next section, we investigate the doping-dependent band structure using our ideal-interface model, and compare it with experiments. We find that the model does not capture the important features of the transition. This motivates us to modify the model in Sec. 4.3.

4.2 Doping-Dependent Band Structure from the Ideal-Interface Model

In this section, we use the ideal-interface model, discussed in Chapter 3, to obtain the doping-dependent band structure in the very low-doping regime. First, we plot the potential energy and charge density as a function of layer index for doping $\sigma^s = 0.01, 0.02, 0.04\text{e/a}^2$ and at temperature 1 K. As seen in Fig. 4.2(a), the triangular quantum well is very shallow at $\sigma^s = 0.01\text{e/a}^2$, and the charge spreads into the STO. As the doping increases, the quantum well becomes deeper, which confines a greater fraction of the electrons to the interface creating 2D states along with the quasi-3D

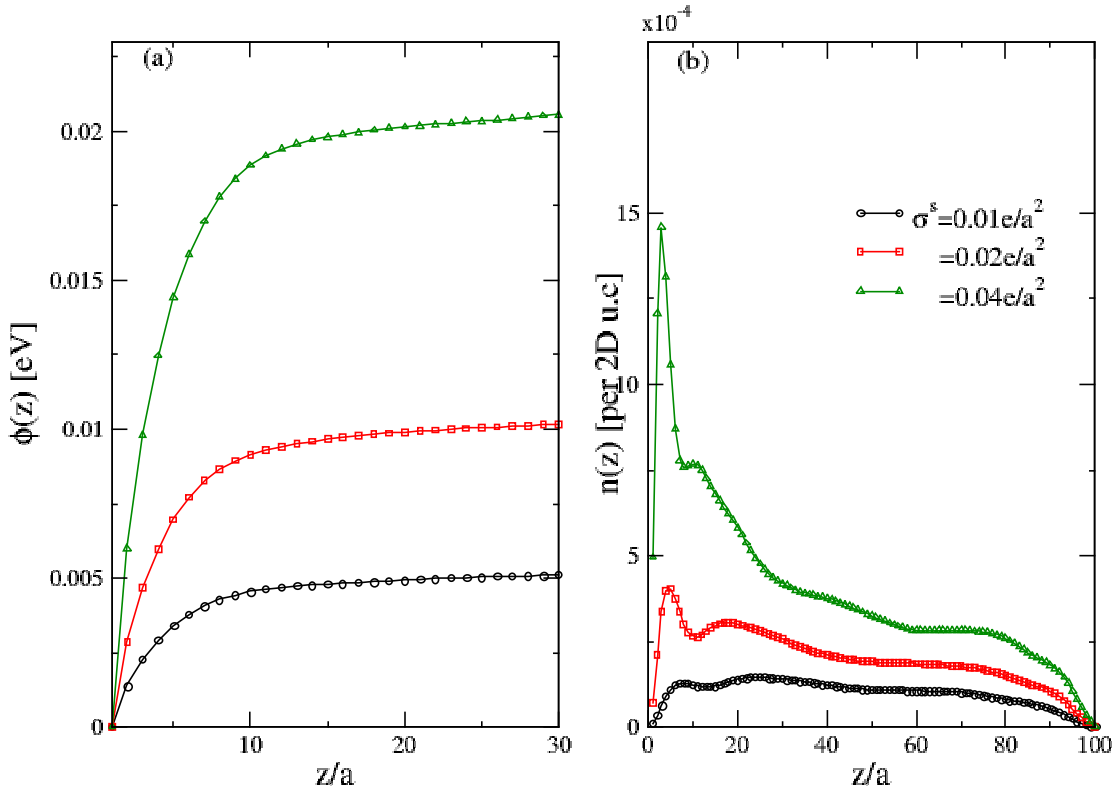

Figure 4.2: Potential energy (a) and charge density (b) per unit cell inside STO at low temperature (1 K) and dopings $\sigma^s = 0.01\text{e}/\text{a}^2$, $\sigma^s = 0.02\text{e}/\text{a}^2$, and $\sigma^s = 0.04\text{e}/\text{a}^2$. Results are for 100 layers and at T=1 K.

tails, Fig. 4.2(b).

Figure 4.3 shows the associated doping-dependent band structure for the ideal model along the k_x-direction. As the doping increases, the splitting between the $1xy$ band and the other bands gradually increases, which is consistent with the deeper quantum well shown in Fig. 4.2(b).

Our result for low doping, that multiple bands cross the Fermi level, does not

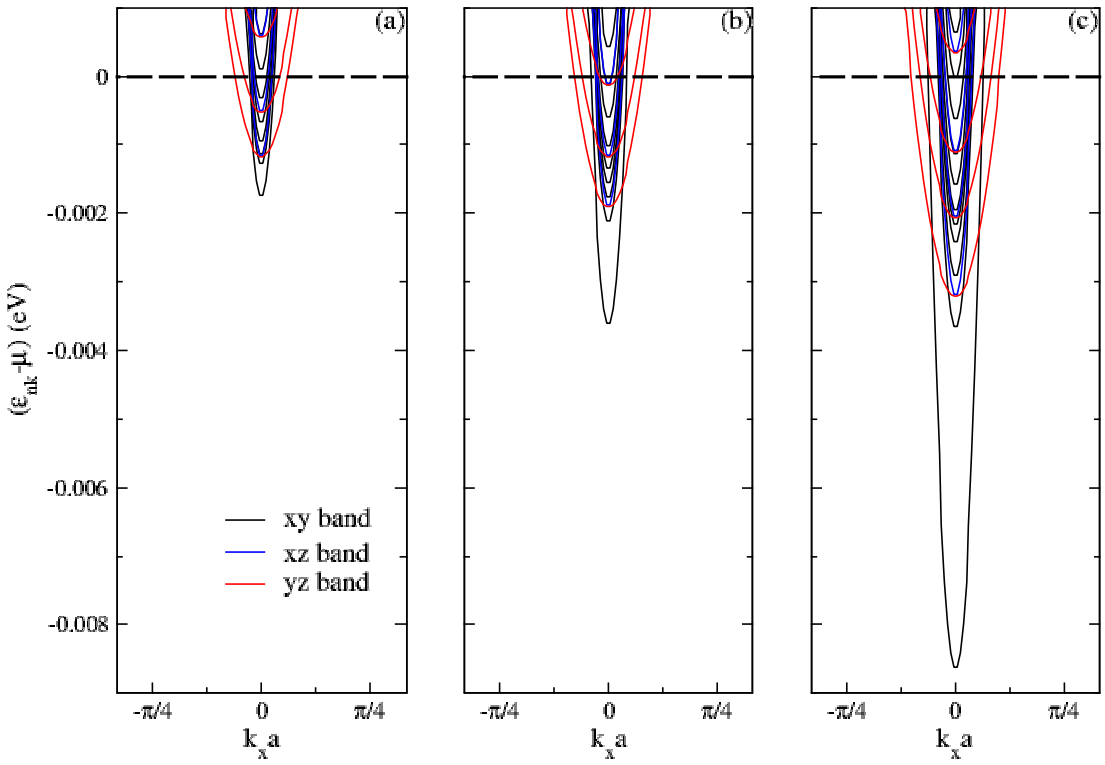

Figure 4.3: Doping-dependent band structure of a STO interface for (a) $\sigma^s = 0.01\text{e}/\text{a}^2$, (b) $\sigma^s = 0.02\text{e}/\text{a}^2$, and (c) $\sigma^s = 0.04\text{e}/\text{a}^2$. Results are for 100 layers, and at 1 K. Black lines are for the xy-character bands, blue for the xz-character bands, and red for the yz-character bands.

agree with experiments, where a single occupied band has been observed at low doping [66, 72]. Also, the ideal-interface model does not predict the sharp Lifshitz transition, discussed in the previous section, at which the electronic properties of the 2DEGs change.

Therefore, our proposal to obtain a single occupied band at low doping is to modify

the ideal-interface model to produce a deep quantum well that confines the electrons to one band. Then, as the doping increases, we expect a Lifshitz transition when higher energy bands become occupied. A deep quantum well is obtained here by a reduction in the permittivity at interface, namely a dielectric dead layer. In the next section, we adapt our model to accommodate a low permittivity near the interface.

4.3 Dielectric Dead-Layer Model

The presence of a dielectric dead layer at STO interfaces is well known. The high dielectric constant of STO makes it a good candidate for nanoscale capacitors, but experimentally, the capacitance of thin STO films is found to be much smaller than expected from bulk properties [80, 81, 82]. The reason for this is the existence of a low-permittivity layer at the STO interfaces, which is known as a "dead layer". The origin of the dead layer is still a controversial issue. Some results suggest that dead layers could arise from strains and defects [82], while other work [83] has reported that the reduction in the permittivity is an intrinsic property, i.e that the induced depolarizing field [the depolarizing field is defined in Eq. (2.22)] hardens the soft mode. The origin of the dead layer in nanoscale STO capacitors is beyond the scope this thesis. Here, we simply assume there is a dead layer, modeled by a reduction of the dielectric susceptibility, and study its effect on the electronic structure.

In order to include the dead layer, we need to modify our dielectric model. The dielectric susceptibility (Appendix B) is

$$\chi(T,E) = \frac{Q^2}{\epsilon_0 a^3}\frac{1}{D_{\mathbf{q}=0} + 3\gamma u^2}, \tag{4.4}$$

where u is obtained from Eq. (2.25), and $D_{\mathbf{q}=0} = \sum_{j_z} D_{i_z j_z}$.

In the weak-field limit, where u is small, Eq. (4.4) shows that the susceptibility is inversely proportional to the matrix of force elements [$\chi \propto (D_{\mathbf{q}=0})^{-1}$]. Therefore, increasing the values of the diagonal elements, $D_{i_z i_z}$, lowers the dielectric susceptibility. To include a dead layer, we therefore add a correction term

$$\tilde{D}_{i_z i_z} = D_{i_z i_z} + \delta D e^{-(z_i/d)^4}, \tag{4.5}$$

with $\delta D > 0$, $z_i = i_z a$, and d the thickness of the dead layer. The stretched exponential function, $e^{-(z_i/d)^4}$, is a convenient way to smoothly connect the dielectric function to its bulk value. We plot the diagonal elements $D_{i_z i_z}$ of the force constant matrix versus distance from the interface in Fig. 4.4 for $\delta D = 180$ kgs^{-2} and $d = 4a$. As shown, $D_{i_z i_z}$ falls to its bulk value within 6 unit cells of the interface.

With this modification, we calculate the normal coordinate u_{i_z} [see Eq. (2.25)] and the electron density self-consistently, following the same procedures as in Chapter 2.

In Fig. 4.5, we plot the potential energy [$\phi(z)$], and the electron density [$n(z)$] as functions of distance from the interface at T= 1 K, and $\sigma^s = 0.01$e/a^2 for several δD values. At $\delta D = 0$, the triangular quantum well is very shallow, while it becomes deeper when δD increases as shown in Fig. 4.5.(a). This behavior is caused by the reduction in the dielectric screening at the interface. This dead layer causes electrons to move towards the interface, and when δD is big, most of the electrons are confined to the interface, as shown in Fig. 4.5.(b).

The evolution of the band structure with different δD values is shown in Fig. 4.6. When $\delta D = 0$, we have the same results as in Fig. 4.3.(a) for $\sigma^s = 0.01$ e/a^2, namely a 3D continuum of states due to the strong dielectric screening. As δD increases, the splitting between the $1xy$-band and the continuum increases. At extremely large δD,

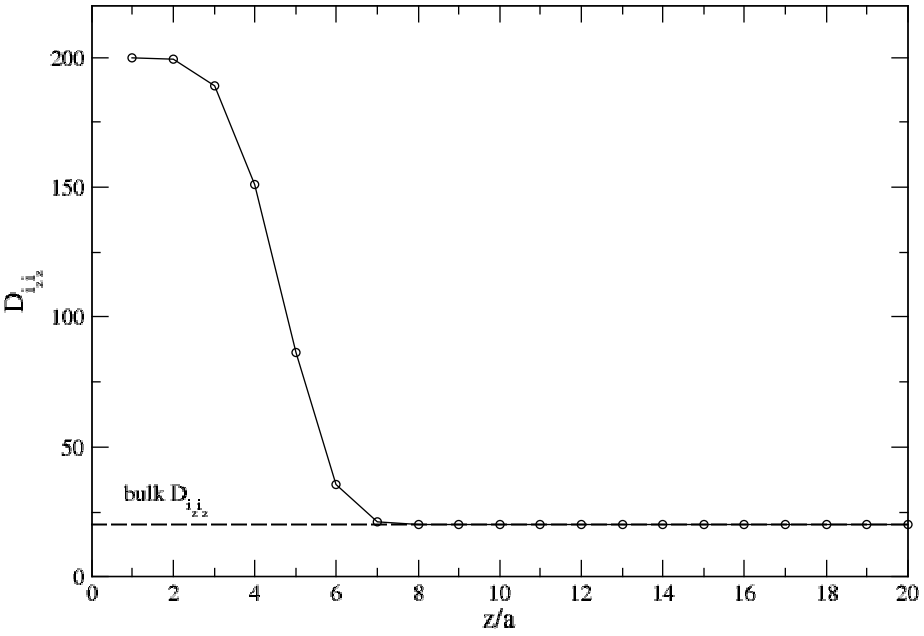

Figure 4.4: The diagonal elements $D_{i_z i_z}$ of the force constant matrix for $\delta D = 180$ kgs^{-2}, and $d = 4a$.

the $1xy$ band becomes the only band crossing the Fermi level [Fig. 4.6.(d)].

In summary, this simple model for the dielectric dead layer changes the shape of the confining potential. 2D states develop as δD increases, and eventually only one occupied band is obtained at large δD. This is consistent with Hall measurements[66, 72] that reported a single occupied band at low doping.

4.4 Relevance of the Dead Layer to the Lifshitz Transition

The consistency of the band structure for large δD at low doping with experiments induces us to explore the doping-dependent band structure. The band structure at

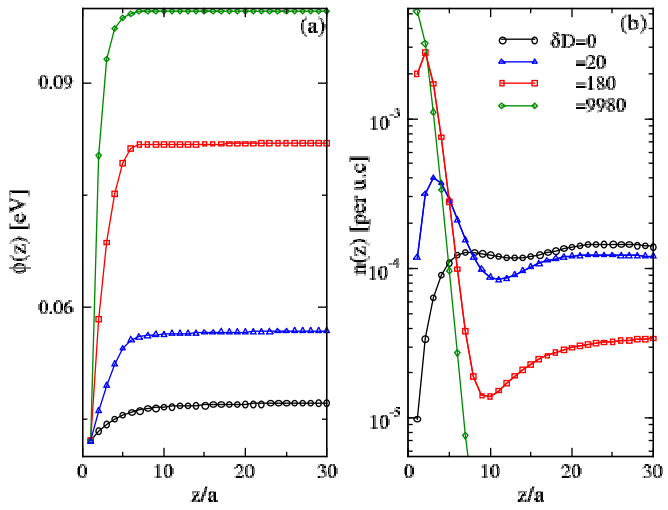

Figure 4.5: The potential energy (a), and the charge density (b) profiles in STO with a dead layer for 0.01 e/a^2 doping, at T= 1 K and for 100 layers. Results are for δD=0 to 9980 kgs^{-2}.

fixed δD = 9980 kgs^{-2} for various doping is shown in Fig. 4.7. Generally speaking, as the doping grows, we see a crossover between one and multiple occupied bands. At low doping, the $1xy$ band is the only band crossing the Fermi level [Fig. 4.7.(a)]. When we increase the doping, other bands cross the Fermi level in a series of Lifshitz transitions. The first transition happens when the $2xy$ band crosses the Fermi level at σ^s =0.03 e/a^2, as shown in Fig. 4.7.(b). The second transition takes place when the $1xz$ and $1yz$ bands separate from the continuum and cross the Fermi level at σ^s =0.07 e/a^2 [Fig. 4.7.(d)]. An important feature of Fig. 4.7 is that the $1xy$ band keeps moving to lower energies as the doping increases.

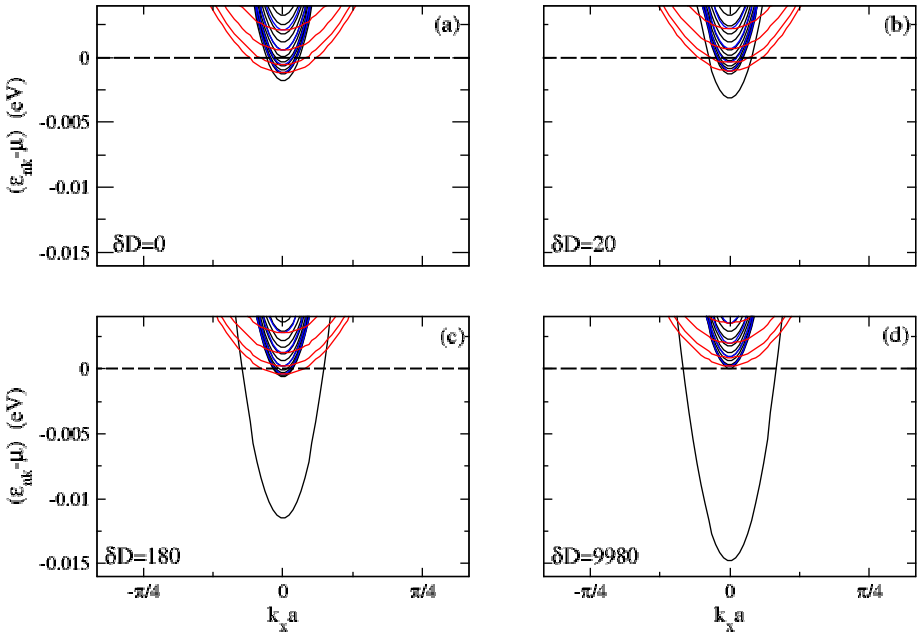

Figure 4.6: Band structure including dead layer for $\sigma^s = 0.01\text{e/a}^2$, at T= 1 K and for 100 layers. (a)-(d) for δD=0 to 9980 kgs^{-2}

To compare to Fig. 4.1, we calculate the filling of the lowest four bands as a function of doping, as shown in Fig. 4.8. At low doping, the filling of the $1xy$ band coincides with the total charge σ^s (dashed line) which indicates that nearly all electrons reside in the $1xy$ band. As the doping increases ($\sigma^s \geq 0.03$ e/a^2), the $1xy$ band filling shifts away from the total charge as the other bands become occupied. However, there are important differences between Fig. 4.1 and Fig. 4.8. First, the slope of the $1xy$ band filling in Fig. 4.8 changes gradually. Second, there are multiple Lifshitz transitions (n_{L1} and n_{L2}) in Fig. 4.8 but not in Fig. 4.1.

This leads us to look for another ingredient to add to our dielectric dead-layer

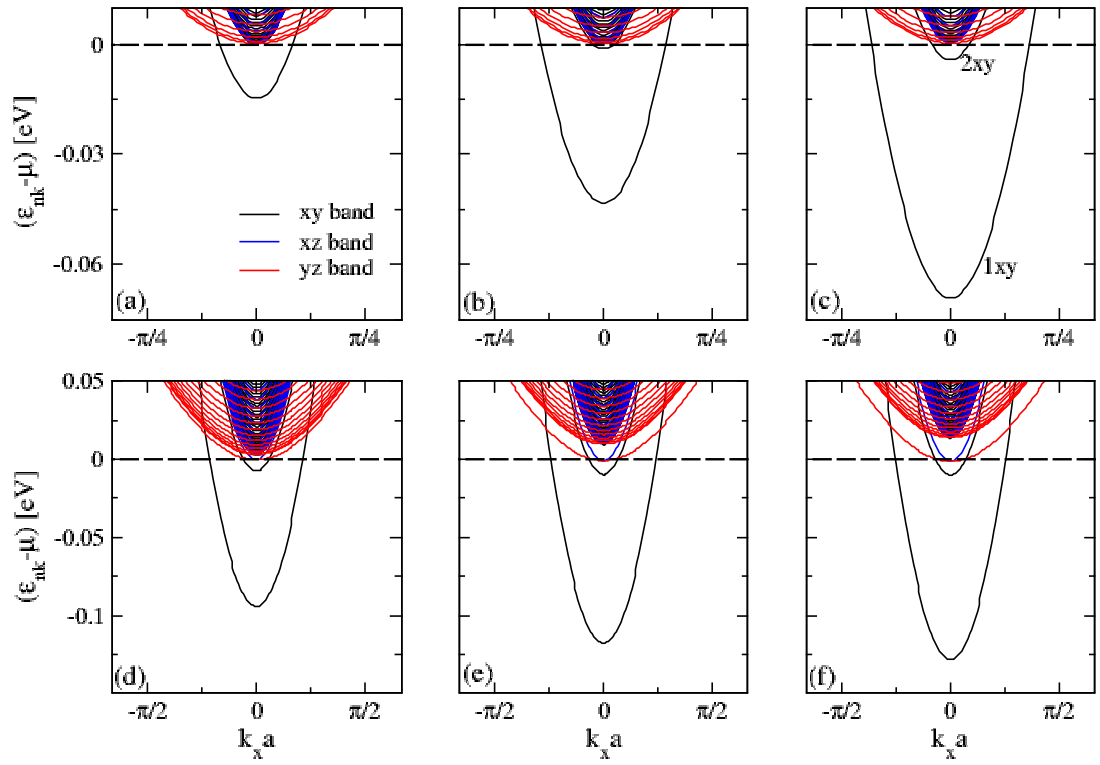

Figure 4.7: Band structure as a function of doping for $\delta D = 9980$ kgs^{-2} and at T=1 K. Results are for $\sigma^s = 0.01$ (a), 0.03 (b), 0.05 (c), 0.07 (d), 0.09 (e), and 0.1 e/a^2 (f).

model. Motivated by previous theoretical work, we add short-range Coulomb interactions to the model [77].

4.4.1 Short Range Electron-Electron Interactions

We consider short-range interactions between electrons on the same Ti atom through a Hubbard term, H_{hub}. The detailed derivation of the Hubbard term in the mean-field

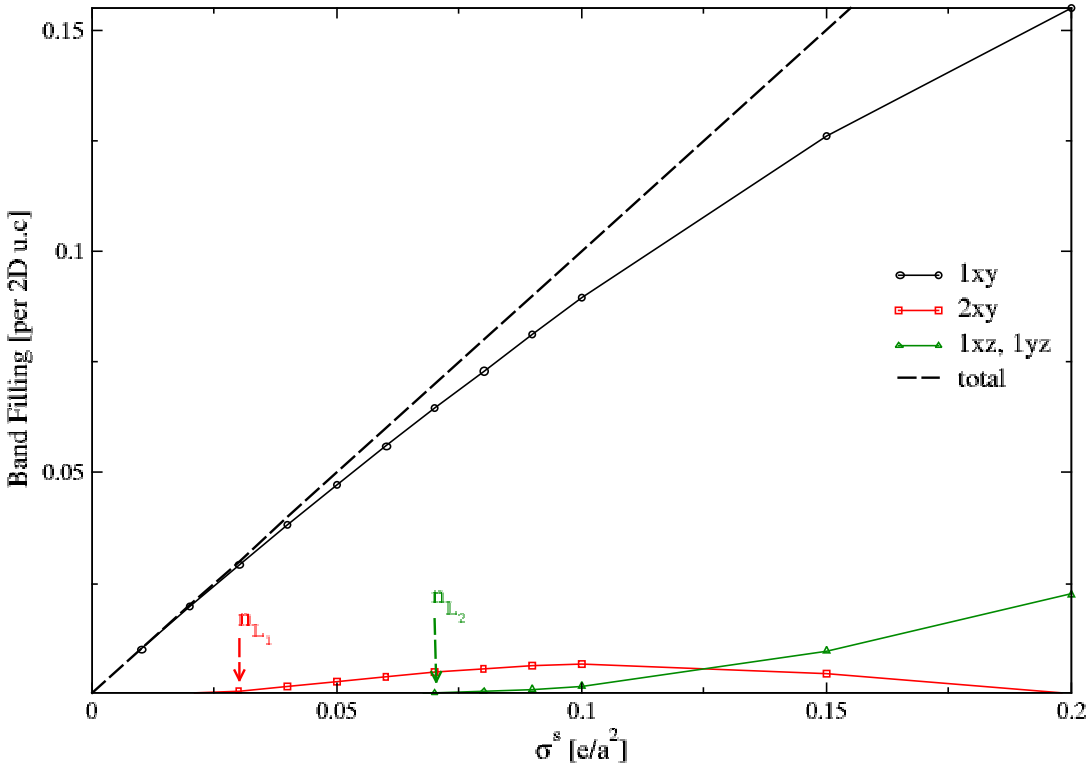

Figure 4.8: The band filling as a function of doping for $\delta D = 9980$ kgs^{-2} and at T=1 K.

approximation is given in Appendix E. The final mean-field expression is

$$\hat{H}^{MF}_{hub} = \sum_{i_z\alpha\sigma} U_0 n_{i_z\alpha\sigma}\hat{n}_{i_z\alpha-\sigma} + \sum_{i_z\sigma}\sum_{\beta\neq\alpha}(2U-J)n_{i_z\beta\sigma}\hat{n}_{i_z\alpha-\sigma}, \tag{4.6}$$

where i_z is the layer index, $\sigma =\uparrow$ or $\downarrow$, α and β label the orbital types. $\hat{n}_{i_z\alpha\sigma}$ is the occupation number operator, and $n_{i_z\alpha\sigma}$ represents the average electron occupation number [Eq. (2.15)]. U_0 represents the intra-orbital interaction, U is the inter-orbital

interaction, and J is the exchange interaction. We assume here that $n_{i_z\alpha\uparrow} = n_{i_z\alpha\downarrow}$.

The d-orbital symmetry imposes [84] a relationship between the interactions: $U_0 = U + 2J$. Considering this constraint, along with the observation that $n_{i_zxy\sigma} \gg n_{i_zxz\sigma}, n_{i_zxz\sigma}$ as shown in Fig.3.4, we can show that there are two distinct behaviours depending on how J is chosen. First, we need to write the mean-field Hubbard terms explicitly for each orbital type

$$(\hat{H}^{MF}_{hub})_{xy} = \sum_{i_z\sigma} U_0 n_{i_zxy\sigma}\hat{n}_{i_zxy-\sigma} + \sum_{i_z\sigma}(2U_0 - 5J)[n_{i_zxz\sigma} + n_{i_zyz\sigma}]\hat{n}_{i_zxy-\sigma}, \tag{4.7}$$

$$(\hat{H}^{MF}_{hub})_{xz} = \sum_{i_z\sigma} U_0 n_{i_zxz\sigma}\hat{n}_{i_zxz-\sigma} + \sum_{i_z\sigma}(2U_0 - 5J)[n_{i_zxy\sigma} + n_{i_zyz\sigma}]\hat{n}_{i_zxz-\sigma}. \tag{4.8}$$

Since $n_{i_zxy\sigma} \gg n_{i_zxz\sigma}$ in the first few layers,

$$(\hat{H}^{MF}_{hub})_{xy} \approx \sum_{i_z\sigma} U_0 n_{i_zxy\sigma}\hat{n}_{i_zxy-\sigma}, \tag{4.9}$$

$$(\hat{H}^{MF}_{hub})_{xz} \approx \sum_{i_z\sigma}(2U_0 - 5J)[n_{i_zxy\sigma} + n_{i_zyz\sigma}]\hat{n}_{i_zxz-\sigma}. \tag{4.10}$$

Therefore, we have one behaviour where the Hubbard term shifts electrons towards the d_{xy} orbitals if $(2U_0 - 5J) > U_0$, i.e $J < \frac{U_0}{5}$, and a second behaviour where electrons prefer to occupy d_{xz} and d_{yz} orbitals if $J > \frac{U_0}{5}$.

We plot the band filling as function of doping at several J values in Fig. 4.9. At J=0 eV, it is clear from Eqs. (4.9) and (4.10) that the $(\hat{H}^{MF}_{hub})_{xz}$ term is greater than

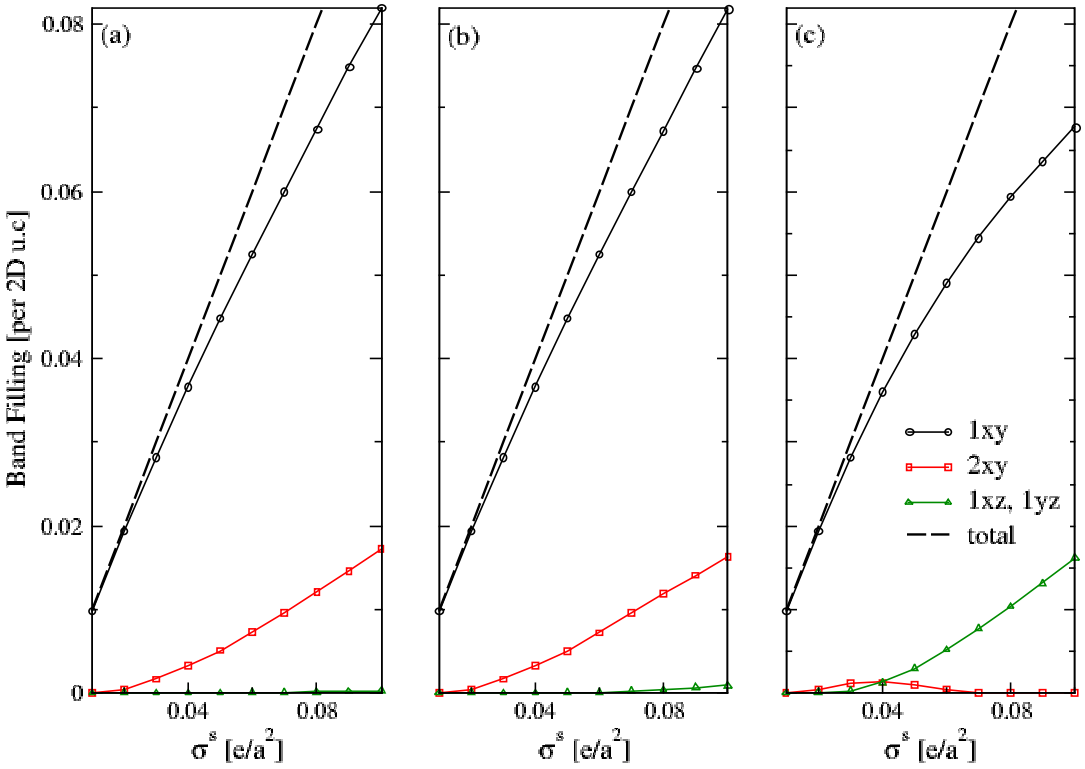

Figure 4.9: The band filling as a function of doping at different values of J, (a) J=0 eV, and U=4 eV, (b) J=0.4 eV, and U=3.2 eV , and (c) J=1.6 eV and U=0.8 eV. Results are for 100 layers, δD = 9980 kgs^{-2}, U$_0$=4 eV, and at T=1 K.

$(\hat{H}^{MF}_{hub})_{xy}$ by a factor of two, which means that the electrons prefer to occupy the xy bands as shown in Fig. 4.9.(a). At J=0.4 eV, the $(\hat{H}^{MF}_{hub})_{xz}$ term is still greater than $(\hat{H}^{MF}_{hub})_{xy}$, and we have nearly the same band filling [see Fig. 4.9.(b)]. At a unphysically large value of J=1.6 eV, the $(H^{MF}_{hub})_{xz}$ term equals zero, and we see that the xz and yz bands start to be occupied, Fig. 4.9.(c). Therefore, the competition

between the two Hubbard terms, $(\hat{H}^{MF}_{hub})_{xy}$ and $(\hat{H}^{MF}_{hub})_{xz}$, controls the filling of the different bands.

Figure 4.10 compares the band filling as a function of doping with and without the interaction term $\hat{H}^{MF}_{hub}$. At J=0.8 eV, the probability of occupying the xy, and xz, yz bands is equal. As shown, we have the same qualitative behaviour as without the interaction term: we see only a small change in the slope of the $1xy$ band filling after the Lifshitz transition, which is not consistent with experiments. This is so because at low electron densities, the effect of the Hubbard interactions is small compared with other terms in the Hamiltonian. To sum up, these results indicate that including short-range Coulomb interactions only weakly affects the band structure.

4.5 Summary

In this chapter, we attempted to explain the observed Lifshitz transition with a realistic model interface. The ideal-interface model failed to predict the transition, and it was imperative to modify the model to observe this transition. We introduced a dielectric dead layer in which we assumed a low premittivity at the interface. We found a single occupied band at low doping and predicted a Lifshitz transition at a similar n_L to what is found experimentally [75, 71, 72]. However, we found that the $1xy$-band filling always grows with the doping, even when correlations are considered, which is not consistent with the reported results [see Fig. 4.1]. We conclude that the dielectric dead-layer model does not give a complete explanation for the Lifshitz transition.

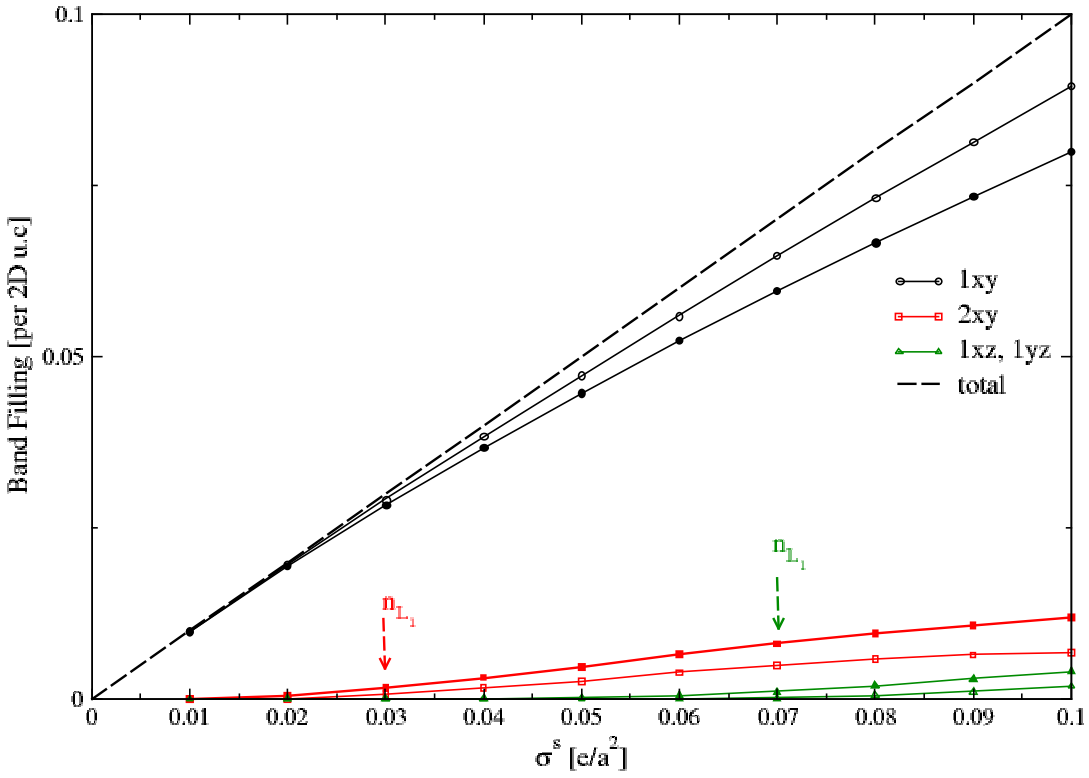

Figure 4.10: The band filling as a function of doping with and without Hubbard term. Results for $\delta D = 9980$ kgs^{-2}, $U_0 = 4eV$, $J = 0.8eV$, and $U = 2.4eV$.

Chapter 5

Flexoelectric Origin of the Lifshitz Transition in LAO/STO Interfaces

This chapter explores the effects of strain and strain gradients on the STO band structure. First, we modify the Landau-Devonshire energy to accommodate the strain effects. Then, we study the doping-dependent electronic properties, and compare the obtained results with experiments.

In the previous chapters, we started with an ideal interface, where the interface has the same dielectric properties as the bulk, and we obtained the temperature-dependent band structure. We found that the doping-dependent band structure is not consistent with experiments at low doping. We then modified our model to include a dielectric dead-layer. This case was successful in obtaining the band structure at low doping and predicted a sequence of Lifshitz transitions, but did not predict the reported abrupt change in the filling of the lowest band at n_L. This leads us to consider other models for the Lifshitz transition.

As will be discussed in the following sections, many experiments reported strain in the STO thin films, and showed that strain changes the dielectric properties of the

films. This motivates us to investigate the strain effects on the band structure.

5.1 Strain

Strain commonly happens at interfaces due to the lattice mismatch between a thin film and substrate during growth of the film. This results in a strained thin film. The strain may be used to engineer interfaces. For instance, strain controls the mobility in semiconductors by increasing the subband splitting and hence decreasing the inter-subband phonon scattering rate [85]. For thin films of perovskite materials such as $SrRuO_3$[86], it was found that biaxial strain (tensile and compressive) modifies and controls the RuO_6 octahedral rotations, which consequently changes the Ru-O-Ru angle. This affects the orbital overlap and modifies transport properties of $SrRuO_3$; the conductivity in $SrRuO_3$ thin films under tensile stress is much lower than films under compressive stress. As another example, it is found that strain can enhance the transition temperature in thin films of ferroelectric materials such as $BaTiO_3$ [87]. For these reasons, strain is considered a useful tool for the manipulation of the electronic properties of thin films.

Strain as well is key in controlling ferroelectricity in STO. Strained STO can be obtained by applying mechanical stress to bulk STO, or by epitaxially growing STO on substrates that have a small lattice mismatch with it. It was observed that by applying uniaxial mechanical stress to bulk STO, ferroelectric polarization can be induced along the z-direction at low temperature [88], while by growing STO epitaxially on $DyScO_3$ substrates, Haneni et. al [89] reported ferroelectricity in STO thin films at room temperature.

Indeed, strain does not only control ferrelectricity in STO thin films, but it also

has a dramatic effect on the 2DEGs at STO interfaces. Bark et al. [90] grew STO on substrates with different lattice mismatches, and then deposited LAO thin films to create LAO/STO interfaces. This produced biaxially strained STO. The results revealed that tensile-strained STO has no conducting 2DEG, i.e. it is an insulating interface, while compressively-strained STO has a 2DEG with total charge density less than the unstrained interface. The tensile strain effect on 2DEGs was later confirmed by Huang et. al [91]; however, they found that the charge density increases and mobility decreases under compressive strain. In addition, they reported that the charge mobility is more sensitive to strain than the charge density. Overall, the results of these studies show that the strain can tailor the 2DEGs at STO interfaces.

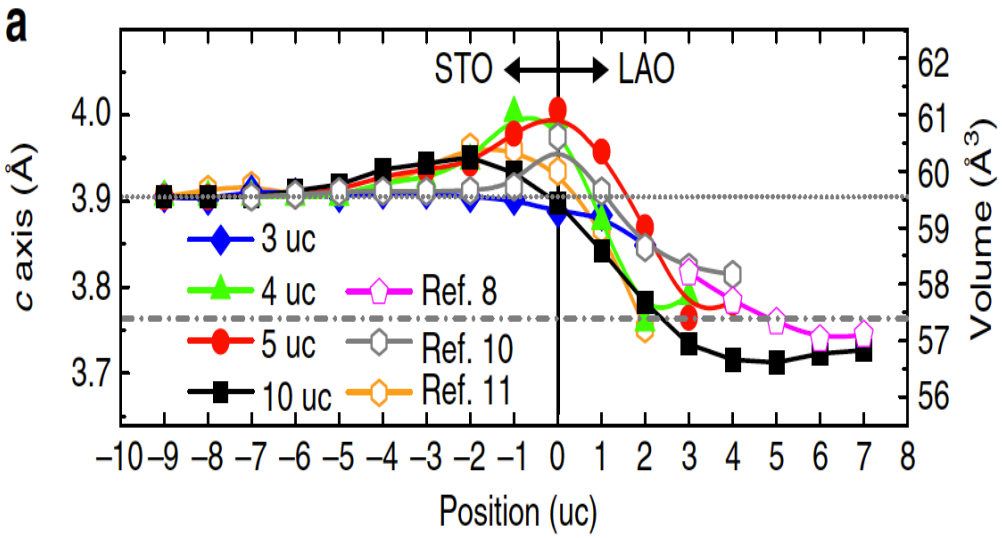

Figure 5.1: The c-axis lattice constant and unit cell volume changes in LAO/STO. The SXRD results are for of heterostructures with various LAO thicknesses. Grey dotted (dotted dashed) line, lattice constant of bulk STO (LAO). The different curves show the results for several LAO thicknesses. Figure taken from [92].

The strain in the preceding discussion was uniform throughout the STO thin films.

However, even in nominally unstrained films, strain is observed in the first few layers near to the interface [93, 92]. Figure 5.1 shows an example of this interfacial strain. The c-axis variations of the LAO/STO lattice constants are observed by using surface X-ray diffraction (SXRD). As shown in Fig. 5.1, the c-axis on the STO side elongates in the first five layers and then relaxes back to its bulk value of $c_0 = 3.905\ \mathring{A}$. For example, in the case of 5 unit cells of LAO (red curve), the (tensile) strain in the first layer of STO is about $\Delta c_0/c_0 = +0.02$ as shown in Fig. 5.1.

The observed interfacial strain in Fig. 5.1 motivates us to consider strain effects. Generally speaking, the strain affects the polarization. As will be seen in the next sections, the strain couples to the polarization in the free energy equation. In addition, the c-axis strain gradients at the interface linearly couple with the polarization through a flexoelectric term. These two terms change the dielectric function at the interface.

In the following sections, we extend the ideal interface model to accommodate the strain effects. First, we include the strain-polarization coupling term, and then investigate its effect on the band structure. Second, we add the coupling between the strain gradient and the polarization.

5.1.1 Coupling to Strain: Electrostriction

To understand how the strain affects the dielectric properties, we need to include the contribution of the strain to the free energy equation. First, the strain (η) is defined by how the displacement of an atom $\vec{\zeta}(\vec{R})$ from its unstrained position $\vec{R}$ varies

$$\eta_{ij} = \frac{1}{2}\left(\frac{\partial \zeta_i}{\partial R_j} + \frac{\partial \zeta_j}{\partial R_i}\right), \tag{5.1}$$

where i, j correspond to x, y, z-directions. The strain is a second rank tensor, its diagonal elements are referred to as normal and the off-diagonal elements as shear. In Voigt notation, the subscripts of η can be simplified as $\eta_{xx} \rightarrow \eta_1$, $\eta_{yy} \rightarrow \eta_2$, $\eta_{zz} \rightarrow \eta_3$, $\eta_{yz} \rightarrow \eta_4$, $\eta_{xz} \rightarrow \eta_5$, and $\eta_{xy} \rightarrow \eta_6$ [46, p.445].

Neglecting strain gradients for the moment, the general full free energy in terms of polarization and strain [88] is

$$\begin{aligned} U(P,\eta) &= \alpha_1(P_1^2+P_2^2+P_3^2)+\alpha_{11}(P_1^4+P_2^4+P_3^4)+\alpha_{12}(P_1^2P_2^2+P_1^2P_3^2+P_2^2P_3^2) \\ &+ \frac{1}{2}c_{11}(\eta_1^2+\eta_2^2+\eta_3^2)+c_{12}(\eta_1\eta_2+\eta_1\eta_3+\eta_2\eta_3)+\frac{1}{2}c_{44}(\eta_4^2+\eta_5^2+\eta_6^2) \\ &- g_{11}(\eta_1P_1^2+\eta_2P_2^2+\eta_3P_3^2)-g_{12}[\eta_1(P_2^2+P_3^2)+\eta_2(P_1^2+P_3^2)+\eta_3(P_1^2+P_2^2)] \\ &- g_{44}(\eta_4P_2P_3+\eta_5P_1P_3+\eta_6P_1P_2), \end{aligned} \tag{5.2}$$

where $\alpha_1 = \frac{1}{2}\frac{a^3}{Q^2}\sum_j D_{ij}$ is the dielectric stiffness, α_{11}, α_{12} are the higher-order stiffness coefficients at a constant strain, c_{nl} are the elastic stiffness at constant polarization, and g_{nl} are the electrostrictive constants that describe the coupling between the polarization and the strain. Equation (5.2) applies to a cubic system where $g_{11} = g_{22} = g_{33}$, $g_{12} = g_{13} = g_{23}$ and $g_{44} = g_{55} = g_{66}$. Note also, $\alpha_1 = \alpha_2 = \alpha_3$, $\alpha_{11} = \alpha_{22} = \alpha_{33}$, and $\alpha_{12} = \alpha_{13} = \alpha_{23}$. In the Voigt notation, g_{11} means that both the strain and the polarization are along the same axis, while g_{12} represents the coupling between strain and polarization along different axes.

The strain in our case is not an order parameter but is imposed to match experiments. Thus, the free energy is only a function of polarization,

$$\begin{aligned} U(P) &= \alpha_1(P_1^2+P_2^2+P_3^2)+\alpha_{11}(P_1^4+P_2^4+P_3^4)+\alpha_{12}(P_1^2P_2^2+P_1^2P_3^2+P_2^2P_3^2) \\ &- g_{11}(\eta_1P_1^2+\eta_2P_2^2+\eta_3P_3^2)-g_{12}[\eta_1(P_2^2+P_3^2)+\eta_2(P_1^2+P_3^2)+\eta_3(P_1^2+P_2^2)] \\ &- g_{44}(\eta_4P_2P_3+\eta_5P_1P_3+\eta_6P_1P_2). \end{aligned} \tag{5.3}$$

For the interface, the polarization points in the z-direction, i.e. $P_1 = P_2 = 0$. This gives

$$U(P) = \alpha_1P_3^2+\alpha_{11}P_3^4-g_{11}\eta_3P_3^2-g_{12}[\eta_1P_3^2+\eta_2P_3^2]. \tag{5.4}$$

In case of the bulk STO, the reported value for $g_{12} = -1\times10^9$ JmC^{-2}, which is much smaller that $g_{11} = 1.33\times10^{10}$ JmC^{-2}, i.e $|g_{12}| \ll g_{11}$. This yields

$$U(P) \cong [\alpha_1 - g_{11}\eta_3]P_3^2+\alpha_{11}P_3^4. \tag{5.5}$$

For STO interfaces, neither the polarization nor the strain is homogeneous through the STO [92]. This leads us to extend Eq. (5.5) to include a layer dependence

$$\frac{U}{N_{2D}} = \frac{1}{2}\sum_{i_zj_z} u_{i_z}[D_{i_zj_z}-2\tilde{g}_{11}\delta_{i_zj_z}\eta_{i_z}]u_{j_z} - Q\sum_{i_z}E_{i_z}u_{i_z}+\frac{\gamma}{4}\sum_{i_z}u_{i_z}^4, \tag{5.6}$$

with $\tilde{g}_{11} = g_{11}\frac{Q^2}{a^3}$, and where $\delta_{i_zj_z}$ is the Kronecker delta function.

As seen in Eq. (5.6), the electrostrictive term, $-2\tilde{g}_{11}\delta_{i_zj_z}\eta_{i_z}$, modifies $D_{i_zj_z}$. From Eq. (4.4), the susceptibility is inversely proportional to the matrix of force elements $D_{i_zj_z}$ in the low electric field limit. Thus, since the experimental value of g_{11} is positive [88] a positive (tensile) strain increases the susceptibility.

In order to model the strain profile shown in Fig. 5.1, we choose an empirical expression for the strain η_{i_z}

$$\eta_{i_z} = \eta_0 \exp[-(z_i/d)^4], \tag{5.7}$$

where $\eta_0 = \Delta c_0/c_0$ is the strain at the top STO layer, $z_i = (i_z - 1)a$, and $d = 4a$ the thickness of the strained layer at the interface. This form qualitatively captures the shape of the strain profile. Thus, the modified $\tilde{D}_{ij}$ elements are

$$\tilde{D}_{i_z j_z} = D_{i_z j_z} - 2\tilde{g}_{11}\delta_{i_z j_z}\eta_0 \exp[-(z_i/d)^4]. \tag{5.8}$$

5.1.2 Results

Figure 5.2 shows a comparison between the potential energy, charge density profile, and band structure for the case of an ideal interface ($g_{11} = 0$) and for the case where electrostrictive coupling is included ($g_{11} = 1.33 \times 10^{10}$ Jm/C^2 [88]). As seen, electrostrictive coupling reduces the confining potential relative to the ideal interface, which therefore deconfines the electron gas [Fig. 5.2(a) and (b)]. The band structure does not change much with the strain coupling; it forms a quasi-3D continuum at $\sigma^s = 0.01$ e/a^2, as in the ideal-interface case [Fig. 5.2(c) and (d)] that is not consistent with experiments. We repeated our calculations at $g_{11} = 0.8 \times 10^{10}$ and 2.0×10^{10} Jm/C^2 values and different strain sizes η_0, and found similar qualitative results as in Fig. 5.2(c) and (d).

Our conclusion is that the electrostrictive coupling term by itself has a very small effect on the interface electronic properties compared with the ideal-interface case. Next, we consider coupling to the strain gradient.

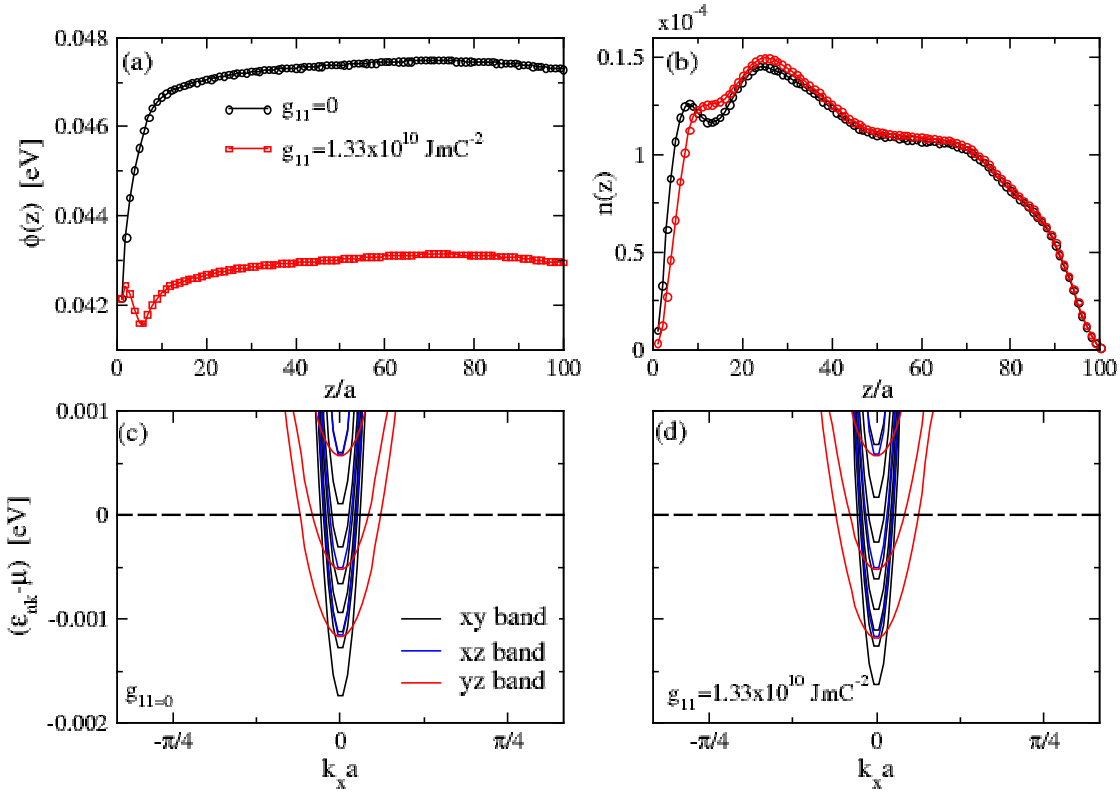

Figure 5.2: Effect of electrostrictive coupling on electronic structure. (a) and (b) show the potential energy $\phi(z)$, and charge density profiles for $g_{11} = 0$ (ideal interface) and $g_{11} = 1.33 \times 10^{10}$ Jm/C^2. (c) and (d) show the corresponding band structures. The results are for $\sigma^s = 0.01$ e/a^2, 100 layers and at T=1 K.

5.2 Coupling to Stain Gradients: Flexoelectricity

In addition to an interfacial strain, Fig. 5.1 shows that STO interfaces have large strain gradients. The strain gradient contributes to the free energy equation through

a flexoelectric term $-\tilde{f}_{11}\sum_{i_z}\frac{\partial\eta_{i_z}}{\partial z_i}u_{i_z}$. Here, $\tilde{f}_{11} = f_{11}\frac{Q}{a}$, where f_{11} is the flexoelectric coefficient that represents coupling between the strain gradients ($\frac{\partial\eta_{i_z}}{\partial z_i}$) and the polarization. Flexoelectricity is a property of materials whereby they polarize when subject to nonuniform strain. It makes these materials a good choice for electromechanical sensors and actuators [94]. Also, strain gradients can mimic an electric field, and can switch the spontaneous polarization of a ferroelectric material [94].

The full Landau-Devonshire energy including flexoelectricitiy is

$$\frac{U}{N_{2D}} = \frac{1}{2}\sum_{i_z j_z} u_{i_z}[D_{i_z j_z} - 2\tilde{g}_{11}\delta_{i_z j_z}\eta_{i_z}]u_{j_z} - \sum_{i_z}\Big[QE_{i_z} + \tilde{f}_{11}\frac{\partial\eta_{i_z}}{\partial z_i}\Big]u_{i_z} + \frac{\gamma}{4}\sum_{i_z} u_{i_z}^4 \quad (5.9)$$

where the strain gradient $\frac{\partial\eta_{i_z}}{\partial z_i}$ is calculated using Eq. (5.7). There is no consensus about the reported value of the flexoelectric coefficient of STO. Most DFT studies predict a wide range for this value of 1-10 V [94]. Here, we perform our calculations using f_{11} values in range of 1-3 V. We repeated our calculations for values bigger than 3 V, and found that the results do not change qualitatively.

The polarization is obtained by minimizing Eq. (5.9) with respect to u_{l_z},

$$\sum_{j_z}[D_{l_z j_z} - 2\tilde{g}_{11}\delta_{l_z j_z}\eta_{l_z}]u_{j_z} + \gamma u_{l_z}^3 = QE_{l_z} + \tilde{f}_{11}\frac{\partial\eta_{l_z}}{\partial z_i}|_{z_i=z_l}. \quad (5.10)$$

At low doping, the electric field is small and Eq. 5.10 tells us that, for negative $\frac{\partial\eta_{i_z}}{\partial z}$, and $f_{11} > 0$, one may have polarization that points opposite to the electric field. As the electric field increases, by increasing the doping, the polarization switches its direction and points in the same direction as the electric field.

We perform the same self-consistent calculations that were discussed in Chapter 2 to obtain the band structure. However, we note that in this case our code is not

stable and it is hard to obtain convergence. This is because the flexoelectric term switches the polarization direction from one iteration to the next. To stabilize the code, we changed how the polarization was calculated, as discussed in Appendix F.

5.2.1 Results

Figure 5.3 shows the band structure at low and intermediate doping for $f_{11} = 2$ V, and $\eta_0 = 0.02$. At $\sigma^s = 0.01$ e/a^2, there is only one band crossing the Fermi level, consistent with experiments. At $\sigma^s = 0.06$ e/a^2, a transition to multiple occupied bands takes place, which is an indication of a Lifshitz transition. These results qualitatively agree with both the dielectric dead layer case [Fig. 4.7], and with experiments [72]. In addition, we see a second Lifshitz transition when the 3D tail states cross the Fermi level as shown in Fig. 5.3.(b).

In order to compare with Fig. 4.1, we plot the filling of lowest four energy bands $(1xy, 2xy, 1xz/1yz)$ as a function of doping Fig. 5.4. This figure has two main features. First, there are two Lifshitz transitions: one when the $2xy$ and $1xz/yz$ bands begin to be occupied at $n_{L1} \approx 0.015$ e/a^2, and the other when the 3D tail bands begin to be occupied at $n_{L2} \approx 0.025$ e/a^2. The second main feature is that the slope of the $1xy$ band filling changes with doping: at low doping it is constant, then it becomes nearly zero after the transition, and finally it increases with doping. This abrupt change in the $1xy$ slope is consistent with the reported results in [66, 75, 72]. Indeed, Fig 5.4 captures the two main features reported by Smink et al. [72]: one is that there is a Liftshitz transition at critical charge density; second is that there is an abrupt reduction in n_1 after the transition [see Fig. 4.1]. To date, this is the only physically plausible model that captures the abrupt change in the slope at n_{L1}.

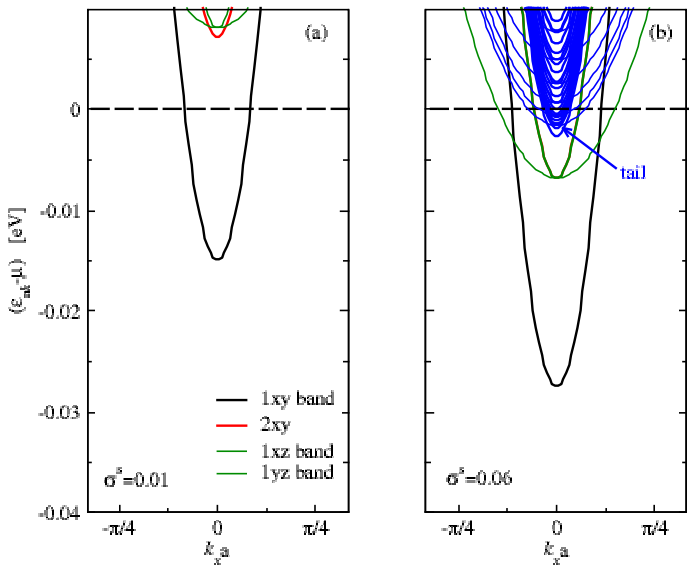

Figure 5.3: Band structure for a strained interface at $\sigma^s = 0.01$ (a) and 0.06 e/a^2 (b). Results are for $\eta_0 = 0.02$, $f_{11} = 2$ V, at T=1 K, $g_{11} = 1.33 \times 10^{10}$ JmC^{-2}, and for 100 STO layers.

Figure 5.5 shows the layer-dependent polarization $[P(z)]$ and charge density $[n(z)]$. The main point of this figure is that for $\sigma^s < n_{L1}$, there is a thin layer of negative polarization extending over $3a \leq z \leq 6a$ [Fig. 5.5.(a)], where the strain gradient is largest [see Fig. 5.1]. In this thin layer, the polarization points towards the interface, and opposite to the electric field. This increases the confining potential, and pushes the electrons to be confined in the first five layers, as shown in Fig. 5.5.(b). At $\sigma^s > n_{L1}$, the polarization switches its direction abruptly (it becomes positive), and it points away from the interface, as shown in Fig. 5.5.(a). This drives the electrons away from the interface to occupy other bands and spread between more layers [see Fig. 5.5.(b)].

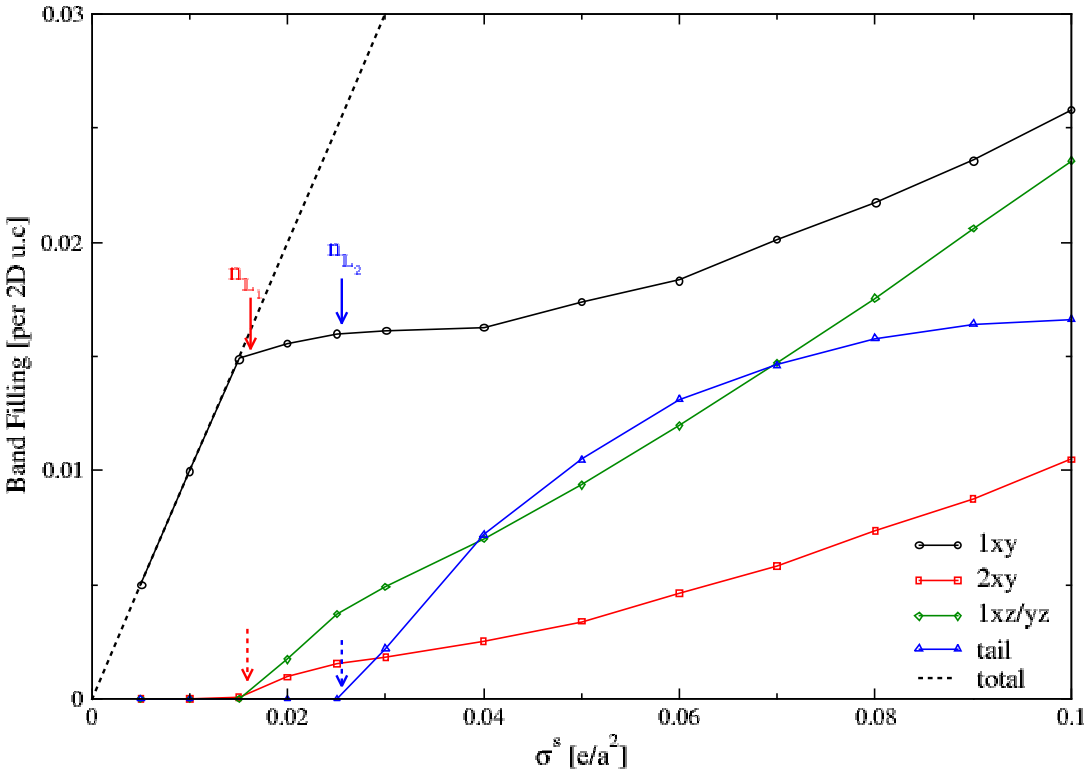

Figure 5.4: Occupation of the four lowest energy bands and tails as function of doping. Results are for $\eta_0 = 0.02$, $f_{11} = 2$ V, at T=1 K, $g_{11} = 1.33 \times 10^{10}$ JmC^{-2}, and for 100 layers.

To understand Fig. 5.5, we should refer to Eq. (5.10). At low doping, the electric field is weak and smaller than the flexelectric term, which results in a negative polarization, where the strain gradient is large. As the doping increases, the electric field becomes strong enough to overcome the flexelectric effect, and yields a positive polarization. We therefore conclude that the switching of the polarization direction is responsible for the Lifshitz transition in our model.

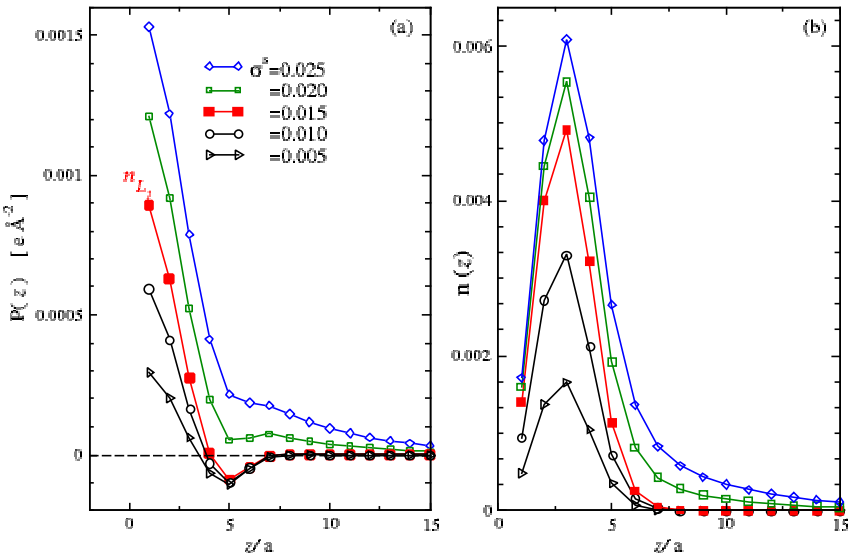

Figure 5.5: Layer-dependent polarization (a) and charge density (b) at different doping. Results are for $\eta_0 = 0.02$, $f_{11} = 2$ V, at T=1 K, $g_{11} = 1.33 \times 10^{10}$ JmC^{-2}, and for 100 STO layers.

5.2.2 Effect of Model Parameters on Band Filling

There are many factors in our model that affect the band filling, such as η and f_{11}. Experiments showed that the size of the interfacial strain η_0 ranges from 0.01-0.03 [92, 95]. In Fig. 5.6.(a), we plot the $1xy$-band filling (n_{1xy}) for different strains, and $f_{11} = 2$ V. As η_0 increases, n_{L1} increases. This can explain the variations in the Lifshitz charge density between different experiments [66, 75, 72]. Because there is uncertainty in the value of f_{11}, Fig. 5.6.(b) shows n_{1xy} for several f_{11}, and $\eta_0 = 0.02$. We can see that f_{11} has a similar effect on n_{L_1} as η_0. This can be understood from Eq. (5.10), where both f_{11} and η_0 determine the size of the flexoelectric term, and control its weight with respect to the electric field.

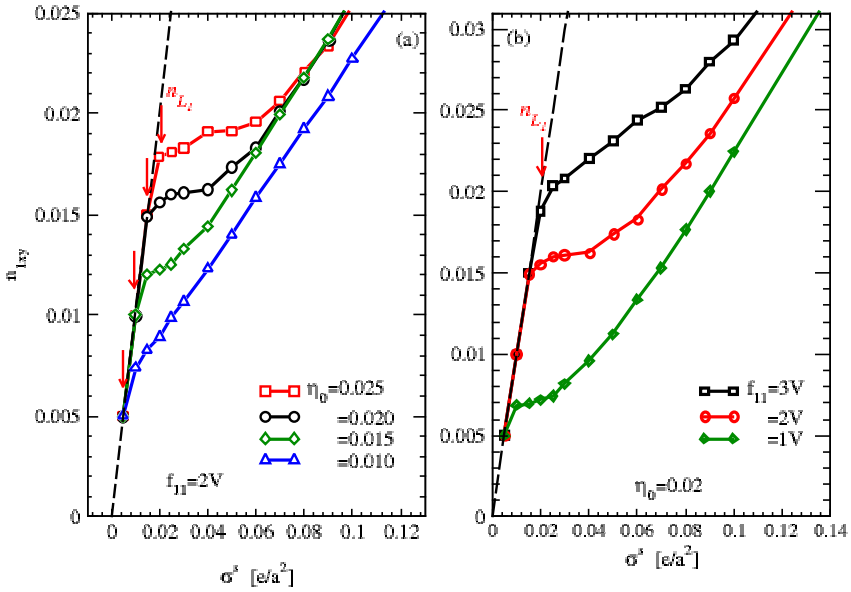

Figure 5.6: The lowest band filling as a function of doping for different strain and f_{11} values. Results of (a) are for $f_{11} = 2$ V, at T=1 K, and for 100 layers. Results of (b) are for $\eta_0 = 0.02$

On the other hand, we see that both γ and g_{11} do not affect the value of n_{L1}. Figure 5.7.(a) shows n_{1xy} at different γ values. We see that γ determines the behaviour of the $1xy$ filling at high doping. This is because, at high doping, the non-linear term in Eq. (5.10) reduces the dielectric screening, and is responsible for an upturn in n_{1xy}. In Fig. 5.7.(b), we show n_{1xy} as a function of g_{11}. It is clear that g_{11} changes the slope of the $1xy$ filling after the transition; small g_{11} gives a negative slope, similar to what Smink el al. reported [72].

For completeness, we repeat our calculations including the Hubbard term [Eq. (E.10)] for $\eta_0 = 0.02$, $f_{11} = 2$ V, and at T=1 K, Fig. 5.8.(a). As shown, the Lifshitz transition happens at a smaller n_{L_1} in this case. However, overall the change is quantitative

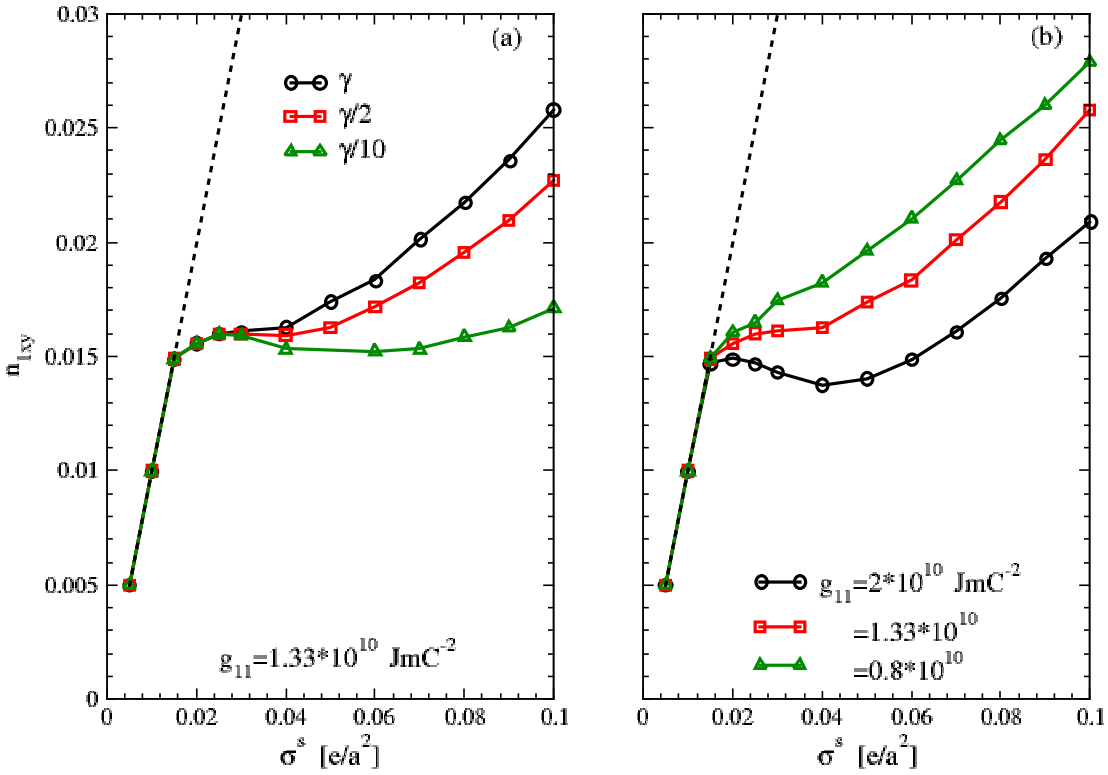

Figure 5.7: The lowest band filling as a function of doping for different γ, and g_{11} values. (a) shows the n_{1xy} at $g_{11} = 1.33 \times 10^{10}$ JmC^{-2} for γ, $\gamma/2$, and $\gamma/10$ where γ is given in Table 2.1. (b) shows n_{L_1} for several g_{11} values. Results of (a) and (b) are for $f_{11} = 2$ V, $\eta_0 = 0.02s$, at T=1 K, and for 100 layers.

rather than qualitative. This implies, similar to what we found in Chapter 4, that the short-range interactions do not have a big effect on the band structure.

We discussed before the strong dependence of the STO permittivity on temperature. In Fig. 5.8.(b), we study the effect of temperature on the Lifshitz transition. At T$\leq$ 20 K, n_{1xy} changes slightly, because $D_{i_z j_z}$ is nearly constant in this temperature

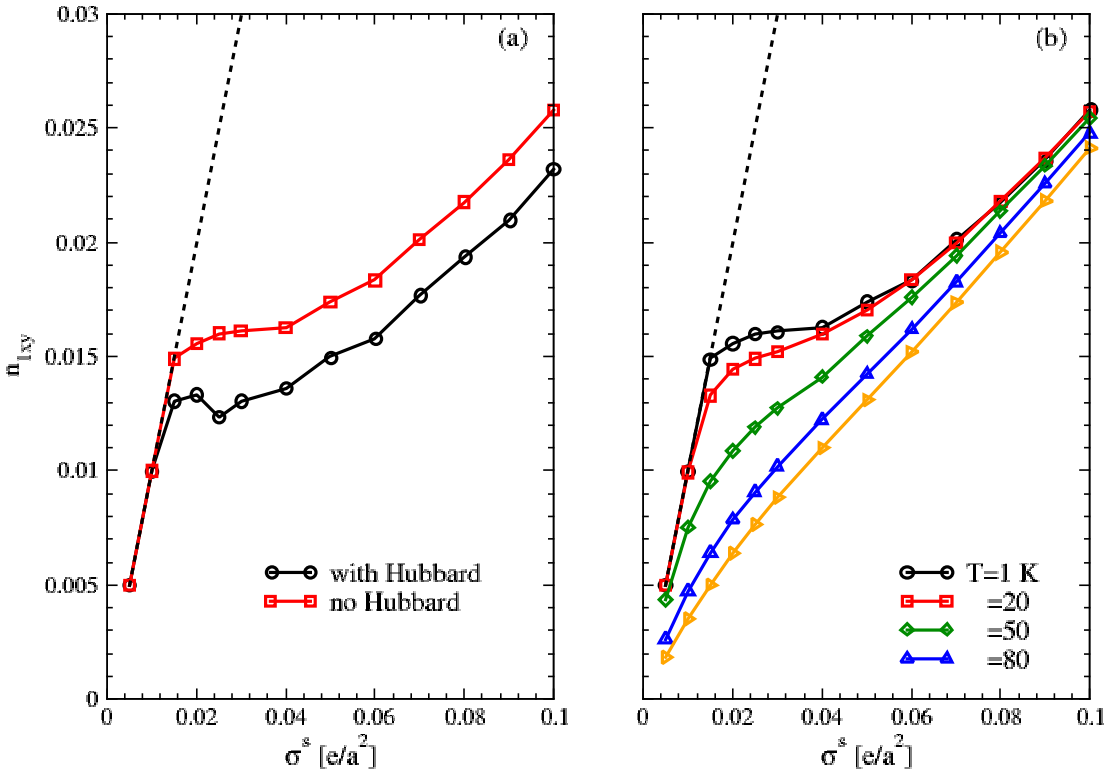

Figure 5.8: (a) shows n_{1xy} with and without Hubbard term, $U_0 = 4$, $U = 2.4$, and $J = 0.8$ eV. (b) shows n_{1xy} as a function of temperature. Results are for $\eta_0 = 0.02$, $f_{11} = 2$ V and for 100 STO layers.

range: it is a reminder that the saturation temperature in our model is 15 K. As the temperature increases, the transition gradually disappears. The reason for that is, the STO permittivity decreases, which increases the field strength and reduces the importance of the flexoelectric effect. We therefore do not see switching of the polarization direction.

5.3 Summary

It is well known that strain has a big effect on the electronic properties of thin films. In our model, we included strain effects in the the Landau-Devonshire equations in two steps. First, we included the strain coupling to the polarization, which gave the same band structure as in the ideal-interface case. We can understand this behaviour by looking to Eq. (5.6). g_{11} increases the permittivity in the interface region, which results in increased screening of the electric field. This effect spreads the electrons into the STO bulk, which does not agree with previous experimental studies.

The second step was to include the strain gradient in the Landau-Devonshire energy. The results show that at low doping there is only one occupied band with d_{xy} character. As the doping increases, there a Lifshitz transition to multiple occupied bands with different orbital character. We showed that the transition takes place when the polarization changes its direction, as shown in Fig. 5.5. The filling at which this happens depends on the flexoelectric term. If this term is bigger than the electric field, the polarization is opposite to the field, but if it is smaller than the electric field, the polarization points in the same direction as the field [Eq.(5.10)]. We have seen that both f_{11} and strains control the flexoelectric term and consequently the value of n_{L_1}. On the other hand, the value of g_{11} control the slope of n_{1xy} after transition.

To date, our interfacial-strain model is the only realistic model that predicted the two main features of the observed Lifshitz transition. This model can be tested by atomic-resolution probes that can resolve the interface polarization. Lee et al. [92] observed a head-to-head polarization in ungated LAO/STO samples. In their measurements, the reversed polarization on the STO side of the interface extends over 5 unit cells into the substrate, similar to what we propose. Therefore, it would

be interesting to use this technique to see whether the polarization can be switched by an external gate voltage, and to determine whether this correlates with a Lifshitz transition.

Chapter 6

Conclusion

STO-based interfaces have attracted attention due to their promising properties for applications. Many studies explored the relation between the interface properties and the dielectric permittivity of STO, and found that including the field-response of the dielectric function is essential to obtain a good description for the electron distribution, in particular at low doping. In this thesis, we made a careful exploration of the role of the dielectric function on the STO interface.

We started with an ideal-interface model, in which the interface dielectric is similar to the bulk. We calculated the band structure and charge distribution as functions of both doping and temperature. In Chapter 3, we showed that the dielectric screening shapes the band structure and electron distribution, and is responsible for the strong dependence of the interface on doping and temperature. Our calculations agree with experiments that reported an increasing width of the conducting region with decreasing temperature [3, 96].

However, there were differences with experiments. Our simple model does not agree with observations of a Lifshitz transition at low doping and low temperature. The observed Lifshitz transition has two important features: one is the transition

from one occupied band to multiple occupied bands at a critical charge density; the other is the change in the slope of the filling of the lowest band (n_{1xy}) with doping. To understand the transition, we modified our model at the interface permittivity. Motivated by experiments, we first assumed a dead layer at the interface. The weak screening due to low the permittivity at the interface confines the electrons to one band at low doping, and allows a crossover to multiple occupied bands at higher doping. Although the model predicted a Lifshitz transition at a critical charge density in the same range as the experimental one, it does not observe an abrupt slope change of n_{1xy} with doping. We found that the dielectric dead-layer model does not provide a complete description of the observed Lifshitz transition. This led us to change our treatment of the interface dielectric.

Strain is a common feature of interfaces, and its effect on the dielectric properties of STO is well studied. We included the interfacial-strain effects in our model by considering the coupling of the strain and strain gradients with polarization. The interfacial-strain model predicted the two main features of the observed Lifshitz transition, and it is the first realistic model to do that. In addition, this model gives a mechanism for the transition in which the strain creates a thin polarized layer whose direction reverses at a critical density.

Although, our interfacial-strain model captures the main features of the transition, differences with experiments remain on the high-doping side of the transition. Indeed, our simple model ignores some features of STO-based interfaces which may be helpful in reproducing the experimental results. For example, we ignored the effect of LAO polarization on the STO. In principle, one also can calculate the strain self-consistently using the extension of Landau-Devonshire model. However, the boundary

condition at LAO/STO interfaces is not obvious. In addition, we neglected cation intermixing, oxygen vacancies, and other defects at the interface, which influence the doping-dependent band structure. Ferromagnatism has been observed in some studies, if it is present, it must also affect the doping-dependent band structure. In future, it will be interesting to see whether including one or two of these features can improve the agreement with experiments.

Bibliography

[1] A. Ohtomo and H. Y. Hwang. A high-mobility electron gas at the $LaAlO_3/SrTiO_3$ heterointerface. *Nature*, 427(6973):423–426, January 2004.

[2] S. Thiel, G. Hammerl, A. Schmehl, C. W. Schneider, and J. Mannhart. Tunable Quasi-Two-Dimensional Electron Gases in Oxide Heterostructures. *Science*, 313(5795):1942–1945, September 2006.

[3] O Copie, V Garcia, C Bödefeld, C Carrétéro, M Bibes, G Herranz, E Jacquet, J L Maurice, B Vinter, S Fusil, K Bouzehouane, H Jaffrès, and A Barthélémy. Towards two-dimensional metallic behavior at $LaAlO_3/SrTiO_3$ interfaces. *Phys. Rev. Lett.*, 102(21):216804, May 2009.

[4] J. Mannhart, D.H.A. Blank, H.Y. Hwang, A.J. Millis, and J.-M. Triscone. Two-dimensional electron gases at oxide interfaces. *MRS Bulletin*, 33(11):10271034, 2008.

[5] Cheng Cen, Stefan Thiel, Jochen Mannhart, and Jeremy Levy. Oxide nanoelectronics on demand. *Science*, 323(5917):1026–1030, 2009.

[6] Fabio Miletto Granozio, Gertjan Koster, and Guus Rijnders. Functional oxide interfaces. *MRS Bulletin*, 38(12):10171023, 2013.

[7] Yun-Yi Pai, Anthony Tylan-Tyler, Patrick Irvin, and Jeremy Levy. Physics of $SrTiO_3$-based heterostructures and nanostructures: a review. *Reports on Progress in Physics*, 81(3):036503, 2018.

[8] Pavlo Zubko, Stefano Gariglio, Marc Gabay, Philippe Ghosez, and Jean-Marc Triscone. Interface physics in complex oxide heterostructures. *Annual Review of Condensed Matter Physics*, 2(1):141–165, 2011.

[9] Young Jun Chang, Luca Moreschini, Aaron Bostwick, Geoffrey A. Gaines, Yong Su Kim, Andrew L. Walter, Byron Freelon, Antonello Tebano, Karsten Horn, and Eli Rotenberg. Layer-by-layer evolution of a two-dimensional electron gas near an oxide interface. *Phys. Rev. Lett.*, 111:126401, Sep 2013.

[10] Pouya Moetakef, James R. Williams, Daniel G Ouellette, Adam P Kajdos, David Goldhaber-Gordon, S James Allen, and Susanne Stemmer. Carrier-Controlled Ferromagnetism in $SrTiO_3$. *Phys. Rev. X*, 2(2):021014, June 2012.

[11] Daniel G. Ouellette, Pouya Moetakef, Tyler A. Cain, Jack Y. Zhang, Susanne Stemmer, David Emin, and S. James Allen. High-density two-dimensional small polaron gas in a delta-doped mott insulator. *Scientific Reports*, 3, 2013.

[12] Paolo Perna, Davide Maccariello, Milan Radovic, U Scotti di Uccio, I Pallecchi, M Codda, Daniele Marre, Claudia Cantoni, J Gazquez, Maria Varela, S J. Pennycook, and F Granozio. Conducting interfaces between band insulating oxides: The $LaGaO_3/SrTiO_3$ heterostructure. *Applied Physics Letters*, 97:152111 – 152111, 11 2010.

[13] A Kalabukhov, Robert Gunnarsson, T Claeson, and Dag Winkler. Electrical transport properties of polar heterointerface between $KTaO_3$ and $SrTiO_3$. *arXiv:0704.1050 [cond-mat.mtrl-sci]*, 05 2007.

[14] N. Reyren, S. Thiel, A. D. Caviglia, L. Fitting Kourkoutis, G. Hammerl, C. Richter, C. W. Schneider, T. Kopp, A.-S. Rüetschi, D. Jaccard, M. Gabay, D. A. Muller, J.-M. Triscone, and J. Mannhart. Superconducting interfaces between insulating oxides. *Science*, 317(5842):1196–1199, August 2007.

[15] Feng Bi, Mengchen Huang, Sangwoo Ryu, Hyungwoo Lee, Chung-Wung Bark, Chang-Beom Eom, Patrick Irvin, and Jeremy Levy. Room-temperature electronically-controlled ferromagnetism at the $LaAlO_3/SrTiO_3$ interface. *Nature Communications*, 5:5019, 09 2014.

[16] Beena Kalisky, Julie A Bert, Christopher Bell, Yanwu Xie, Hiroki K. Sato, Masayuki Hosoda, Yasuyuki Hikita, Harold Y Hwang, and Kathryn A Moler. Scanning probe manipulation of magnetism at the $LaAlO_3/SrTiO_3$ heterointerface. *Nano Lett.*, 12:4055–4059, 2012.

[17] Beena Kalisky, Julie A. Bert, Brannon B. Klopfer, Christopher Bell, Hiroki K. Sato, Masayuki Hosoda, Yasuyuki Hikita, Harold Y. Hwang, and Kathryn A. Moler. Critical thickness for ferromagnetism in $LaAlO_3/SrTiO_3$ heterostructures. *Nature Communications*, 3:922, 2012.

[18] Amany Raslan. Two-diemnsional conductivity at the $LaAlTiO_3/SrTiO_3$ interfaces. Master's thesis, Trent University, Peterborough, ON, Canada, 2014.

[19] Naoyuki Nakagawa, Harold Y Hwang, and David A Muller. Why some interfaces cannot be sharp. *Nature Mater.*, 5(3):204–209, January 2006.

[20] ChengJian Li, YanPeng Hong, HongXia Xue, XinXin Wang, Yongchun Li, Kejian Liu, Weimin Jiang, Mingrui Liu, Lin He, RuiFen Dou, ChangMin Xiong, and JiaCai Nie. Formation of two-dimensional electron gas at amorphous/crystalline oxide interfaces. *Scientific Reports*, 8(1):404, 2018.

[21] G. Herranz, F. Snchez, N. Dix, M. Scigaj, and J. Fontcuberta. High mobility conduction at (110) and (111) $LaAlO_3/SrTiO_3$ interfaces. *Scientific Reports*, 2012.

[22] David A. Muller, Naoyuki Nakagawa, Akira Ohtomo, John L. Grazul, and Harold Y. Hwang. Atomic-scale imaging of nanoengineered oxygen vacancy profiles in $SrTiO_3$. *Nature*, 430:657, 08 2004.

[23] F. Gunkel, P. Brinks, S. Hoffmann-Eifert, R. Dittmann, M. Huijben, J. E. Kleibeuker, G. Koster, G. Rijnders, and R. Waser. Influence of charge compensation mechanisms on the sheet electron density at conducting $LaAlO_3/SrTiO_3$-interfaces. *Applied Physics Letters*, 100(5):052103, 2012.

[24] Alexey Kalabukhov, Robert Gunnarsson, Johan Börjesson, Eva Olsson, Tord Claeson, and Dag Winkler. Effect of oxygen vacancies in the $SrTiO_3$ substrate on the electrical properties of the $LaAlO_3/SrTiO_3$ interface. *Phys. Rev. B*, 75:121404, Mar 2007.

[25] N. C. Bristowe, P. B. Littlewood, and Emilio Artacho. Surface defects and conduction in polar oxide heterostructures. *Phys. Rev. B*, 83:205405, May 2011.

[26] S.A. Chambers, M.H. Engelhard, V. Shutthanandan, Z. Zhu, T.C. Droubay, L. Qiao, P.V. Sushko, T. Feng, H.D. Lee, T. Gustafsson, E. Garfunkel, A.B. Shah, J.-M. Zuo, and Q.M. Ramasse. Instability, intermixing and electronic structure at the epitaxial $LaAlO_3/SrTiO_3(001)$ heterojunction. *Surface Science Reports*, 65(10):317 – 352, 2010.

[27] H. Zaid, M. H. Berger, D. Jalabert, M. Walls, R. Akrobetu, I. Fongkaew, W. R. L. Lambrecht, N. J. Goble, X. P. A. Gao, P. Berger, and A. Sehirlioglu. Atomic-resolved depth profile of strain and cation intermixing around $LaAlO_3/SrTiO_3$ interfaces. *Scientific Reports*, 6:28118, 06 2016.

[28] K. van Benthem, C. Elssser, and R. H. French. Bulk electronic structure of $SrTiO_3$: Experiment and theory. *Journal of Applied Physics*, 90(12):6156–6164, 2001.

[29] Zoran Popović, Sashi Satpathy, and Richard Martin. Origin of the two-dimensional electron gas carrier density at the $LaAlO_3$ on $SrTiO_3$ interface. *Phys. Rev. Lett.*, 101(25):256801, December 2008.

[30] Won-Joon Son, Eunae Cho, Bora Lee, Jaichan Lee, and Seungwu Han. Density and spatial distribution of charge carriers in the intrinsic n-type $LaAlO_3$-$SrTiO_3$ interface . *Phys. Rev. B*, 79:245411, 2009.

[31] Guru Khalsa and A MacDonald. Theory of the $SrTiO_3$ surface state two-dimensional electron gas. *Phys. Rev. B*, 86(12):125121, September 2012.

[32] Se Young Park and Andrew J Millis. Charge density distribution and optical response of the $LaAlO_3/SrTiO_3$ interface. *Phys. Rev. B*, 87(20):205145, May 2013.

[33] Amany Raslan, Patrick Lafleur, and W. A. Atkinson. Temperature-dependent band structure of $SrTiO_3$ interfaces. *Phys. Rev. B*, 95:054106, Feb 2017.

[34] S Gariglio, A Fête, and J.-M. Triscone. Electron confinement at the $LaAlO_3$. *J. Phys. Cond. Mat.*, 27:283201, October 2015.

[35] Massimiliano Stengel. First-principles modeling of electrostatically doped perovskite systems. *Phys. Rev. Lett.*, 106(13):136803, March 2011.

[36] Zhicheng Zhong, Anna Tóth, and Karsten Held. Theory of spin-orbit coupling at $LaAlO_3/SrTiO_3$ interfaces and $SrTiO_3$ surfaces. *Phys. Rev. B*, 87(16):161102, April 2013.

[37] A F Santander-Syro, O Copie, T Kondo, F Fortuna, S Pailhès, R Weht, X G Qiu, F Bertran, A Nicolaou, A Taleb-Ibrahimi, P Le Fèvre, G Herranz, M Bibes, N Reyren, Y Apertet, P Lecoeur, A Barthélémy, and M J Rozenberg. Two-dimensional electron gas with universal subbands at the surface of $SrTiO_3$. *Nature*, 469(7329):189–193, January 2011.

[38] J Dec, W Kleemann, and M Itoh. Temperature dependence of the non-linearity coefficient of strontium titanate. *Ferroelectrics*, 316(1):59–64, July 2005.

[39] J Hemberger, P Lunkenheimer, R Viana, R Böhmer, and A Loidl. Electric-field-dependent dielectric constant and nonlinear susceptibility in $SrTiO_3$. *Phys. Rev. B*, 52(18):13159–13162, November 1995.

[40] Matthew Trainer. Ferroelectricity: Measurement of the dielectric susceptibility of strontium titanate at low temperatures. *American Journal of Physics*, 69(9):966–969, 2001.

[41] K. A. Müller and H. Burkard. Srtio$_3$: An intrinsic quantum paraelectric below 4 k. *Phys. Rev. B*, 19:3593–3602, Apr 1979.

[42] R A Cowley. Lattice Dynamics and Phase Transitions of Strontium Titanate. *Phys. Rev.*, pages A981–A997, May 1964.

[43] K V Reich, M Schecter, and B I Shklovskii. Accumulation, inversion, and depletion layers in $SrTiO_3$. *Phys. Rev. B*, 91:115303, 2015.

[44] Amany Raslan and W. A. Atkinson. Possible flexoelectric origin of the lifshitz transition in $LaAlO_3/SrTiO_3$ interfaces. *arXiv:1808.03797 [cond-mat.mes-hall]*, 2018.

[45] M E Lines and A M Glass. *Principles and applications of ferroelectrics and related materials*. Oxford University Press, Oxford, 2001.

[46] Neil W. Ashcroft and N. David Mermin. *Solid State Physics*. 1976.

[47] H Peelaers, K Krishnaswamy, L Gordon, D Steiauf, A Sarwe, A Janotti, and C G Van de Walle. Impact of electric-field dependent dielectric constants on two-dimensional electron gases in complex oxides. *Appl. Phys. Lett.*, 107(18):183505, November 2015.

[48] Netlib. Lapack driver routine, 2006.

[49] M Ben Shalom, M Sachs, D Rakhmilevitch, A Palevski, and Y. Dagan. Tuning spin-orbit coupling and superconductivity at the $SrTiO_3/LaAlO_3$ interface: A magnetotransport study. *Phys. Rev. Lett.*, 104(12):126802, March 2010.

[50] A D Caviglia, M Gabay, S Gariglio, N Reyren, C Cancellieri, and J.-M. Triscone. Tunable Rashba spin-orbit interaction at oxide interfaces. *Phys. Rev. Lett.*, 104(12):126803, March 2010.

[51] H. Walker and P. Ni. Anderson acceleration for fixed-point iterations. *SIAM Journal on Numerical Analysis*, 49(4):1715–1735, 2011.

[52] V Eyert. A comparative study on methods for convergence acceleration of iterative vector sequences. *J. Comp. Phys.*, 124(2):271–285, March 1996.

[53] C Cancellieri, A S Mishchenko, U Aschauer, A Filippetti, C Faber, O S Barišić, V A Rogalev, T Schmitt, N Nagaosa, and V N Strocov. Polaronic metal state at the $LaAlO_3/SrTiO_3$ interface. *Nature Comm.*, 7:10386, 2016.

[54] John R Tolsma, Alessandro Principi, Reza Asgari, Marco Polini, and Allan H MacDonald. Quasiparticle mass enhancement and Fermi surface shape modification in oxide two-dimensional electron gases. *Phys. Rev. B*, 93(4):045120, January 2016.

[55] L Mattheiss. Effect of the 110 °K phase transition on the $SrTiO_3$ conduction bands. *Phys. Rev. B*, 6(12):4740–4753, December 1972.

[56] Qian Tao, Bastien Loret, Bin Xu, Xiaojun Yang, Carl Willem Rischau, Xiao Lin, Benoît Fauqué, Matthieu J. Verstraete, and Kamran Behnia. Nonmonotonic anisotropy in charge conduction induced by antiferrodistortive transition in metallic $SrTiO_3$. *Phys. Rev. B*, 94:035111, Jul 2016.

[57] Pouya Moetakef, Tyler A Cain, Daniel G Ouellette, Jack Y Zhang, Dmitri O Klenov, Anderson Janotti, Chris G Van de Walle, Siddharth Rajan, S James Allen, and Susanne Stemmer. Electrostatic carrier doping of $GdTiO_3/SrTiO_3$ interfaces. *Appl. Phys. Lett.*, 99(23):232116, 2011.

[58] V K Guduru, A McCollam, A Jost, S Wenderich, H Hilgenkamp, J C Maan, A Brinkman, and U Zeitler. Thermally excited multiband conduction in $LaAlO_3/SrTiO_3$ heterostructures exhibiting magnetic scattering. *Phys. Rev. B*, 88(24):241301, December 2013.

[59] A Jost, V K Guduru, S Wiedmann, J C Maan, U Zeitler, S Wenderich, A Brinkman, and H Hilgenkamp. Transport and thermoelectric properties of the $LaAlO_3/SrTiO_3$ interface. *Phys. Rev. B*, 91:045304, 2015.

[60] A Dubroka, M Rössle, K W Kim, V K Malik, L Schultz, S Thiel, C W Schneider, J Mannhart, G Herranz, O Copie, M Bibes, A Barthélémy, and C Bernhard. Dynamical Response and Confinement of the Electrons at the $LaAlO_3/SrTiO_3$ Interface. *Phys. Rev. Lett.*, 104(15):156807, April 2010.

[61] C. Cancellieri, M. L. Reinle-Schmitt, M. Kobayashi, V. N. Strocov, P. R. Willmott, D. Fontaine, Ph. Ghosez, A. Filippetti, P. Delugas, and V. Fiorentini. Doping-dependent band structure of $LaAlO_3/SrTiO_3$ interfaces by soft x-ray

polarization-controlled resonant angle-resolved photoemission. *Phys. Rev. B*, 89:121412, 2014.

[62] S. M. Walker, F. Y. Bruno, Z. Wang, A. de la Torre, S. Riccó, A. Tamai, T. K. Kim, M. Hoesch, M. Shi, M. S. Bahramy, P. D. C. King, and F. Baumberger. Carrier-density control of the $SrTiO_3$ (001) surface 2D electron gas studied by arpes. *Advanced Materials*, 27:3894, 2015.

[63] G Berner, M Sing, H Fujiwara, A Yasui, Y Saitoh, A Yamasaki, Y Nishitani, A Sekiyama, N. Pavlenko, T. Kopp, C Richter, J Mannhart, S Suga, and R Claessen. Direct k-Space Mapping of the Electronic Structure in an Oxide-Oxide Interface. *Phys. Rev. Lett.*, 110(24):247601, June 2013.

[64] N Reyren, S Gariglio, A D Caviglia, D Jaccard, T Schneider, and J.-M. Triscone. Anisotropy of the superconducting transport properties of the $LaAlO_3/SrTiO_3$ interface. *Appl. Phys. Lett.*, 94:112506, 2009.

[65] M Basletić, J L Maurice, C Carrétéro, G Herranz, O Copie, M Bibes, E Jacquet, K Bouzehouane, S Fusil, and A Barthélémy. Mapping the spatial distribution of charge carriers in $LaAlO_3/SrTiO_3$ heterostructures. *Nature Mater.*, 7(8):621–625, June 2008.

[66] Arjun Joshua, S. Pecker, J. Ruhman, E. Altman, and S. Ilani. A universal critical density underlying the physics of electrons at the $LaAlO_3/SrTiO_3$ interface. *Nature Comm.*, 3:1129–, October 2012.

[67] S Lerer, M Ben Shalom, G Deutscher, and Y. Dagan. Low-temperature dependence of the thermomagnetic transport properties of the $SrTiO_3/LaAlO_3$ interface. *Phys. Rev. B*, 84(7):075423, August 2011.

[68] J S Kim, S S A Seo, M F Chisholm, R K Kremer, H U Habermeier, B Keimer, and H N Lee. Nonlinear Hall effect and multichannel conduction in $LaTiO_3/SrTiO_3$ superlattices. *Phys. Rev. B*, 82(20):201407, November 2010.

[69] A Spinelli, M A Torija, C Liu, C Jan, and C Leighton. Electronic transport in doped $SrTiO_3$: Conduction mechanisms and potential applications. *Phys. Rev. B*, 81(15):155110, April 2010.

[70] A Faridi, R Asgari, and A Langari. Electron mobility of a two-dimensional electron gas at the interface of $SrTiO_3$ and $LaAlO_3$. *Phys. Rev. B*, 93:235306, 2016.

[71] Wei Niu, Yu Zhang, Yulin Gan, Dennis V. Christensen, Merlin V. Soosten, Eduardo J. Garcia-Suarez, Anders Riisager, Xuefeng Wang, Yongbing Xu, Rong Zhang, Nini Pryds, and Yunzhong Chen. Giant tunability of the two-dimensional electron gas at the interface of γ-$Al_2O_3/SrTiO_3$. *Nano Letters*, 17(11):6878–6885, 2017.

[72] A. E. M. Smink, J. C. de Boer, M. P. Stehno, A. Brinkman, W. G. van der Wiel, and H. Hilgenkamp. Gate-tunable band structure of the $LaAlO_3$-$SrTiO_3$ interface. *Phys. Rev. Lett.*, 118:106401, Mar 2017.

[73] A. E. M. Smink, M. P. Stehno, J. C. de Boer, A. Brinkman, W. G. van der Wiel, and H. Hilgenkamp. Correlation between superconductivity, band filling, and

electron confinement at the $LaAlO_3/SrTiO_3$ interface. *Phys. Rev. B*, 97:245113, Jun 2018.

[74] S Gariglio, N Reyren, A D Caviglia, and J-M Triscone. Superconductivity at the $LaAlO_3/SrTiO_3$ interface. *Journal of Physics: Condensed Matter*, 21(16):164213, 2009.

[75] Haixing Liang, Long Cheng, Laiming Wei, Zhenlin Luo, Guolin Yu, Changgan Zeng, and Zhenyu Zhang. Nonmonotonically tunable rashba spin-orbit coupling by multiple-band filling control in $SrTiO_3$-based interfacial *d*-electron gases. *Phys. Rev. B*, 92:075309, Aug 2015.

[76] G. E. Volovik. Topological lifshitz transitions. *Low Temperature Physics*, 43(1):47–55, 2017.

[77] E. Maniv, M. Ben Shalom, A. Ron, M. Mograbi, A. Palevski, M. Goldstein, and Y. Dagan. Strong correlations elucidate the electronic structure and phase diagram of $LaAlO_3/SrTiO_3$ interface. *Nature Communications*, 6:8239, 2015.

[78] S. Nandy, N. Mohanta, S. Acharya, and A. Taraphder. Anomalous transport near the lifshitz transition at the $LaAlO_3/SrTiO_3$ interface. *Phys. Rev. B*, 94:155103, Oct 2016.

[79] W. A. Atkinson, P. Lafleur, and A. Raslan. Influence of the ferroelectric quantum critical point on $SrTiO_3$ interfaces. *Phys. Rev. B*, 95:054107, Feb 2017.

[80] Li-Wu Chang, Marin Alexe, James F. Scott, and J. Marty Gregg. Settling the dead layer debate in nanoscale capacitors. *Advanced Materials*, 21(48):4911–4914.

[81] M. S. Majdoub, R. Maranganti, and P. Sharma. Understanding the origins of the intrinsic dead layer effect in nanocapacitors. *Phys. Rev. B*, 79:115412, Mar 2009.

[82] A. A. Sirenko, C. Bernhard, A. Golnik, Anna M. Clark, Jianhua Hao, Weidong Si, and X. X. Xi. Soft-mode hardening in $SrTiO_3$ thin films. *Nature*, 404:373, 2000.

[83] Massimiliano Stengel and Nicola A. Spaldin. Origin of the dielectric dead layer in nanoscale capacitors. *Nature*, 443:679, 10 2006.

[84] A. M. Oleś. Antiferromagnetism and correlation of electrons in transition metals. *Phys. Rev. B*, 28:327–339, Jul 1983.

[85] Min Chu, Yongke Sun, Umamaheswari Aghoram, and Scott E. Thompson. Strain: A solution for higher carrier mobility in nanoscale mosfets. *Annual Review of Materials Research*, 39(1):203–229, 2009.

[86] A. Vailionis, H. Boschker, W. Siemons, E. P. Houwman, D. H. A. Blank, G. Rijnders, and G. Koster. Misfit strain accommodation in epitaxial ABO_3 perovskites: Lattice rotations and lattice modulations. *Phys. Rev. B*, 83:064101, Feb 2011.

[87] K. J. Choi, M. Biegalski, Y. L. Li, A. Sharan, J. Schubert, R. Uecker, P. Reiche, Y. B. Chen, X. Q. Pan, V. Gopalan, L.-Q. Chen, D. G. Schlom, and C. B. Eom. Enhancement of ferroelectricity in strained $BaTiO_3$ thin films. *Science*, 306(5698):1005–1009, 2004.

[88] Hiromoto Uwe and Tunetaro Sakudo. Stress-induced ferroelectricity and soft phonon modes in $SrTiO_3$. *Phys. Rev. B*, 13:271–286, Jan 1976.

[89] J. H. Haeni, P. Irvin, W. Chang, R. Uecker, P. Reiche, Y. L. Li, S. Choudhury, W. Tian, M. E. Hawley, B. Craigo, A. K. Tagantsev, X. Q. Pan, S. K. Streiffer, L. Q. Chen, S. W. Kirchoefer, J. Levy, and D. G. Schlom. Room-temperature ferroelectricity in strained $SrTiO_3$. *Nature*, 430:758, 2004.

[90] C. W. Bark, D. A. Felker, Y. Wang, Y. Zhang, H. W. Jang, C. M. Folkman, J. W. Park, S. H. Baek, H. Zhou, D. D. Fong, X. Q. Pan, E. Y. Tsymbal, M. S. Rzchowski, and C. B. Eom. Tailoring a two-dimensional electron gas at the $LaAlO_3/SrTiO_3$ (001) interface by epitaxial strain. *Proceedings of the National Academy of Sciences*, 108(12):4720–4724, 2011.

[91] Z. Huang, Z. Q. Liu, M. Yang, S. W. Zeng, A. Annadi, W. M. Lü, X. L. Tan, P. F. Chen, L. Sun, X. Renshaw Wang, Y. L. Zhao, C. J. Li, J. Zhou, K. Han, W. B. Wu, Y. P. Feng, J. M. D. Coey, T. Venkatesan, and Ariando. Biaxial strain-induced transport property changes in atomically tailored $SrTiO_3$-based systems. *Phys. Rev. B*, 90:125156, Sep 2014.

[92] P. W. Lee, V. N. Singh, G. Y. Guo, H.-J. Liu, J.-C. Lin, Y.-H. Chu, C. H. Chen, and M.-W. Chu. Hidden lattice instabilities as origin of the conductive interface between insulating $LaAlO_3$ and $SrTiO_3$. *Nature communications*, 7, 2016.

[93] Claudia Cantoni, Jaume Gazquez, Fabio Miletto Granozio, Mark P. Oxley, Maria Varela, Andrew R. Lupini, Stephen J. Pennycook, Carmela Aruta, Umberto Scotti di Uccio, Paolo Perna, and Davide Maccariello. Electron transfer and ionic displacements at the origin of the 2d electron gas at the LAO/STO interface: Direct measurements with atomic-column spatial resolution. *Advanced Materials*, 24(29):3952–3957, 2012.

[94] P. Zubko, G. Catalan, A. Buckley, P. R. L. Welche, and J. F. Scott. Strain-gradient-induced polarization in $SrTiO_3$ single crystals. *Phys. Rev. Lett.*, 99:167601, Oct 2007.

[95] P. R. Willmott, S. A. Pauli, R. Herger, C. M. Schlepütz, D. Martoccia, B. D. Patterson, B. Delley, R. Clarke, D. Kumah, C. Cionca, and Y. Yacoby. Structural basis for the conducting interface between $LaAlO_3$ and $SrTiO_3$. *Phys. Rev. Lett.*, 99:155502, Oct 2007.

[96] Hongxia Xue, Chengjian Li, Yanpeng Hong, Xinxin Wang, Yongchun Li, Kejian Liu, Weimin Jiang, Mingrui Liu, Lin He, Ruifen Dou, Changmin Xiong, and Jiacai Nie. Temperature dependence of the conductive layer thickness at the $LaAlO_3/SrTiO_3$ heterointerface. *Phys. Rev. B*, 96:235310, Dec 2017.

[97] J Dec, W Kleemann, and B Westwanski. Scaling behaviour of strontium titanate. *J. Phys. Cond. Mat.*, 11:L379–L384, 1999.

[98] Eleftherios N. Economou. *Green's Functions in Quantum Physics*. 2006.

Appendix A

Derivation of the Electron Density $n_{j_z\beta}$

The charge density for a site $j = (j_x, j_y, j_z)$ and orbital type β could be expressed as,

$$n_{j\beta} = \langle c^\dagger_{j\beta} c_{j\beta} \rangle, \tag{A.1}$$

where

$$c_{j\beta} = \frac{1}{\sqrt{N_{\mathbf{k}}}} \sum_{\mathbf{k}} e^{i\mathbf{k}\cdot\mathbf{r}_\beta} c_{j_z\mathbf{k}\beta}. \tag{A.2}$$

where j_z layer index, and $\mathbf{r}_\beta$ a 2D vector in the $x-y$ plane.

$$n_{j\beta} = \frac{1}{N_{\mathbf{k}}} \sum_{\mathbf{k}\mathbf{k}'} e^{-i\mathbf{k}'\cdot\mathbf{r}_\beta} e^{i\mathbf{k}\cdot\mathbf{r}_\beta} \langle c^\dagger_{j_z\mathbf{k}'\beta} c_{j_z\mathbf{k}\beta} \rangle, \tag{A.3}$$

where $\langle c^\dagger_{j_z\mathbf{k}'\beta} c_{j_z\mathbf{k}\beta} \rangle = \hat{n}_{j_z\mathbf{k}\beta}$ is the number of electrons in certain eigenstate. Since there is a translational invariance in the x and y direction, $n_{j\beta}$ only depends on layer index j_z, then we write

$$n_{j_z\beta} = \frac{1}{N_{\mathbf{k}}} \sum_{\mathbf{k}\mathbf{k}'} e^{-i\mathbf{k}'\cdot\mathbf{r}_\beta} e^{i\mathbf{k}\cdot\mathbf{r}_\beta} \langle c^\dagger_{j_z\mathbf{k}'\beta} c_{j_z\mathbf{k}\beta} \rangle. \tag{A.4}$$

We then transform to basis in which the Hamiltonian $\hat{H}^{\text{eff}}$ is diagonalize, since

$$H^{\text{eff}}(\mathbf{k})\psi(\mathbf{k}) = \psi(\mathbf{k})E(\mathbf{k}), \tag{A.5}$$

where ψ is the unitary matrix that diagonalizes H^{eff}, so

$$H^{\text{eff}}(\mathbf{k}) = \psi(\mathbf{k})E(\mathbf{k})\psi^{\dagger}(\mathbf{k}). \tag{A.6}$$

Since

$$\hat{H}^{\text{eff}}(\mathbf{k}) = \sum_{i_z\alpha, j_z\beta} c^{\dagger}_{j_z\beta\mathbf{k}'} H_{j_z\beta, i_z\alpha} c_{i_z\alpha\mathbf{k}}, \tag{A.7}$$

then define

$$\hat{H}^{\text{eff}}(\mathbf{k}) = \sum_{l} \sum_{i_z\alpha, j_z\beta} c^{\dagger}_{j_z\beta\mathbf{k}'} \psi_{j_z l} E_l \psi^{\dagger}_{l i_z} c_{i_z\alpha\mathbf{k}}, \tag{A.8}$$

where $l = \beta\mathbf{k}n$ with n is band index. We define

$$\gamma_l = \sum_{i_z} \psi^{\dagger}_{l i_z} c_{i_z\alpha\mathbf{k}}. \tag{A.9}$$

If ψ is real, then

$$\sum_{l} \psi_{l i_z} \gamma_l = c_{i_z\alpha\mathbf{k}}. \tag{A.10}$$

Therefore,

$$n_{j_z\beta} = \frac{1}{N_{\mathbf{k}}} \sum_{k} \sum_{MP} \psi^{*}_{IM} \langle \gamma^{\dagger}_M \gamma_P \rangle \psi_{IP}, \tag{A.11}$$

where $I = \mathbf{k}j_z$, then

$$n_{j_z\beta} = \frac{1}{N_{\mathbf{k}}} \sum_{k} \sum_{n} |\psi_{j_z\beta n}(\mathbf{k})|^2 \langle n_{n\mathbf{k}\beta} \rangle, \tag{A.12}$$

$$n_{j_z\beta} = \frac{1}{N_{\mathbf{k}}} \sum_{k} \sum_{n} |\psi_{j_z\beta n}(\mathbf{k})|^2 f(\epsilon_{n\mathbf{k}}), \tag{A.13}$$

where $n_{j_z\beta}$ is the charge density at layer j_z and orbital type β, n represents the band index, $\psi_{j_z\beta n}(\mathbf{k})$ is the eigenvector element and $f(\epsilon_{n\mathbf{k}})$ is the Fermi-Dirac distribution function.

Appendix B

Fitting the Dielectric Model to Experiments

This appendix describes work done by Patrick Lafleur to fit our Landau-Devonshire parameters to experiments. This was his contribution to Ref. [33]. It is included here for completeness.

In this appendix, we outline the process by which the model parameters were fitted to experimental measurements of the field- and temperature-dependent dielectric susceptibility

$$\chi_{ij}(T,E) = \frac{1}{\epsilon_0}\frac{\partial P_i}{\partial E_j}, \tag{B.1}$$

where i and j label unit cells. For a uniform electric field, the polarization and normal coordinate u are also uniform, and from Eq. (2.17),

$$\chi(T,E) = \frac{Q}{\epsilon_0 a^3}\frac{\partial u}{\partial E} \tag{B.2}$$

From Eq. (2.25), we then obtain

$$D_{\mathbf{q}=0}u + \gamma u^3 = QE, \tag{B.3}$$

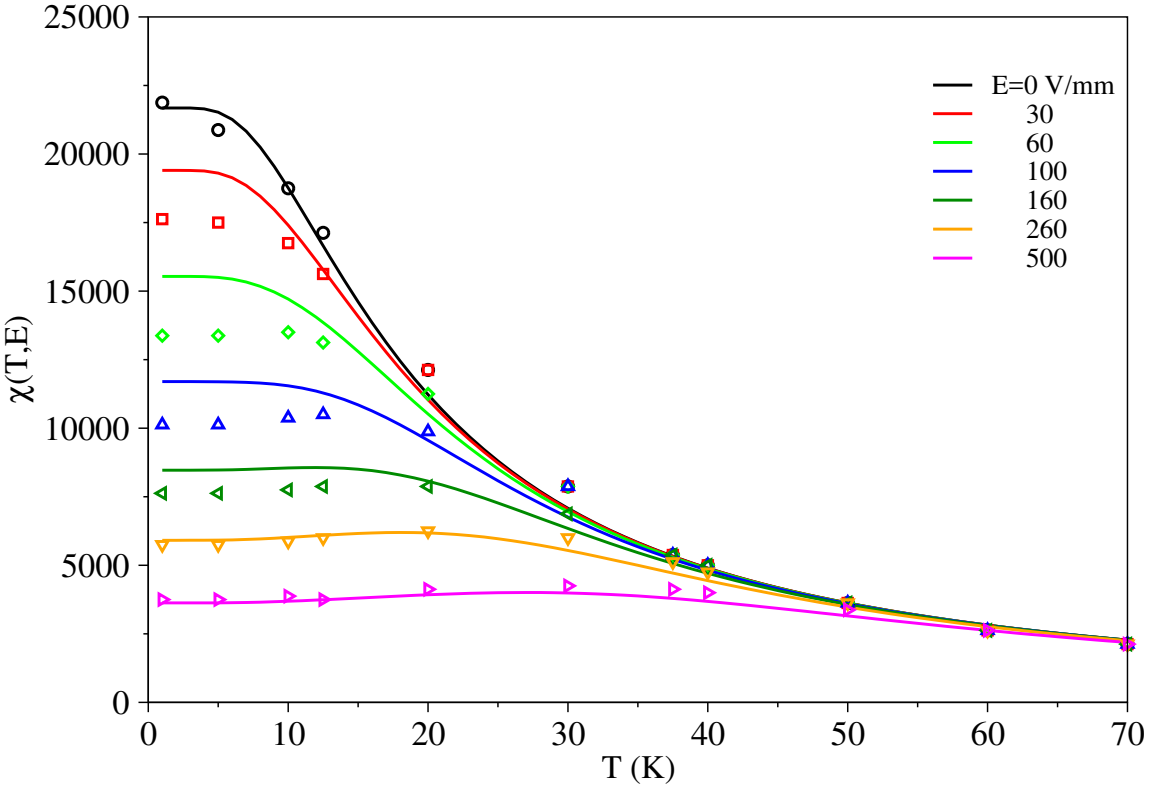

Figure B.1: Comparison of the uniform dielectric susceptibility $\chi(T, E)$ to the experimental results of Dec *et al.*[97] Symbols are experimental data, solid lines are theory. Results are shown as a function of temperature for different electric field strengths.

where $D_{\mathbf{q}=0} = \sum_j D_{ij}$. Differentiating Eq. (B.3) with respect to E, we obtain

$$\chi(T, E) = \frac{Q^2}{\epsilon_0 a^3} \frac{1}{D_{\mathbf{q}=0} + 3\gamma u^2}, \tag{B.4}$$

where u is obtained from Eq. (B.3).

Dec *et al.*[97] showed that the zero-field dielectric susceptibility can be fitted empirically by

$$\chi(T, 0) = \left(\frac{T_0}{T_Q}\right)^{\lambda} \tag{B.5}$$

where T_0 is a constant and $T_Q = T_s \coth(\frac{T_s}{T})$ is the quantum analogue of the temperature: when $T \gg T_s$, $T_Q \to T$ and when $T \ll T_s$, $T_Q \to T_s$. We note that λ was found to be 2 at low temperatures and 1 at high temperatures; to reduce the number of fitting parameters, we take $1 < \lambda < 2$ to be constant over the entire temperature range. This improves the quantitative fit to the data, but means that we do not reproduce the correct critical exponents at low T.

Equating Eq. (B.5) to Eq. (B.4) in the zero-field limit yields

$$D_{\mathbf{q}=0} = \frac{Q^2}{\epsilon_0 a^3} \left(\frac{T_Q}{T_0} \right)^{\lambda}. \tag{B.6}$$

Reinserting this into Eq. (B.4) gives us an equation for the nonlinear susceptibility at finite fields with the fitting parameters T_s, T_0, Q, λ, and γ. We fit this expression to the experimental data of Ref. [97], and the result is shown in Fig. B.1. The model reproduces the data at both low and room temperatures and a range of electric fields from 0 V/mm to 500 V/mm with a maximum relative error of 16%. The best fit parameters are given in Table 2.1.

To extend this model to finite $\mathbf{q}$, we take the empirical expression[31]

$$D_{\mathbf{q}} = M[\omega_0^2 - \omega_1^2 e^{\frac{-(\alpha_1 \mathbf{q})^2}{2}} - \omega_2^2(T) e^{\frac{-(\alpha_2 \mathbf{q})^2}{2}}], \tag{B.7}$$

where M is the reduced mass for the soft mode, ω_0, ω_1, and α_1 are used to reproduce the measured phonon dispersion [42] at 90 K, and $\omega_2(T)$ and α_2 are used to capture the low-temperature phonon dispersion. Equation (2.28) for the temperature-dependence of $\omega_2(T)$ can be obtained by setting $\mathbf{q} = 0$ in Eq. (B.7) and equating it to Eq. (B.6).

Appendix C

Atomic Spin-Orbit Coupling

In this appendix, we drive the Atomic spin-orbit coupling (ASOC) Hamiltonian. The spin-orbit coupling Hamiltonian is written as

$$\hat{H}_{\mathrm{SOC}} = \xi_{SOC}\, \hat{\vec{l}} \cdot \hat{\vec{s}} = \xi\, [\hat{l}_x \hat{s}_x + \hat{l}_y \hat{s}_y + \hat{l}_z \hat{s}_z], \tag{C.1}$$

with ξ_{SOC} is the atomic SOC strength, l is the orbital angluar momentum of the electron, and s is the spin.

We express the ASOC Hamiltonian terms of ladder operator as

$$\hat{H}_{\mathrm{SOC}} = \xi_{SOC}\, [\frac{1}{2}\hat{l}_- \hat{s}_+ + \frac{1}{2}\hat{l}_+ \hat{s}_- + \hat{l}_z \hat{s}_z]. \tag{C.2}$$

Because the orbital and spin angular momentum operators only act on the individual orbital and spin functions, the matrix elements of the product operators $\hat{l}_- \hat{s}_+, \hat{l}_+ \hat{s}_-$, and $\hat{l}_z \hat{s}_z$ can be formulated as a product of matrix elements, for example

$$\langle lms m_s | \hat{l}_- \hat{s}_+ | l' m' s' m'_s \rangle = \langle lm | \hat{l}_- | l' m' \rangle \langle s m_s | \hat{s}_+ | s' m'_s \rangle$$

These matrix elements can be evaluated using

$$\langle lm|\hat{l}_{\pm}|l'm'\rangle = \hbar[(l' \mp m')(l' \pm m' + 1)]^{1/2}\delta_{ll'}\delta_{m,m'\pm 1},$$

$$\langle lm|\hat{l}_{z}|l'm'\rangle = \hbar m'\delta_{ll'}\delta_{mm'},$$

and similary for $\hat{s}_{\pm}$, and $\hat{s}_z$.

In our case we construct the ASOC Hamiltonian for the 3d Ti t_{2g} orbitals, d_{xy}, d_{xz}, and d_{yz} as

$$\hat{H}_{SOC} = \frac{\xi_{SOC}}{2}\hbar^2 \begin{bmatrix} 0 & 0 & 0 & 0 & -i & 1 \\ 0 & 0 & -i & i & 0 & 0 \\ 0 & i & 0 & -1 & 0 & 0 \\ 0 & -i & -1 & 0 & 0 & 0 \\ i & 0 & 0 & 0 & 0 & i \\ 1 & 0 & 0 & 0 & -i & 0 \end{bmatrix} \begin{Bmatrix} xy\uparrow \\ xz\uparrow \\ yz\uparrow \\ xy\downarrow \\ xz\downarrow \\ yz\downarrow \end{Bmatrix}. \tag{C.3}$$

Appendix D

Derivation of the Electron Lifetime τ_n

Here, we include interface disorder in our model and calculate the resultant scattering rate within the Born approximation. In this case the Hamiltonian is

$$\hat{H}_{\text{tot}} = \hat{H}^{\text{eff}} + \hat{H}^{\text{imp}}, \tag{D.1}$$

where $\hat{H}^{\text{eff}}$ is given in Eq. (2.1), $\hat{H}^{\text{imp}}$ is the perturbation due to impurities [98, ch. 6]

$$\hat{H}^{\text{imp}} = \sum_{i\alpha\sigma} \epsilon_i c^{\dagger}_{i\alpha\sigma} c_{i\alpha\sigma}, \tag{D.2}$$

where $i = (i_x, i_y, i_z)$ is lattice site, and $\epsilon_i \in [\frac{-W_i}{2}, \frac{W_i}{2}]$ is the impurity potential with W_i the distribution width of the impurity potential at that site.

Economou [98, ch. 6] solves the total Hamiltonian by finding the corresponding Green function G,

$$[i\omega - \mathbf{H}^{\text{eff}} - \mathbf{H}^{\text{imp}}]\mathbf{G} = \mathbf{I} \tag{D.3}$$

$$(\mathbf{G}^0)^{-1}[1 - \mathbf{G}^0\mathbf{H}^{\text{imp}}]\mathbf{G} = \mathbf{I} \tag{D.4}$$

where $\mathbf{G}^0$ is is the Green function corresponding to $\hat{H}^{\text{eff}}$. To second order in the impurity potential, we solve Eq. (D.4)

$$G_{ij\alpha}(\omega) = G^0_{ij\alpha} + \sum_l G^0_{il\alpha}\epsilon_l G^0_{lj\alpha} + \sum_{lm} G^0_{il\alpha}\epsilon_l G^0_{lm\alpha}\epsilon_m G^0_{mj\alpha}. \tag{D.5}$$

Taking the average over the impurity potential, we get

$$\bar{\epsilon}_l = \frac{1}{W}\int_{\frac{-W_l}{2}}^{\frac{W_l}{2}} d\epsilon_l \epsilon_l = 0,$$

$$\overline{\epsilon_l \epsilon_m} = \delta_{lm} \times \frac{1}{W}\int_{\frac{-W_l}{2}}^{\frac{W_l}{2}} d\epsilon_l \epsilon_l^2 = \frac{W_l^2}{12},$$

and

$$\overline{G}_{ij\alpha}(\omega) = G^0_{ij\alpha} + \sum_l G^0_{il\alpha}\frac{W_l^2}{12}G^0_{ll\alpha}G^0_{lj\alpha}. \tag{D.6}$$

We define self-energy Σ_i as

$$\Sigma_{i\alpha} = \frac{W_i^2}{12}G^0_{ii\alpha}. \tag{D.7}$$

We assume that the impurity strength W_i depends on the layer i_z but is independent of position in the layer. Then

$$\Sigma_{i\alpha} = \frac{W_{i_z}^2}{12}G^0_{ii\alpha}, \tag{D.8}$$

with

$$G^0_{ii\alpha} = \frac{1}{N_{\mathbf{k}}}\sum_{\mathbf{k}}\sum_n |\psi_{i_z\alpha n}(\mathbf{k})|^2 \frac{1}{\omega - i\eta - \epsilon'_n(\mathbf{k})},$$

where η is a positive infinitesimal number.

We approximate the dispersions, Eqs. (2.8), near the Γ point by their quadratic forms

$$\epsilon'_n(\mathbf{k}) = \frac{\hbar^2}{2}(\frac{k_x^2}{m_x^n} + \frac{k_y^2}{m_y^n}) + \epsilon_{n0},$$

where ϵ_{n0} is the band bottom energy, and m_x^n and m_y^n are the effective masses in the x- and y-direction, respectively. The effective mass is

$$\frac{1}{m_{x,y}} = \frac{1}{\hbar^2}\frac{d^2\epsilon'_n(\mathbf{k})}{d\mathbf{k}^2},$$

then by using Eqs. (2.8), the effective masses in the x and y directions for the xy bands are

$$m_x^{xy} = m_y^{xy} = \frac{\hbar^2}{2at^{\parallel}},$$

for the xz bands are

$$m_x^{xz} = \frac{\hbar^2}{2at}, \quad m_y^{xz} = \frac{\hbar^2}{2at^{\perp}},$$

and for the yz bands are

$$m_x^{yz} = \frac{\hbar^2}{2at^{\perp}}, \quad m_y^{yz} = \frac{\hbar^2}{2at^{\parallel}}.$$

To calculate the sum over $\mathbf{k}$, we convert it to integration as

$$\sum_{\mathbf{k}} \to \int d^2\mathbf{k} \to \frac{\sqrt{m_x^n m_y^n}}{\hbar^2}\int d\xi_x\xi_y \to \frac{\sqrt{m_x^n m_y^n}}{\hbar^2}\int_0^{2\pi} d\theta \int \xi d\xi,$$

where $\xi_x = \frac{\hbar\mathbf{k}_x}{\sqrt{m_x}}$, and $\xi_y = \frac{\hbar\mathbf{k}_y}{\sqrt{m_y}}$. Then

$$G^0_{i_z i_z} = \frac{1}{N_{\mathbf{k}}}\sum_n |\psi_{i_z\alpha n}(\mathbf{k})|^2 \frac{\sqrt{m_x^n m_y^n}}{\hbar^2}\int_0^{2\pi} d\theta \int \xi d\xi \frac{1}{\omega - i\eta - \xi^2 - \epsilon_{n0}},$$

where we have used the fact that $\psi_{i_z\alpha n}$ does not depend on $\mathbf{k}$.

The scattering rate for electrons in band n is given in terms of the self-energy as

$$\gamma^n = -Im\Sigma_n.$$

Therefore,

$$\gamma^n = \frac{\sqrt{m_x^n m_y^n}}{\hbar^2} \sum_{i_z} |\psi_{i_z\alpha n}|^2 \frac{W_{i_z}^2 a^2}{24}. \tag{D.9}$$

Here, we assume that $W_{i_z} = W$ in the first Λ layers, and is zero further from the interface. Then, the electron lifetime τ_n in band n is

$$\frac{\hbar}{\tau_n} = \frac{\sqrt{m_{x,n} m_{y,n}} W^2 a^2}{24\hbar^2} \sum_{i_z=1}^{\Lambda} |\Psi_{i_z\alpha,n}|^2. \tag{D.10}$$

Appendix E

Derivation of Hubbard Model for Short-Range Interactions

In this appendix, we introduce our derivation for the short-range electron-electron interactions. This derivation comes from Ref. [84], here we provide details that are not given in the original article [84].

The Hubbard term is given

$$\hat{H}_{hub} = \frac{1}{2}\sum_{\sigma}\int d^3\mathbf{r}d^3\mathbf{r}'\Psi^{\dagger}_{\sigma}(\mathbf{r})\Psi^{\dagger}_{\sigma'}(\mathbf{r}')V(\mathbf{r}-\mathbf{r}')\Psi_{\bar{\sigma}}(\mathbf{r}')\Psi_{\sigma}(\mathbf{r}) \tag{E.1}$$

where

$$\Psi_{\sigma}(\mathbf{r}) = \sum_{i}\sum_{\alpha}\psi_{i\alpha}(\mathbf{r})c_{i\alpha\sigma}, \tag{E.2}$$

and

$$\Psi^{\dagger}_{\sigma}(\mathbf{r}) = \sum_{i'}\sum_{\alpha'}\psi^{*}_{i'\alpha'}(\mathbf{r})c^{\dagger}_{i'\alpha'\sigma}. \tag{E.3}$$

Then,

$$\hat{H}_{hub} = \frac{1}{2}\sum_{\sigma}\sum_{ij,i'j'}\sum_{\alpha\beta,\alpha'\beta'}\int d^3\mathbf{r}d^3\mathbf{r}'\psi^*_{i'\alpha'}(\mathbf{r})\psi^*_{j'\beta'}(\mathbf{r}')V(\mathbf{r}-\mathbf{r}')\psi_{j\beta}(\mathbf{r}')\psi_{i\alpha}(\mathbf{r})c^\dagger_{i'\alpha'\sigma}c^\dagger_{j'\beta'\bar{\sigma}}c_{j\beta\bar{\sigma}}c_{i\alpha\sigma}, \tag{E.4}$$

with σ is the electron spin, i, j labels the unit cell, and α, β is the orbital type. Assume that the interactions taking place at the same site are more important than different sites, i.e $i = i' = j = j'$, therefore,

$$\hat{H}_{hub} = \frac{1}{2}\sum_{\sigma}\sum_{i}\sum_{\alpha\beta,\alpha'\beta'}\int d^3\mathbf{r}d^3\mathbf{r}'\psi^*_{i\alpha'}(\mathbf{r})\psi^*_{i\beta'}(\mathbf{r}')V(\mathbf{r}-\mathbf{r}')\psi_{i\beta}(\mathbf{r}')\psi_{i\alpha}(\mathbf{r})c^\dagger_{i\alpha'\sigma}c^\dagger_{i\beta'\bar{\sigma}}c_{i\beta\bar{\sigma}}c_{i\alpha\sigma}. \tag{E.5}$$

We now define interaction parameters, U_0, U, and J as

$$U_{0\alpha} = \int d^3\mathbf{r}d^3\mathbf{r}'|\psi_{i\alpha}(\mathbf{r})|^2V(\mathbf{r}-\mathbf{r}')|\psi_{i\alpha}(\mathbf{r}')|^2, \tag{E.6}$$

$$U_{\alpha\beta} = \int d^3\mathbf{r}d^3\mathbf{r}'|\psi_{i\alpha}(\mathbf{r})|^2(\mathbf{r}')V(\mathbf{r}-\mathbf{r}')|\psi_{i\beta}(\mathbf{r}')|^2, \tag{E.7}$$

$$J_{\alpha\beta} = \int d^3\mathbf{r}d^3\mathbf{r}'\psi^*_{i\beta}(\mathbf{r})\psi^*_{i\alpha}(\mathbf{r}')V(\mathbf{r}-\mathbf{r}')\psi_{i\beta}(\mathbf{r}')\psi_{i\alpha}(\mathbf{r}). \tag{E.8}$$

Therefore, the Hubbard Hamiltonian in terms of thes interaction parameters is

$$\begin{aligned}\hat{H}_{hub} &= \sum_i \sum_\alpha U_{0\alpha} \hat{n}_{i\alpha\uparrow} \hat{n}_{i\alpha\downarrow} + \frac{1}{2} \sum_\sigma \sum_i \sum_{\alpha\beta} U_{\alpha\beta} \hat{n}_{i\alpha\sigma} \hat{n}_{i\beta\bar{\sigma}} + \sum_\sigma \sum_i \sum_{\alpha<\beta} U_{\alpha\beta} \hat{n}_{i\alpha\sigma} \hat{n}_{i\beta\sigma} \\ &- \sum_\sigma \sum_i \sum_{\alpha<\beta} J_{\alpha\beta} \hat{n}_{i\alpha\sigma} \hat{n}_{i\beta\sigma} - \sum_\sigma \sum_i \sum_{\alpha<\beta} J_{\alpha\beta} c^\dagger_{i\beta\sigma} c_{i\beta\bar{\sigma}} c^\dagger_{i\alpha\bar{\sigma}} c_{i\alpha\sigma} \\ &+ \frac{1}{2} \sum_\sigma \sum_i \sum_{\alpha\beta} J_{\alpha\beta} c^\dagger_{i\alpha\sigma} c^\dagger_{i\alpha\bar{\sigma}} c_{i\beta\bar{\sigma}} c_{i\beta\sigma}, \end{aligned} \tag{E.9}$$

where $\hat{n}_{i\alpha\sigma} = c^\dagger_{i\alpha\sigma} c_{i\alpha\sigma}$. $\alpha < \beta$ is here to avoid double counting over the orbital type.

In the mean field theory, the charge density operator ($c^\dagger_{i\alpha\sigma} c_{i\alpha\sigma}$) deviates from its average value, $\langle c^\dagger_{i\alpha\sigma} c_{i\alpha\sigma} \rangle$ as

$$\delta n_{i\alpha\sigma} = c^\dagger_{i\alpha\sigma} c_{i\alpha\sigma} - \langle c^\dagger_{i\alpha\sigma} c_{i\alpha\sigma} \rangle,$$

therefore, the Hubbard Hamiltonian in mean-field approximation is

$$\begin{aligned}\hat{H}^{MF}_{hub} &= \sum_i \sum_\alpha U_{0\alpha} \bar{n}_{i\alpha\downarrow} \hat{n}_{i\alpha\uparrow} + \sum_i \sum_\alpha U_{0\alpha} \bar{n}_{i\alpha\uparrow} \hat{n}_{i\alpha\downarrow} - \sum_i \sum_\alpha U_{0\alpha} \bar{n}_{i\alpha\uparrow} \bar{n}_{i\alpha\downarrow} \\ &+ \sum_\sigma \sum_i \sum_{\alpha<\beta} U_{\alpha\beta} \bar{n}_{i\beta\bar{\sigma}} \hat{n}_{i\alpha\sigma} + \sum_\sigma \sum_i \sum_{\alpha<\beta} U_{\alpha\beta} \bar{n}_{i\alpha\sigma} \hat{n}_{i\beta\bar{\sigma}} - \sum_\sigma \sum_i \sum_{\alpha<\beta} U_{\alpha\beta} \bar{n}_{i\alpha\sigma} \bar{n}_{i\beta\bar{\sigma}} \\ &+ \sum_\sigma \sum_i \sum_{\alpha<\beta} U_{\alpha\beta} \bar{n}_{i\beta\sigma} \hat{n}_{i\alpha\sigma} + \sum_\sigma \sum_i \sum_{\alpha<\beta} U_{\alpha\beta} \bar{n}_{i\alpha\sigma} \hat{n}_{i\beta\sigma} - \sum_\sigma \sum_i \sum_{\alpha<\beta} U_{\alpha\beta} \bar{n}_{i\alpha\sigma} \bar{n}_{i\beta\sigma} \\ &- \sum_\sigma \sum_i \sum_{\alpha<\beta} J_{\alpha\beta} \bar{n}_{i\beta\sigma} \hat{n}_{i\alpha\sigma} - \sum_\sigma \sum_i \sum_{\alpha<\beta} J_{\alpha\beta} \bar{n}_{i\alpha\sigma} \hat{n}_{i\beta\sigma} + \sum_\sigma \sum_i \sum_{\alpha<\beta} J_{\alpha\beta} \bar{n}_{i\alpha\sigma} \bar{n}_{i\beta\sigma}, \end{aligned}$$

where $\bar{n}_{i\beta\sigma} = \langle c^\dagger_{i\alpha\sigma} c_{i\alpha}\sigma \rangle$ is the occupation of a single orbital (α, σ) in layer i.

By assuming that $\bar{n}_{i\alpha\downarrow} = \bar{n}_{i\alpha\uparrow}$, and $U_{\alpha\beta} = U$, then the final Hubbard Hamiltonian is

$$\hat{H}_{hub}^{MF} = \sum_{i\alpha\sigma} U_0 \bar{n}_{i\alpha\sigma} \hat{n}_{i\alpha\bar{\sigma}} + \sum_{i\sigma} \sum_{\beta\neq\alpha} (2U - J) \bar{n}_{i\beta\sigma} \hat{n}_{i\alpha\bar{\sigma}}, \tag{E.10}$$

Appendix F

Numerical Solution of the Interfacial-Strain Model

We find that, for the interfacial-strain model, self-consistent calculations are not stable, and it is hard to make the code converge. This is that because the flexoelectric term leads to a rapid switching of the polarization direction from one iteration to the next. To overcome this problem, we find that the calculations are easily controlled if we work in a basis in which the matrix D is diagonal. The Landau- Devonshire free energy is

$$\frac{U}{N_{2D}} = \frac{1}{2}\sum_{i_z j_z} u_{i_z}\tilde{D}_{i_z j_z}u_{j_z} - \sum_{i_z}\tilde{E}_{i_z}u_{i_z} + \frac{\gamma}{4}\sum_{i_z}u_{i_z}^4 \tag{F.1}$$

where

$$\tilde{D}_{i_z j_z} = D_{i_z j_z} - 2\tilde{g}_{11}\delta_{i_z j_z}\eta_{i_z},$$

and

$$\tilde{E}_{i_z} = QE_{i_z} + \tilde{f}_{11}\frac{\partial \eta_{i_z}}{\partial z_i}.$$

Letting λ and $\mathbf{S}$ be the eigenvalues and the matrix of eigenvectors of $\tilde{D}$, the energy

equation in mode index basis n is

$$U = \frac{1}{2}\sum_n \lambda_n a_n^2 - \sum_n \tilde{E}_n a_n + \frac{\gamma}{4}\sum_n a_n^4, \tag{F.2}$$

where $a_n = \sum_i u_i S_{in}$, and $\tilde{E}_n = \sum_i E_i S_{in}$. The first two terms in Eq. (F.2) are formally equivalent to Eq. (F.1), while the final term is an ansatz.

To stabilize the calculations, we rearrange Eq. (F.2) such that we group the depolarizing fields (given in Eq. (2.22)) with λ_n. This gives

$$(\lambda_l + \frac{Q^2}{\epsilon_\infty a^3})a_l - \tilde{E}_l^{\text{other}} + \gamma a_l^3 = 0. \tag{F.3}$$

Because $\lambda_l + \frac{Q^2}{\epsilon_\infty a^3} > 0$, This helps stabilize the iterative cycle. We solve Eq. (F.3) for a_l, and then find $u_i = \sum_n S_{in} a_n$.